Department of Physics and Astronomy
University of Heidelberg

Master thesis

in Physics

submitted by

Marvin Kriening

born in Jena

2022

The 3-D Potential Vorticity Development during the Tropical Transition of Hurricane Leslie (2018) and Paulette (2020) over the North Atlantic Ocean

This Master thesis has been carried out by Marvin Kriening

at the

Institute of Environmental Physics

under the supervision of

Prof. Dr. André Butz

and

Prof. Dr. Andreas Fink

Institute of Meteorology and Climate Research at Karlsruhe Institute of Technology

Heidelberg 2022

Abstract (German)

Extratropische oder subtropische Wirbelstürme, welche eine erhebliche Menge Energie aus baroklinen oder diabatischen Prozessen ziehen, stellen potentielle Vorläufer tropischer Zyklogenese dar. *Tropical Transition*-Prozesse (TT), welche die Entwicklung tropischer Zyklone basierend auf dem Vorhandensein außertropischer Störungen beschreiben, sind noch heute durch eine vergleichsweise schwache Vorhersagbarkeit sowie durch eine hohe Präsenz in der Nord-Atlantik-Region charakterisiert. Dies ist Folge der Variabilität der Umwelteigenschaften, welche durch die ihnen vorausgehenden atmosphärischen Wechselwirkungen gegeben sind. Ziel dieser Arbeit ist es, unter Betrachtung der Entwicklung Potentieller Vorticity (PV), die Voraussetzungen sowie Hauptursachen für TT-Szenarien besser zu verstehen. Durch die Nutzung von Ensemble Wettervorhersagen des europäischen Zentrums für mittelfristige Wettervorhersage werden die Entwicklungen von Hurrikan Leslie (2018) und Hurrikan Paulette (2020) näher untersucht. Beide Systeme wurden aufgrund ihrer außergewöhnlichen Trajektorien, des vergleichsweise unberechenbaren Verhaltens und deren Einbettung in stark barokline Randbedinungen ausgewählt. Diese Studie soll eine Fortsetzung der Arbeit von Maier-Gerber et al. [1] darstellen. Ziel ist es, Merkmale von PV-Strukturen abzuleiten, welche das Aufkommen von TT-Szenarien begünstigen oder dessen Entwicklung beschränken. Hierbei wird, durch Nutzung eines neuartigen Algorithmus zur Analyse von PV-Anomalien, insbesondere die 3-D Struktur der jeweiligen PV-Streamer untersucht. *Dynamic Time Warping* wird genutzt um ein erfolgreiches Tracken der jeweiligen Stürme zu gewährleisten. Cyclone-Phase-Space-Diagramme werden verwendet, um zwischen abgeschlossenen und nicht-realisierten TT-Ereignissen zu unterscheiden. Zusätzlich wird die Entwicklung des Kopplungsindex (CI), motiviert durch die Studie von McTaggart-Cowan et al., herangezogen, um Rückschluss auf die konvektive Stabilität der Atmosphäre in der Umgebung des beschriebenen Sturmzentrums schließen zu können. Die 3-D-Untersuchung der PV-Entwicklung im Zusammenhang mit den beiden TT-Szenarien veranschaulicht die Vorteile, welche durch die Aufteilung der Ensemblevorhersage in Gruppen gewonnen werden können. Des Weiteren wird hierbei die Gestalt der PV-Struktur selbst, als eine der ausschlaggebensten Kriterien für die Realisierung der TT, herausgearbeitet und hervorgehoben werden.

Abstract (English)

Extratropical or Subtropical cyclones, which extract a significant amount of required energy from baroclinic and diabatic processes, can serve as seeds for further tropical cyclogenesis. Pathways, characterized by the evolution of a tropical cyclone based on the development of a nontropical precursor feature are known as *Tropical Transitions* (TTs). These events, while especially prominent over the North Atlantic Ocean, are still associated with a comparatively low predictability. This is the result of the pronounced variety in environmental conditions given by the atmospheric interactions preceding them. Investigating and understanding the main drivers for TT, given the PV framework consideration, is what motivates this thesis. By using the operational European Centre for Medium-Range Weather Forecasts ensemble predictions, the development of Hurricane Leslie (2018) and Hurricane Paulette (2020) are considered. Both systems, characterized by extraordinary storm tracks, erratic behavior and the embedment in highly baroclinic environments, were assessed as legitimate choices for this study. Here we follow the preceding and in-depth work of Maier-Gerber et al. [1]. The general goal is to infer the necessary features of PV structures leading to, or vitiating a possible TT scenario, while going a step further by also investigating the 3-D structure of the associated streamers by applying a novel algorithm for the objective identification of PV anomalies. The technique of dynamic time warping is applied to identify adequate ensemble tracks with respect to the analysis track. Cyclone-Phase-Space diagrams are used in order to differentiate between completed and uncompleted TT events. Additionally, the Coupling Index (CI) development, motivated by the study of McTaggart-Cowan et al., is analyzed to shed light on to the importance of convective stability in the vicinity of the respective storm system. The 3-D investigation of the PV evolution associated with the two TT scenarios demonstrates the purpose of further separating the ensemble weather forecast in several groups, while also highlighting the favorable shape of the associated PV streamer as one of the main necessary preconditions for TT itself.

Contents

1 Introduction

Tropical Cyclones still demonstrate one of the most threatening natural hazards for human life. While especially prominent over the Western Pacific, Indian and Atlantic Ocean, tropical cyclones are mostly accompanied by storm surge, flooding, lightning or even tornadoes. Because the heat, released by the condensation of water vapor, serves in order to drive the vortex, tropical cyclones can survive longer over the North Atlantic Basin due to the existence of the Gulf Stream. Associated with this, these storm systems can make landfall over the North American Continent, while leading to significant damages (As demonstrated by the latest Hurricane Ian (2022)), or recurve and follow their trajectory over cooler waters. Despite the latest technologies for forecasting tropical storms, the predictability of such systems still remains not fully understood. This becomes especially apparent when analyzing more chaotic tropical cyclogenesis pathways, such as the *Tropical Transition Process* (TT), on which we will mainly focus in this study.
A series of events leading to the development and transformation of a baroclinic, vertically sheared, extratropical cyclone into a warm-core, vertically stacked tropical cyclone is universally defined as *Tropical Transition* [2]. In order to facilitate the evolution of a tropical cyclone at the later stages of a TT, structural characteristics of the upper troposphere are of major importance. In particular, a climatological perspective, investigated by McTaggart-Cowan et al. [3], revealed that 16% of all tropical cyclones between 1948 and 2010 developed from TT and associated baroclinic precursors at upper-levels in the troposphere. Furthermore the understanding of the TT development pathway is of exceptionally high importance concerning the North Atlantic region, where roughly 40% of all tropical cyclogenesis events result from TT. The formation of an upper-level trough, characterizing an intrusion of stratospheric high *Potential Vorticity* (PV) air, which enters the upper tropospheric environment, is a necessary pre-condition to realize a "successful" TT-process. Associated with this, anticyclonic wave breaking events of upper-level trough structures play a major role in providing sufficient environmental conditions. Resulting from baroclinic disturbances, high PV troughs are able to enter tropical regions [4], leading to the formation of extratropical or subtropical cyclones. Therefore, they serve as precursors for potential TT events ([5], [6] and [7]). After formation of the antecedent nontropical storm system, a preexisting lower-level baroclinic zone interacting with the upper-level PV anomaly favors the organization of convection in the vicinity of the trough [2]. Hence, this process represents the possibility to reduce existing PV gradients above the storm center and further reduces vertical wind shear ([5] and [8]), which is a necessary condition in order to realize tropical cyclogenesis. Bentley et al. [7] show, that TT events occurring over the North Atlantic basin are generally observed at higher latitudes in comparison to other oceanic regions, which is due to the extratropical origin of the PV trough associated with the storm development. Furthermore a climatological study by McTaggart-Cowan et al. [9], investigating tropical cyclogenesis events from 1989 to 2013, reveals that the *Coupling Index* (CI), a measure of tropospheric depth and bulk convective stability, should rather be used, instead of sea surface temperature, in order to improve the predictability of TT scenarios. Based on the strength of the baroclinicity in the lower troposphere ([9] and [10]), TT is separated in *Weak TT* and *Strong TT* respectively. As a result, 27% of all strong TT formations were observed over waters cooler than 26.5° C, the common used threshold for tropical cyclogenesis.
This, further investigated in later sections, already sheds light on to the still prevailing difficulties concerning the predictability of TT events. Wang et al. [11] state that, besides forecast errors of deep-layer shear and moisture in the mid-troposphere, interactions of several precursor features may serve as the main factor limiting the latter. Associated with this, the aim of this thesis is to infer the necessary physical structure of these PV precursor features which guarantee a sufficient environment for "successful" tropical transition scenarios. In this context, a recently developed algorithm [12] as well as the 3-D visualization software *Met.3D* is used to investigate the stalactite-like characteristics of the PV streamers associated with two case study examples. This visual analysis is highlighting the main part of this study. Additionally, ensemble forecasts of the European Centre for Medium-Range Weather Forecasts (ECMWF) will be investigated

concerning the difference in the structure of the respective PV anomalies leading to, or restricting TT.
In this study, Hurricane Leslie (2018) and Hurricane Paulette (2020) were chosen for several reasons. While characterized by rather unconventional storm tracks, Leslie and Paulette often encountered environments of high baroclinicity throughout their life cycles. Amplifying interactions of upper tropospheric and lower-level baroclinic zones facilitate the realization of the TT. The structural properties of the PV streamer, leading to the formation of the tropical characteristics, are the main driver for realizing the TT pathway, while also being capable of impeding it on the other hand. This is examined by combining the investigation of the ensemble weather forecast predictions concerning their respective CPS metrics and CI developments, together with the 3-D PV analysis using the already mentioned algorithm by Fischer et al. [12].

2 Background and Basics

The task is not to see what has never been seen before, but to think what has never been thought before about what you see everyday.

- Schrödinger, E

2.1 The Fundamental Equations of Atmospheric Dynamics

A closer look at the daily sky reveals that the atmospheric composition, which varies in space and time, is mostly dependent on the amount of water vapor given in the environment. Because stratospheric air is described by an almost completely dry air mass, this characteristic is especially important when it comes to the analysis of tropospheric dynamics.
Hence, this leads to a small modification of the original *ideal gas law*, or so-called *equation of state*

$$p = \rho R_d T_\nu \;\text{ or }\; p\alpha = \frac{p}{\rho} = R_d T_\nu. \tag{2.1}$$

Together with the dry-air gas constant R_d, the specific humidity q and the virtual temperature $T_\nu = T(1 + 0.61q)$, this equation describes the relation between pressure, temperature and density in the troposphere.
Furthermore, another governing equation which describes the motion of viscous fluid substances is the famous *Navier-Stokes equation*, which, regarding horizontal motion, can be examined as follows:

$$\frac{\mathrm{d}\vec{V}}{\mathrm{d}t} = -\frac{1}{\rho}\nabla_h p - f\vec{k} \times \vec{V} + \vec{F}_r. \tag{2.2}$$

While the left hand side describes the acceleration an air parcel would undergo in case of external forcing, the right hand side denotes these several forcing terms leading to the acceleration respectively. The first term on the right visualizes the pressure gradient force followed directly by the Coriolis force. The frictional force, denoted by the term $\vec{F}_r$, is mostly connected to the existence of turbulent eddies in the planetary boundary layer and the transport of momentum associated with it. Therefore it can be legitimately neglected when describing the dynamics in the upper troposphere.
One might consider the Eulerian form of the zonal component of the *Navier-Stokes equation* by multiplying equation (2.2) with the unit vector $\vec{i}$ and separating the partial derivative of u with respect to time

$$\frac{\partial u}{\partial t} = -u\frac{\partial u}{\partial x} - v\frac{\partial u}{\partial y} - w\frac{\partial u}{\partial z} - \frac{1}{\rho}\frac{\partial p}{\partial x} + fv + F_x. \tag{2.3}$$

This equation, describing the time rate of change of u at a fixed location in space, visualizes the Forces acting on the considered parcel more clearly. The local time rate of change is due to the horizontal and vertical advection (first three terms on the right), the pressure gradient force, the zonal component of friction and the Coriolis torque, which is acting on the meridional component of the flow.
Since the Navier-Stokes equation is not solvable analytically, scale analyses are often used in atmospheric sciences. The most simplest assumption concerning the movement of air parcels is the *Geostrophic Balance*, where we assume synoptic-scale motions. Because scale analysis reveals that the pressure gradient force and Coriolis force are the dominant terms in this case, one might consider the limiting case in which those two terms are in exact balance. This leads

to the equations of the so-called *Geostrophic Wind*, which is oriented parallel to the isobars

$$\vec{V}_g = \vec{k} \times \frac{1}{\rho f} \nabla p \tag{2.4}$$

$$u_g = -\frac{1}{\rho f}\frac{\partial p}{\partial y}; \qquad v_g = \frac{1}{\rho f}\frac{\partial p}{\partial x}. \tag{2.5}$$

For flows, which can approximately described by a state of geostrophic balance, the governing equation (2.2) can be simplified considerably. This we will also further examine by investigating the *Quasigeostrophic Theory* in section 2.2.

2.1.1 Geopotential Lines and Thickness

Because of centrifugal effects associated with the Earth's rotation, the shape of the Earth's surface is characterized by a small departure from a perfect sphere. Therefore the definition of the *Geopotential* is commonly used in meteorological sciences.

$$\vec{g} = -\nabla \Phi \tag{2.6}$$

It combines gravitational and centrifugal effects and therefore surfaces of constant geopotential are exactly aligned with the oblate surface of our planet. By defining the mean sea level as the surface of zero geopotential, Φ is related to the work which is required to lift a unit mass from sea level to a given altitude.
By using the gravitational constant at mean sea level ($g_0 = 9.80665\,\frac{\mathrm{m}}{\mathrm{s}^2}$) we are further able to define the *Geopotential Height*:

$$Z = \frac{\Phi(z)}{g_0} = \frac{1}{g_0}\int_0^z g \mathrm{d}z. \tag{2.7}$$

Using the hydrostatic assumption ($\partial p/\partial z = -\rho g$) and a small deviation in vertical distance, such that $\vec{g}$ can be described as a constant, the change in geopotential can be visualized as follows:

$$\mathrm{d}\Phi = g\mathrm{d}z \approx -\alpha \mathrm{d}p. \tag{2.8}$$

By regarding the geostrophic wind, described by equation (2.5) and written in pressure coordinates instead of height coordinates, we replace the pressure gradient by a geopotential height gradient

$$\vec{V}_g = \vec{k} \times \frac{g_0}{f} \nabla Z. \tag{2.9}$$

Hence, one could already recognize the importance of geopotential height for atmospheric sciences.
Following the hydrostatic assumption as well as the equation of state (2.1), we obtain

$$\mathrm{d}\Phi = \frac{-R_d T_v}{p}\mathrm{d}p \qquad\qquad \Phi_{up} - \Phi_{low} = -R_d \int_{p_{low}}^{p_{up}} T_v \mathrm{d}(\ln(p)). \tag{2.10}$$

Further Division by g_0 leads to the so-called *Hypsometric equation*

$$Z_{up} - Z_{low} = \frac{R_d}{g_0}\int_{p_{up}}^{p_{low}} T_v \mathrm{d}(\ln(p)) \tag{2.11}$$

which, in general, is characterized by an elaborated structure because of the virtual temperature on the right hand side of the equation. However, it can also be simplified by extracting the average virtual temperature over the layer of integration

$$\Delta Z = \frac{R_d \overline{T_v}}{g_0} \ln\left(\frac{p_{low}}{p_{up}}\right). \tag{2.12}$$

With this, one might see, that for two given pressure surfaces, the colder the average layer potential temperature, the smaller the thickness. Therefore, pressure decreases more rapidly with height in cold air in comparison to warm air. Hence, the thickness relates the structure of geopotential height on constant pressure surfaces to the temperature distribution and thus provides insight into the structure of a large variety of weather systems, such as tropical and extratropical cyclones.

2.1.2 The Thermal Wind

Since we are able to recognize a link between the geostrophic wind field and geopotential height via the geostrophic wind equation, the *vertical shear* of the geostrophic wind can be related to the difference in height between two given pressure levels.
The vertical shear of the geostrophic wind, or as it is called, the *Thermal Wind*, can be expressed as

$$\vec{V}_T = \vec{V}_{up} - \vec{V}_{low}. \tag{2.13}$$

Hence thermal wind is just describing the vertical shear of the geostrophic wind, the thermal wind itself is not a true wind.
In this context, one common technique is to change the coordinate system to *Natural Coordinates*. In this case, we are replacing the vectors $\vec{i}$ and $\vec{j}$ by $\vec{s}$ and $\vec{n}$, where $\vec{s}$ describes the unit vector parallel to the geostrophic flow, while $\vec{n}$ points in the normal direction with respect to the height contours. Hence, we recognize the form of the geostrophic wind as

$$V_g = \frac{g_0}{f}\frac{\partial Z}{\partial n}. \tag{2.14}$$

Furthermore, by using equation (2.12) one might derive the thermal wind relation in natural coordinates

$$V_T = \frac{R_d}{f}\ln\left(\frac{p_{low}}{p_{up}}\right)\frac{\partial \overline{T_v}}{\partial n}. \tag{2.15}$$

The thermal wind is therefore related to the horizontal temperature gradient.
Several observations have shown, that outside of the tropics the atmosphere is generally close to thermal wind balance [13]. Therefore, regions of strong horizontal temperature gradients are characterized by strong vertical wind shear. This on the other hand is detrimental to tropical cyclones as will be shown in later sections and therefore marks a critical quantity when it comes to the understanding of tropical and extratropical transition events over the North Atlantic Ocean.

2.1.3 Basic Concepts of Vorticity

Concerning the dynamics of extreme weather events associated with rotating air masses, expressed for example by extratropical and tropical storms, tornadoes or hurricanes, a new concept is often utilized by atmospheric scientists. *Vorticity*, which is a local measure of rotation about a given coordinate axis, will be further investigated in this section to provide the mathematical basis for understanding tropical and extratropical cyclone dynamics later on.
Relative vorticity, as it is defined, serves to describe the rotation in a fluid and is given by the curl of the velocity

$$\vec{\omega}_{rel} = \nabla \times \vec{V}. \tag{2.16}$$

One might also take the rotation of planet Earth itself into account, which then leads to the definition of *absolute voriticty* ζ_a. Considering only the vertical axis, as is common done in meteorology, leads to

$$\zeta_a = \left(\frac{\partial v}{\partial x} - \frac{\partial u}{\partial y}\right) + f. \tag{2.17}$$

Here, the first term on the right denotes the relative vorticity of the system, while $f = 2\Omega\sin(\phi)$ describes the vorticity due to Earth's rotation ($\Omega \approx 7.2921 \cdot 10^{-5}\,\mathrm{rad\,s^{-1}}$).

To gain a better understanding of the physical processes involved in the development of atmospheric circulation systems one might also consider the changes and drivers of vorticity. Hence, the *Vorticity Equation*, which is formed as a combination of horizontal momentum equations, will be further investigated.
The vorticity equation in isobaric, Cartesian coordinates can be written as

$$\underbrace{\frac{\partial \zeta_a}{\partial t}}_{\text{(a)}} = \underbrace{-\vec{V} \cdot \nabla \zeta_a}_{\text{(b)}} \underbrace{- \omega \frac{\partial \zeta_a}{\partial p}}_{\text{(c)}} \underbrace{- \left[\frac{\partial \omega}{\partial x} \frac{\partial v}{\partial p} - \frac{\partial \omega}{\partial y} \frac{\partial u}{\partial p} \right]}_{\text{(d)}} \underbrace{+ \zeta_a \frac{\partial \omega}{\partial p}}_{\text{(e)}} \underbrace{+ \left[\frac{\partial F_y}{\partial x} - \frac{\partial F_x}{\partial y} \right]}_{\text{(f)}}. \tag{2.18}$$

Several potential sources and sinks for absolute vorticity can be understood by studying the equation above. The local vorticity tendency (term a) is partly dependent on the horizontal vorticity advection (term b), as well as on the vertical advection of vorticity (term c). Furthermore one might have to consider the tilting of vorticity about the horizontal axes into the vertical (term d), the contribution of vortex stretching (term e) and several additional frictional processes (term f).
The magnitude of the vorticity gradient itself multiplied by the wind vector component in the direction of the just mentioned gradient determines the strength of the horizontal advection component. Since vertical velocities are often times weaker than the horizontal ones, the vertical vorticity component takes on a less relevant role in comparison to term b. Tilting in particular plays an important role in upper-level frontal zones, which are characterized both by strong horizontal gradients of vertical motion as well as by large vertical wind shear [14]. Whenever large horizontal vorticity components are accompanied by a horizontal vertical velocity gradient tilting of vorticity about a horizontal axis into the vertical is favored. However, we will see later that this is detrimental for tropical cyclogenesis as well, because heat and moisture are advected away from the system and further development is inhibited (see section 2.4).
The most dominant vorticity production term is visualized by term e in equation (2.18). By using the continuity equation

$$\frac{\partial u}{\partial x} + \frac{\partial v}{\partial y} + \frac{\partial \omega}{\partial p} = 0, \tag{2.19}$$

one can express this term as $-(\zeta + f)\nabla \cdot \vec{V}$. Therefore the spin-up of vorticity is not only proportional to the convergence and stretching of the vertical air column, it is also dependent on the amount of preexisting absolute vorticity. This describes why zones of cyclonic preexisting vorticity, such as fronts and troughs, serve as preferential sites for further growth of cyclonic vorticity. This can also be inferred by considering the analysis of the tropical transition process associated with tropical storm Leslie as described in section 5.1.1.

2.2 The Quasi-Geostrophic Analysis

The understanding of how the conservation of momentum, mass and energy is expressed in the atmosphere serves as a base in order to determine the relationships among temperature, pressure and velocity fields in the atmosphere itself. Therefore, one of the main goals of dynamic meteorology is to interpret the structure of large-scale atmospheric motions in a framework determined by the physical laws mentioned above. Considering the content of section 2, one might realize that the general investigation of atmospheric dynamics is quite demanding. However, for extratropical synoptic-scale motions the horizontal velocities are approximately geostrophic and thus the governing equations can be significantly simplified [13]. Almost geostrophic motions, or *Quasi-Geostrophic* motions, are much more simpler to analyze than tropical disturbances for example. Hence, an analysis of the prior serves as a reasonable starting point for our dynamical analysis. Furthermore, insights demonstrated in this chapter will also be used in later sections in order to gain a qualitative understanding of the dynamics involved in the formation of synoptic-scale weather systems.

2.2.1 Basic Equations and the Quasi-Geostrophic Approximation

The most fundamental assumption when it comes to the description of atmospheric dynamics considering the quasi-geostrophic approximation is that the Rossby number, which describes the ratio of inertial force to Coriolis force, is small (on the order of 0.1). In cases where this assumption holds we are allowed to neglect the ageostrophic velocity in some terms of the governing equations. However, this does not mean that the flow must be geostrophic in the first place. One important insight we will gain is that the ageostrophic contribution of motions in the quasi-geostrophic (QG) system is the most dominant driver considering the impact on our daily weather.
One further simplification will be the restriction to those parts of the atmosphere which lie above the planetary boundary layer, leading to the assumption of *frictionless* flow. This visualizes the neglection of frictional convergence in the planetary boundary layer, which naturally leads to vertical air motions, but which will not be of further consideration in the context of this theory. The vector form of the frictionless horizontal momentum equation is given as follows

$$\frac{\partial \vec{V}}{\partial t} = -\vec{V} \cdot \nabla_h \vec{V} - \omega \frac{\partial \vec{V}}{\partial p} - \nabla_h \Phi - f\vec{k} \times \vec{V}, \tag{2.20}$$

where the advection term is split into horizontal and vertical part respectively. Furthermore, ω is given as

$$\omega = \frac{\mathrm{d}p}{\mathrm{d}t} = \frac{\mathrm{d}p}{\mathrm{d}z}\frac{\mathrm{d}z}{\mathrm{d}t} \approx -\rho g w. \tag{2.21}$$

By further consideration of the horizontal advection term and partitioning of the horizontal wind in geostrophic and ageostrophic part

$$\vec{V}^h = \vec{V}_g^h + \vec{V}_{ag}^h, \tag{2.22}$$

we see that we are able to neglect some terms by regarding the expansion of the advection term into four parts: (i) $-\vec{V}_{ag}^h \cdot \nabla \vec{V}_g^h$, (ii) $-\vec{V}_{ag}^h \cdot \nabla \vec{V}_{ag}^h$, (iii) $-\vec{V}_g^h \cdot \nabla \vec{V}_{ag}^h$, (iv) $-\vec{V}_g^h \cdot \nabla \vec{V}_g^h$. Performing a scale analysis, as given in [14], we see that term (iv) is at least one magnitude larger than the other terms. A further scale analysis of the vertical advection due to ageostrophic motion reveals that its neglect relative to the geostrophic dynamics is feasible. Considering the *Beta*-approximation of the Coriolis parameter: $f = f_0 + \beta y$; $\beta = (\mathrm{d}f/\mathrm{d}y)|_{\Phi_0}$ one might also realize that the beta term is one order of magnitude smaller than f_0, which leads to the geostrophic wind relation given as follows:

$$\vec{V}_g = \frac{1}{f_0}\vec{k} \times \nabla\Phi. \tag{2.23}$$

By applying the quasi-geostrophic approximations, the total derivative with respect to time is given by

$$\frac{\mathrm{d}}{\mathrm{d}t} = \frac{\partial}{\partial t} + \vec{V}_g \cdot \nabla_h, \tag{2.24}$$

such that the momentum equation can be written as

$$\frac{\mathrm{d}\vec{V}_g}{\mathrm{d}t_g} = -\nabla\Phi - (f_0 + \beta y)\vec{k} \times \vec{V}. \tag{2.25}$$

Substituting $\nabla\Phi$, given by equation (2.23), and plugging the separation of velocity in geostrophic and ageostrophic contribution into equation (2.25) leads to

$$\frac{\mathrm{d}\vec{V}_g}{\mathrm{d}t_g} = f_0(\vec{k} \times \vec{V}_g) - (f_0 + \beta y)\vec{k} \times (\vec{V}_g + \vec{V}_{ag}), \tag{2.26}$$

which, after the expansion of the right-hand term, can be written as

$$\frac{\mathrm{d}\vec{V}_g}{\mathrm{d}t_g} = -f_0\vec{k} \times \vec{V}_{ag} - \beta y\vec{k} \times \vec{V}_g - \beta y\vec{k} \times \vec{V}_{ag}. \tag{2.27}$$

After the consideration of our first fundamental approximation, a small Rossby number, one recognizes that the third term on the right hand side is one magnitude smaller than the second one. This in the end leads to the final form of the quasi-geostrophic momentum equation

$$\frac{\mathrm{d}\vec{V}_g}{\mathrm{d}t_g} = -f_0\vec{k} \times \vec{V}_{ag} - \beta y\vec{k} \times \vec{V}_g. \tag{2.28}$$

Based on the latter, one can derive the continuity equation and the thermodynamic energy equation in quasi-geostrophic form:

$$\nabla_h \cdot \vec{V}_{ag} + \frac{\partial \omega}{\partial p} = 0 \tag{2.29}$$

$$\frac{\sigma p}{R}\omega + \frac{J}{C_p} = \frac{\mathrm{d}T}{\mathrm{d}t_g}, \tag{2.30}$$

with the diabatic heating rate J and $\sigma = -(RT/p)(\mathrm{d}(\ln(p))/\mathrm{d}p$.
With this in mind, one might further simplify the equations by assuming adiabatic motion and a stability parameter σ, which is a function only depending on pressure.
Besides the reduction of complexity to processes described by adiabatic and frictionless motion in hydrostatic balance and uniform static stability σ, the most dominant restriction is the description of motions characterized by a small Rossby number exclusively. However, considering certain weather phenomena, such as intense upper troughs, mid-latitude cyclones or tropical storms, the described systems are characterized by strong ageostrophic contributions to the flow field associated with a high Rossby number. This on the other hand symbolizes the absurdity of applying the quasi-geostrophic theory when one is willing to understand the dynamics of such weather systems.
However, it may be acceptable to use the QG approximations when describing the interactions of tropical cyclones in a larger-scale environment as well as when tropical systems have made landfall or significantly weakened in another way. Furthermore, the QG theory constitutes one of the building blocks when it comes to the understanding of vertical motion in the Earth's atmosphere. Further study of the quasi-geostrophic vorticity equation and its applications will show us, in which way we should understand the reasons for vertical motion dynamics in the atmosphere, which will then serve as the basis for understanding extratropical and tropical cyclogenesis events presented in chapter 3.
The derivation of the quasi-geostrophic vorticity equation follows the same steps already presented in chapter 2. By taking the curl of the horizontal QG momentum equations we end up with

$$\zeta_g = \frac{\partial v_g}{\partial x} - \frac{\partial u_g}{\partial y} = \frac{1}{f_0}\nabla^2\Phi = \frac{g_0}{f_0}\nabla^2 Z$$

$$\frac{\partial \zeta_g}{\partial t} = -\vec{V}_g \cdot \nabla(\zeta_g + f) + f_0\frac{\partial \omega}{\partial p}. \tag{2.31}$$

Therefore, the local time rate of change of relative vorticity can be inferred by regarding the geostrophic advection of geostrophic relative and planetary vorticity in combination with an analysis of the given amount of vortex stretching.
Considering the difference of equation (2.31) to the general form of the vorticity equation given by (2.18), one recognizes the absence of the advection, tilting and frictional terms. However, one simplification, which has to be highlighted, is the difference in the stretching term. In quasi-geostrophic consideration, $\frac{\partial \omega}{\partial p}$ is multiplied by f_0 only rather than being multiplied by $(\zeta + f)$ in the full vorticity equation. In the full equation the magnitude of stretching is proportional to the vorticity itself. Therefore zones of large preexisting vorticity are also sites for preferential vorticity growth, which serves as the base for an exponential feedback loop. In the QG perspective however, this effect is absent. Nevertheless we will further have to examine this characteristic when studying different cyclone types and their dynamics in later chapters, especially when it comes to the development of extratropical cyclones on frontal boundaries (section 2.5).

2.2.2 The Quasi-Geostrophic Omega Equation

In order to understand the processes leading to vertical motions as well as pressure and height tendencies, one might consider a combination of the vorticity equation and the first law of thermodynamics describing a closed system in omega and geopotential tendency. To replace the temperature by the vertical derivative of the geopotential in the quasi-geostrophic thermodynamic equation

$$\left(\frac{\partial}{\partial t} + \vec{V}_g \cdot \nabla\right) T = \frac{\sigma p}{R}\omega \tag{2.32}$$

one might use

$$\frac{\partial \Phi}{\partial p} = -\alpha = -\frac{RT}{p}. \tag{2.33}$$

Further division by $-\frac{p}{R}$ and use of $\chi \equiv \frac{\partial \Phi}{\partial t}$ leads to the following form:

$$\begin{aligned} \frac{\partial \chi}{\partial p} &= -\vec{V}_g \cdot \nabla\left(\frac{\partial \Phi}{\partial p}\right) - \sigma\omega \\ \nabla^2 \chi &= -f_0 \vec{V}_g \cdot \nabla\left(\frac{1}{f_0}\nabla^2\Phi + f\right) + f_0^2 \frac{\partial \omega}{\partial p}. \end{aligned} \tag{2.34}$$

Since this describes a system of two equations and two unknowns, it is straightforward to derive the *QG Omega Equation* which provides a conceptual framework for understanding the fundamental causes of daily weather

$$\underbrace{\left(\nabla^2 + \frac{f_0^2}{\sigma}\frac{\partial^2}{\partial p^2}\right)\omega}_{\text{(A)}} = \underbrace{\frac{f_0}{\sigma}\frac{\partial}{\partial p}\left[\vec{v}_g \cdot \nabla\left(\frac{1}{f_0}\nabla^2\Phi + f\right)\right]}_{\text{(B)}} + \underbrace{\frac{1}{\sigma}\nabla^2\left[\vec{V}_g \cdot \nabla\left(-\frac{\partial \Phi}{\partial p}\right)\right]}_{\text{(C)}}. \tag{2.35}$$

While looking demanding on the first glance, understanding the different parts of equation (2.35) is straightforward.
Term A, which serves as a kind of 3D-Laplacian acting on ω, switches the sign on the left hand side when considering sinusoidal patterns. This visualizes another simplification not necessarily valid in many situations. When applied however, this results in a $-\omega$ on the left hand side, which has the same sign as the vertical velocity w, since omega is defined to be negative for upward motion.
Term B describes the vertical derivative of the absolute geostrophic vorticity advection by the geostrophic wind, which is why it is often referred to as the *Differential Vorticity Advection* term. One might recognize that this term visualizes the role vorticity plays in the vertical rise and fall of air masses. Forcing for ascent is characterized by a cyclonic vorticity advection increasing with height or anticyclonic vorticity advection decreasing with height. Similarly anticyclonic vorticity advection increasing with height represents forcing for descent as well as cyclonic vorticity advection decreasing with height.
Term C, the *Thermal Advection Term*, is proportional to the Laplacian of the thickness advection. Here we are able to see that local maxima of warm advection represent forcing for ascent, whereas local maxima for cold advection lead to a forcing for descent. The Laplacian operator also leads to the fact that a local minimum of warm advection also leads to a forcing for descent. The derivations observed in the last subsection visualize how one is able to understand the effects of vorticity on to the vertical movement of air masses, which will also be used in later sections in order to understand the physical processes leading to extratropcial cyclone formation or tropical transition events. Nevertheless, one has to be aware of the fact that the QG forcing for a given sign of vertical motion does not guarantee that the same sign for real vertical motion will be observed. There are several processes which are not considered in the application of QG dynamics, such as orographic and fricitional effects. Additionally rising air does not guarantee precipitation or the formation of clouds, which should urgently kept in mind.

After the derivation of equation (2.35) we are able to understand the physical processes leading to the vertical movement of air masses.
As an appropriate starting point, we choose a situation in which the only contribution to the forcing is based on the first term on the right hand side (Term B). Considering the illustration presented by figure 1 and assuming that the 1000 mb geopotential height surface is equal to zero everywhere, one might recognize the existence of an upper westerly jet feature at a level of 500 mb. Equation (2.20) gives rise to the advective tendency of the zonal velocity component in the interior of region A. Since this leads to a clearly negative contribution, the tendency of advection is to reduce the wind speed in the vicinity of the jet entrance region. By further consideration of the geostrophic temperature advection one realizes that the geostrophic thermal advection is equal to zero in the A-region, since the geostrophic wind is parallel to the thickness contours in this particular case.

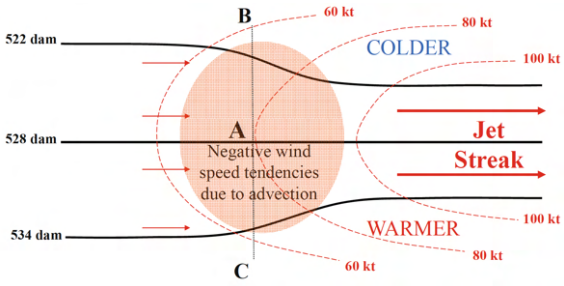

Fig. 1: Sketch of a Jet Entrance Region in the Northern Hemisphere [14]
Black lines denote (1000-500) mb *thickness contours in dekameters while red dashed lines characterize isotachs of the geostrophic wind, which direction is indicated by the arrows.*

This on the other hand leads to a weakening of vertical wind shear with time, since the zonal velocity at a level of 1000 mb remains constant. Therefore, a further inspection of the thermal wind equation $\left(u_g^U - u_g^L = -\frac{C}{f}\frac{\partial \overline{T}}{\partial y}\right)$ visualizes, that there has to be a mechanism, which has not been considered yet, in order to ensure the state of thermal wind balance, we are able to see in the atmosphere. Since geostrophic thermal advection is non-existent in this case, the thermal wind balance has to be maintained by the ageostrophic circulation. Figure 2 demonstrates the associated flow field. In case that the North-South thermal gradient has become too strong, such that the balance can not be maintained because of the weakened geostrophic shear, the thermal gradient itself has to weaken.

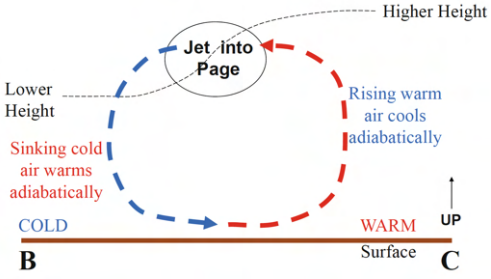

Fig. 2: Vertical Cross-Section as demonstrated in Figure 1 [14]

This further requires a cooling of the warm air and warming of the cool air. Hence, this is realized by adiabatic expansion and compression, therefore leading to warm air rising, becoming cooler and cool air sinking, thus becoming warmer. In Figure 3 we are able to recognize how the description of this vertical motion pattern is consistent with the QG omega equation given by (2.35). Cyclonic vorticity advection increasing with height coincides with the region of ascent next to the jet entrance region and vice versa. Therefore, following the QG assumptions, cyclonic and anticyclonic vorticity advection associated with the ascent and descent of air masses is realized in order to bring the atmosphere back toward a state of thermal wind balance.

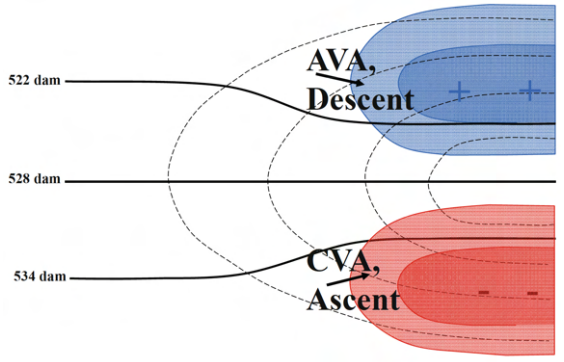

Fig. 3: Geostrophic Relative Vorticity Distribution associated with the Example shown in Figure 1 and 2 [14]
Red and blue regions denote cyclonic and anticyclonic vorticity advection respectively.

In summary, one might state, that the quasi-geostrophic theory explains the evolution of an ageostrophic secondary circulation in favor of counteracting the disruption of thermal wind balance by the primary circulation.
To neglect the second term on the right hand side of equation (2.35), the thermal advection term, would be naive when describing real world weather dynamics in general. Especially for intensive lower-tropospheric warm advection it would be very unlikely that differential vorticity advection could change the expected sign of the quasi-gestrophic omega contribution.
However, since there may also be a cancellation between the two right-hand terms given, it is rather problematic to consider both of them in isolation. A common way to tackle this issue is to recast the right-hand side into the so-called *Q-vector* form, in which the right side itself is related to the divergence of a vector field.

$$\left(\nabla^2 + \frac{f_0^2}{\sigma}\frac{\partial^2}{\partial p^2}\right)\omega = -2\nabla\cdot\vec{Q}$$
$$\vec{Q} = -\frac{R}{\sigma p}\left[\frac{\partial \vec{V}_g}{\partial x}\cdot\nabla\theta,\ \frac{\partial \vec{V}_g}{\partial y}\cdot\nabla\theta\right] \tag{2.36}$$

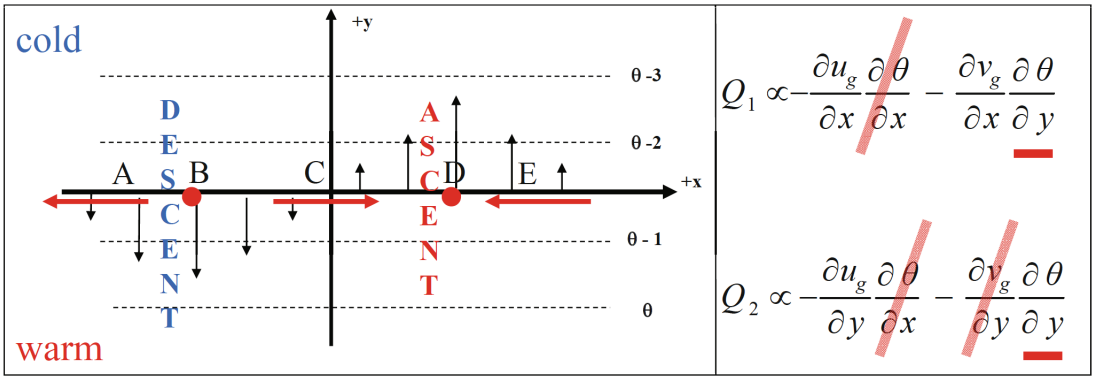

Fig. 4: Q-Vector Characterization describing an idealized Situation on dashed Isentropic Levels [14]
Black solid lines indicate the geostrophic winds whereas red arrows correspond to the Q-vectors. Red dots show positions for Q-vectors of magnitude zero.
The right side shows the individual components of the Q-vector while demonstrating vanishing parts marked by a red slash.

As shown in figure 4, forcing for descent can be emphasized in regions where Q-vectors diverge, whereas there will be ascent taking place in regions of converging Q-vectors. Besides the vanishing cancellation problem when using the Q-vector form, one primary advantage is demonstrated by the fact, that the Q-vector forcing can be computed on single levels rather than considering the differential aspect when using the *traditional* form of the QG omega equation.

2.2.3 Height Tendency Considerations

Further insights into the development and decay of weather systems can be gained by solving equation (2.34) for χ instead of ω. Following the same approach as in deriving the QG omega equation, it is straightforward to show that

$$\underbrace{\left[\nabla^2 + \frac{\partial}{\partial p}\left(\frac{f_0^2}{\sigma}\frac{\partial}{\partial p}\right)\right]\chi}_{A} = \underbrace{-f_0\vec{V}_g\cdot\nabla\left(\frac{1}{f_0}\nabla^2\Phi + f\right)}_{B}\underbrace{-\frac{\partial}{\partial p}\left[-\frac{f_0^2}{\sigma}\vec{V}_g\cdot\nabla\left(-\frac{\partial\Phi}{\partial p}\right)\right]}_{C} \tag{2.37}$$

holds.
Following the interpretation of the QG omega equation as well, Term B in equation (2.37) can be

understood as the absolute geostrophic vorticity advection, where cyclonic (anticyclonic) advection is associated with a tendency for height falling (rising). However, in case of an asymmetric vorticity distribution in an upper trough for example, term B will lead to a non-negligible amplification or decay. Hence, we expect that there is an import of cyclonic vorticity into the base of a through whenever a jet streak is located to the west of the through axis. This then further leads to an amplification and digging towards lower latitudes, which is why those configurations are commonly known as *Digging Troughs*. On the other hand, a wind speed maximum on the downstream side of the trough leads to a net export of vorticity associated with weakening and poleward movement of the system.
Term C of equation (2.37) is also strongly linked to amplification and decay of upper-level trough structures. This contribution, describing the differential thermal advection, can easily be understood by regarding figure 5. Due to the existence of a maximum of warm advection near the 700 mb pressure level the thickness of the layer must increase according to equation (2.10). Understanding of the geopotential height adjustment due to the presence of thermal advection maxima and geostrophic vorticity advection illustrates one of the building blocks when it comes to the differentiation between tropical and extratropical cyclones.

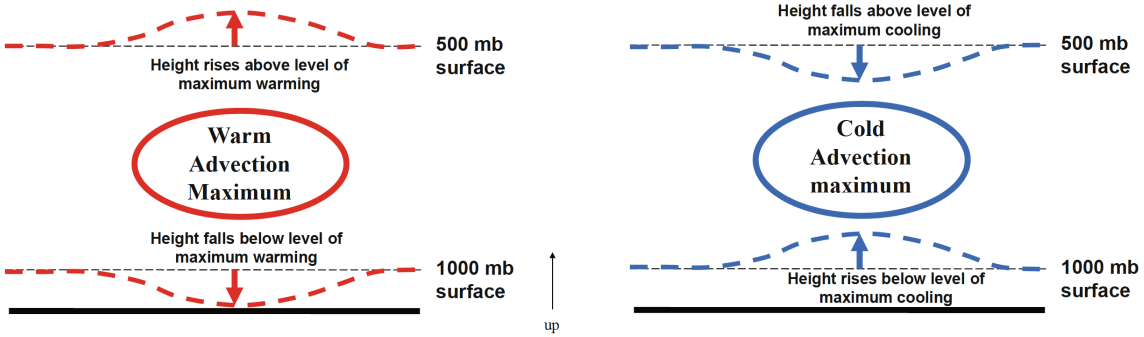

Fig. 5: Geopotential Height Changes due to Advection demonstrated by Term C in Equation (2.37) [14]

2.2.4 Quasi-Geostrophic Potential Vorticity and Impact of Diabatic Processes

In this section we will derive the QG potential vorticity equation and therefore one of the most powerful properties of PV, the conservation under certain flow conditions. Applying the chain rule in equation (2.37) and using the thermal wind relation given in (2.9), we end up with a scalar product of two perpendicular vectors

$$-\frac{\partial \vec{V}_g}{\partial p} \cdot \nabla \left(\frac{f_0^2}{\sigma} \frac{\partial \Phi}{\partial p} \right) = \frac{f_0}{\sigma} \vec{k} \times \nabla \frac{\partial \Phi}{\partial p} \cdot \nabla \frac{\partial \Phi}{\partial p} = 0. \tag{2.38}$$

Therefore, we can use this equation to replace term C in the height tendency equation (2.37), yielding

$$\frac{\partial}{\partial t} \left(\frac{1}{f_0} \nabla^2 \Phi + \frac{\partial}{\partial p} \left(\frac{f_0}{\sigma} \frac{\partial \Phi}{\partial p} \right) + f \right) + \vec{V}_g \cdot \nabla \left(\frac{1}{f_0} \nabla^2 \Phi + \frac{\partial}{\partial p} \left(\frac{f_0}{\sigma} \frac{\partial \Phi}{\partial p} \right) + f \right) = 0. \tag{2.39}$$

One might recognize that the quantity in the parentheses is conserved for adiabatic, frictionless and geostrophic flow. Hence, this quantity, also denoted as the *Quasi-Geostrophic Potential Vorticity*

$$q = \frac{1}{f_0} \nabla^2 \Phi + f + \frac{\partial}{\partial p} \left(\frac{f_0}{\sigma} \frac{\partial \Phi}{\partial p} \right), \tag{2.40}$$

fulfills the following conservation property

$$\frac{\mathrm{d}q}{\mathrm{d}t_g} = 0. \tag{2.41}$$

Therefore, the QG height tendency equation demonstrates a statement of quasi-geostrophic potential vorticity conservation, which will be further investigated in section 2.4.
The quasi-geostrophic framework provides concepts to qualitatively understand the vertical motion of air masses, as well as the development and decay of weather systems we are able to see in real nature. However, one of the most restrictive assumptions in the QG considerations is the adiabatic flow. Since the atmosphere is a chaotic system in which precipitation, condensational heating, etc. play a dominant role, it would be rather naive to neglect the importance of diabatic processes completely. Fortunately it is straightforward to re-include the diabatic term into the governing equations by simply retaining it in the derivations of equation (2.30) to (2.32), yielding

$$\left(\nabla^2 + \frac{f_0^2}{\sigma}\frac{\partial^2}{\partial p^2}\right)\omega = \frac{f_0}{\sigma}\frac{\partial}{\partial p}\left[\vec{V}_g \cdot \nabla\left(\frac{1}{f_0}\nabla^2\Phi + f\right)\right] + \frac{1}{\sigma}\nabla^2\left[\vec{V}_g \cdot \nabla\left(-\frac{\partial\Phi}{\partial p}\right)\right] - \frac{R}{C_p p\sigma}\nabla^2 J. \quad (2.42)$$

Hence, we see that the effect of the diabatic heating term is exactly similar to the thermal advection term in the adiabatic case and therefore a local maximum of heating (cooling) is consistent with forcing for ascent (descent).
Especially concerning the development of storm systems, latent heat release has led to dramatic model forecast failures in the past with the perhaps most famous example depicted by the *Presidents' Day* blizzard on February 19, 1979 [14]. Furthermore, diabatic contributions, such as the moistening of the mid-troposphere and the existence of deep-layer shear, still demonstrate the main features responsible for reducing the predictability of tropical transition events over the North Atlantic ([3] and [11]). Hence, further investigation of these features will also be presented in later sections.

2.3 The Isentropic Analysis

The isentropic analysis framework represents an alternate method for describing synoptic-scale motion fields while containing a multitude of insights and being conceptually simple at once. Describing a system using the isentropic analysis leads to results which are generally consistent with those obtained from the quasi-geostrophic analysis (section 2.2) for synoptic-scale motions. However, some assumptions needed to derive the governing equations of the quasi-geostrophic system are not required when using the isentropic analysis, which visualizes a significant advantage in comparison to the latter.
For describing adiabatic motions one might consider the first law of thermodynamics in the following form:

$$0 = C_p\,\mathrm{d}T - \alpha\,\mathrm{d}p. \quad (2.43)$$

Where C_p is the specific heat of air at constant pressure ($1004\,\mathrm{JK^{-1}kg^{-1}}$).
Integrating this formula with respect to pressure, while assuming a temperature θ at p_0, one obtains *Poisson's equation* for potential temperature

$$\theta = T\left(\frac{p_0}{p}\right)^{\frac{R}{C_p}}, \quad (2.44)$$

where R describes the dry-air gas constant ($\sim 287\,\mathrm{Jkg^{-1}}$).
Since entropy $s = C_p \ln(\theta) + \text{const.}$ is related to the potential temperature, lines of constant entropy coincide with lines of conserved potential temperature. This in the end is the reason for associating *Isentropes* with lines of constant potential temperature as well.
Following adiabatic motion air parcels are constraint to move along isentropic surfaces, which reflects one of the major advantages of using the isentropic analysis when it comes to the understanding of spatial development. In the isentropic framework one is able to trace the concrete path of several air parcels in three dimensions as long as adiabatic conditions are fulfilled.
To derive the form of the so-called *Isentropic Density*, which will be used in later chapters, we

consider a small fluid element of unit area and depth δz bounded above and below by isentropes θ_1 and θ_2, which is visualized by figure 6. The mass contained in this volume is given by

$$M = \rho \, \delta A \, \delta z. \tag{2.45}$$

By using the hydrostatic assumption, one can express this mass as

$$M = -\delta A \frac{\delta p}{g}. \tag{2.46}$$

Furthermore, one can use $\delta p = (\partial p / \partial \theta) \delta \theta$, where $\delta \theta$ denotes the isentropic depth of the parcel, to get

$$M = \frac{\delta A}{g} \left(-\frac{\partial p}{\partial \theta} \right) \delta \theta. \tag{2.47}$$

Finally dividing this equation by $\delta A \delta \theta$ leads to the form of the *Isentropic Density* σ

$$\sigma = -\frac{1}{g} \frac{\partial p}{\partial \theta}. \tag{2.48}$$

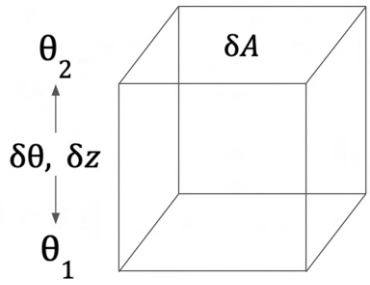

Fig. 6: Shape Identification of an Idealized Isentropic Volume

Therefore, this quantity is inversely proportional to the static stability $\partial \theta / \partial p$, which will be of further importance when describing the development of potential vorticity on isentropic surfaces (section 2.4).
When it comes to the description of vertical motion in atmospheric sciences one often refers to the pressure-coordinate vertical velocity ω. However, since potential temperature could undergo changes in time, one might state the equation for vertical air motion in isentropic coordinates as

$$\left(\frac{\mathrm{d}p}{\mathrm{d}t} \right)_{\theta=\text{const.}} \equiv \omega = \underbrace{\left(\frac{\partial p}{\partial t} \right)_{\theta}}_{\text{A}} + \underbrace{\vec{V} \cdot \nabla_{\theta} p}_{\text{B}} + \underbrace{\frac{\partial p}{\partial \theta} \frac{\partial \theta}{\partial t}}_{\text{C}}. \tag{2.49}$$

The three terms on the right hand side of the equation can be understood as follows:
Term A, describing the local pressure tendency, denotes the vertical movement of an isentropic surface at a fixed location.
Term B describes the pressure advection and also the most dominant term in many situations. However, since we are describing the system in isentropic coordinates, isobars coincide with isotherms and therefore term B can also be understood as the result of isentropic temperature advection.
Heating and Cooling effects associated with diabatic processes, like absorption, radiation or latent heat release lead to a vertical movement of isentropic surfaces. This on the other hand can also be described as the movement of an air parcel from one isentrope to another, which is also contained in equation (2.49) and further visualized by term C.
When applying the isentropic framework one has to be aware of the accuracy of the system itself, as well as of the present environmental conditions. Most of the time problems need to be considered in which the assumption of adiabatic motion does not hold. This contradicts the usage of the isentropic framework on first sight, which is why we'll now take a further look on to the natural development of a rising air parcel. Figure 7 demonstrates the evolution of an air parcel which is rising along a sloping isentrope starting at position 1. Following a dry adiabat, the parcel will rise until it reaches position 2, the lifting condensation level. As a result of this, further lifting will result in condensation of water vapor and interrelated latent heat release. This will lead to a more pronounced upward motion, following a moist adiabat, in comparison to the movement denoted by the path between point 1 and 2. Therefore, the violation of the adiabatic assumptions only results in an underestimation of the isentropic lift, which

legitimates the application of the isentropic framework to describe the development of a given weather system in a qualitative sense.

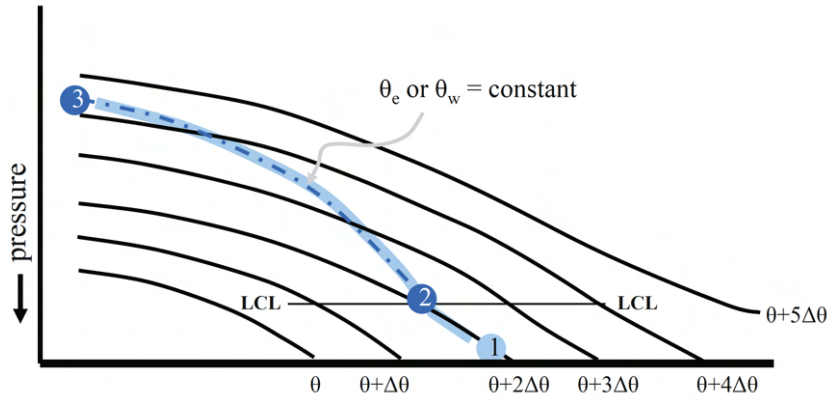

Fig. 7: Rising Motion of an Air Parcel depicted on Solid Black Isentropic Levels [14],[15]
Three different levels characterize the rising motion beginning on a dry isentrope (1), reaching the Lifting Condensation Level (LCL)(2) and further following a moist adiabat until point (3).

Comprizingly one can state that the isentropic analysis provides a conceptual, visual and easily understandable description of air parcel motion in three dimensional air flow, while the assumptions of a small Rossby number and horizontal uniform static stability are not needed. Hence it seems obvious why many forecasters prefer the isentropic framework to the traditional QG techniques.

2.4 Potential Vorticity Theory and the PV Framework

When it comes to the description of atmospheric dynamics there are many different frameworks which can be utilized to provide a better understanding of the processes involved. One of such, described as the Potential Vorticity framework, became comparably widespread in the late 20th century because of a series of extraordinary papers published by Hoskins et al. (1985) [14].

2.4.1 Potential Vorticity and the PV Tendency Equation

When studying the quasi-geostrophic height tendency equation in section 2.2, we see that the thermal wind relation serves as a pre-condition for the conservation of quasi-geostrophic potential vorticity. While QGPV is conserved following geostrophic, adiabatic and frictionless motion, it is also possible to define other forms of potential vorticity, which were introduced earlier and are more generally conserved.
One of the first analyses of potential vorticity is based on the work of Rossby (1940) and Ertel (1942), describing PV as

$$PV = \frac{1}{\rho}\vec{\eta} \cdot \nabla\theta. \tag{2.50}$$

In this case, $\vec{\eta}$ denotes the three-dimensional absolute vorticity vector, ρ describes the density and θ the potential temperature respectively.
Further consideration of equation (2.50) in isentropic coordinates, while applying the hydrostatic assumption, results in the following form of the PV:

$$PV = -g(\zeta_{a\theta})\frac{\partial\theta}{\partial p}, \tag{2.51}$$

where $\zeta_{a\theta}$ denotes the three-dimensional absolute vorticity on an isentropic surface.
From this equation one might understand PV as the vorticity that the air would have, if it were adiabatically adjusted to a reference latitude (characterized by $\zeta_{a\theta}$) and static stability ($\partial\theta/\partial p$).

This section is used to visualize the advantages and ways in which the given definition of PV can be used to analyze atmospheric dynamics and certain weather phenomena in greater detail. When describing the dynamics and time development of atmospheric systems one generally starts by regarding the governing equation of fluid dynamics, the Navier-Stokes-equation (2.2). Using the so-called *Montgomery Streamfunction*

$$M = (C_p T + gZ)_\theta \,, \tag{2.52}$$

as well as considering the problem in an isentropic framework, the horizontal momentum equations may be written as

$$\left(\frac{\partial}{\partial t} + u\frac{\partial}{\partial x} + v\frac{\partial}{\partial y} + \dot{\theta}\frac{\partial}{\partial \theta}\right) u - fv + \frac{\partial M}{\partial x} - F_x = 0 \tag{2.53}$$

$$\left(\frac{\partial}{\partial t} + u\frac{\partial}{\partial x} + v\frac{\partial}{\partial y} + \dot{\theta}\frac{\partial}{\partial \theta}\right) v + fu + \frac{\partial M}{\partial y} - F_y = 0. \tag{2.54}$$

Here, F_x and F_y denote the frictional force components in zonal and meridional directions respectively.
Cross differentiating equation (2.53) and (2.54) provides the isentropic vorticity equation

$$\frac{\partial \zeta_{a\theta}}{\partial t} + \frac{\partial}{\partial x}\left[u\zeta_{a\theta} + \dot{\theta}\frac{\partial v}{\partial \theta} - F_y\right] + \frac{\partial}{\partial y}\left[v\zeta_{a\theta} - \dot{\theta}\frac{\partial u}{\partial \theta} + F_x\right] = 0, \tag{2.55}$$

which should also be considered in vector form

$$\frac{\partial \zeta_{a\theta}}{\partial t} + \nabla \cdot \left(\vec{V}\zeta_{a\theta}\right) + \vec{k} \cdot \nabla_\theta \times \left(\vec{F} - \dot{\theta}\frac{\partial \vec{V}}{\partial \theta}\right) = 0. \tag{2.56}$$

To obtain the conservation laws associated with this equation one might rewrite equation (2.56) in the form of a continuity equation

$$\frac{\partial \zeta_{a\theta}}{\partial t} + \nabla \cdot \vec{j} = 0, \tag{2.57}$$

where $\vec{j}$ takes the form of

$$\vec{j} = (u\zeta_{a\theta}, v\zeta_{a\theta}, 0) + \left(\dot{\theta}\frac{\partial v}{\partial \theta}, -\dot{\theta}\frac{\partial u}{\partial \theta}, 0\right) + (-F_y, F_x, 0). \tag{2.58}$$

In general, a conservation relation for the mixing ratio of any arbitrary quantity χ can be written as

$$\frac{\partial(\sigma\chi)}{\partial t} + \nabla\vec{j} = \sigma S. \tag{2.59}$$

In this case, S represents all sources and sinks of χ, σ is the isentropic density, which we already derived in equation (2.48), and $\vec{j}$ represents the flux vector given by

$$\vec{j} = (u\sigma\chi, v\sigma\chi, \dot{\theta}\sigma\chi) + (-F_y, F_X, 0). \tag{2.60}$$

Furthermore, choosing χ as

$$\chi = \frac{\zeta_{a\theta}}{\sigma} \tag{2.61}$$

the amount of isentropic absolute vorticity per mass of dry air, we are able to derive the potential vorticity tendency equation.
Considering PV with the help of equation (2.48)

$$PV = \frac{\zeta_{a\theta}}{\sigma} = -g\frac{\partial \theta}{\partial p}\zeta_{a\theta} \tag{2.62}$$

and evaluating equation (2.59), while regarding $\chi = PV$, yields

$$\frac{\partial(\sigma PV)}{\partial t} + \frac{\partial}{\partial x}\left[u\sigma PV + \dot{\theta}\frac{\partial v}{\partial \theta} - F_y\right] + \frac{\partial}{\partial y}\left[v\sigma PV - \dot{\theta}\frac{\partial u}{\partial \theta} + F_x\right] = 0. \tag{2.63}$$

With the help of the latter mathematical statement it is straightforward to show that the full PV tendency equation can be obtained by

$$\begin{aligned}
\frac{\mathrm{d}PV}{\mathrm{d}t} &= -g\frac{\partial\theta}{\partial p}\zeta_{a\theta}\frac{\partial\dot{\theta}}{\partial\theta} + g\frac{\partial\theta}{\partial p}\left[\frac{\partial\dot{\theta}}{\partial x}\frac{\partial v}{\partial\theta} - \frac{\partial F_y}{\partial x} - \frac{\partial\dot{\theta}}{\partial y}\frac{\partial u}{\partial\theta} + \frac{\partial F_y}{\partial x}\right] \\
\frac{\mathrm{d}PV}{\mathrm{d}t} &= \underbrace{-g\frac{\partial\dot{\theta}}{\partial p}\zeta_{a\theta}}_{\mathrm{A}} + \underbrace{g\frac{\partial\theta}{\partial p}\vec{k}\cdot\left(\nabla\dot{\theta}\times\frac{\partial\vec{V}}{\partial\theta}\right)}_{\mathrm{B}} + \underbrace{g\frac{\partial\theta}{\partial p}\vec{k}\cdot(\nabla\times\vec{F})}_{\mathrm{C}}.
\end{aligned} \tag{2.64}$$

As denoted by the visualized parentheses, one might separate the right hand side of equation (2.64) in *Vertical Diabatic* (A), *Shear Diabatic* (B) and *Frictional* (C) PV tendency, respectively. The first term on the right hand side of equation (2.64) can easily be understood by considering a scenario where a particular heating region is given in the atmosphere while neglecting vertical isentropic shear and frictional influences. As regarded in the PV framework, the presence of a heating region would lead to an increased vertical spacing of the isentropes above the heating maximum and decrease of vertical spacing below. This however, while connected to the static stability of the respective region, results in a negative contribution of $\partial\dot{\theta}/\partial p$ in term A. Furthermore, assuming that the processes are taking place in the Northern Hemisphere, divergence aloft also leads to a decrease in vorticity by considering $\zeta_{a\theta}$. In summary, the existence of a heating region in the atmosphere would lead to negative PV advection aloft and positive PV advection below the heating maximum, indicated by equation (2.64). Term B is strictly connected to the asymmetry of isentropes. A departure of the vorticity vector from its vertical orientation might be the result of vertical shear presence. This however leads to a distortion of regions characterized by negative PV reduction aloft and the associated region of positive PV growth below a given heating maximum. The effect described by term B, demonstrating the advection of heat away from the system due to the existence of vertical wind shear, clearly depicts one critical characteristic when considering the differences in extratropical and tropical cyclones.
Generally, this equation, which describes the temporal evolution of PV as a result of diabatic effects, can be used to understand the conservation property of potential vorticity itself. Hence, in the absence of diabatic heating ($\dot{\theta} = 0$), while also neglecting frictional forces ($F = 0$), all three terms on the right hand side of equation (2.64) vanish and so PV is conserved following the quasi-two-dimensional flow on isentropic surfaces.

2.4.2 The Dynamic Tropopause and Stratospheric Influence

Concerning equation (2.51), PV is proportional to the product of absolute vorticity and static stability. Due to their characteristically high static stability one might expect to find large values of PV in the stratosphere and in polar regions as well.
As will be described in later sections (2.5, 2.6), situations, in which stratospheric air is adiabatically stretched to the point where the static stability is similar to values commonly measured in the troposphere, are not rarely observed. Such developments are associated by a large amount of relative vorticity advection due to the conservation property of PV mentioned in section 2.4. Hence, these processes led several atmospheric scientists, most notably Kleinschmidt (e.g., Eliassen and Kleinschmidt 1957), regard the stratospheric PV reservoir as the "producing mass" of cyclonic disturbances in the troposphere. The induced velocity field which results of such a PV anomaly is presented in figure 8.

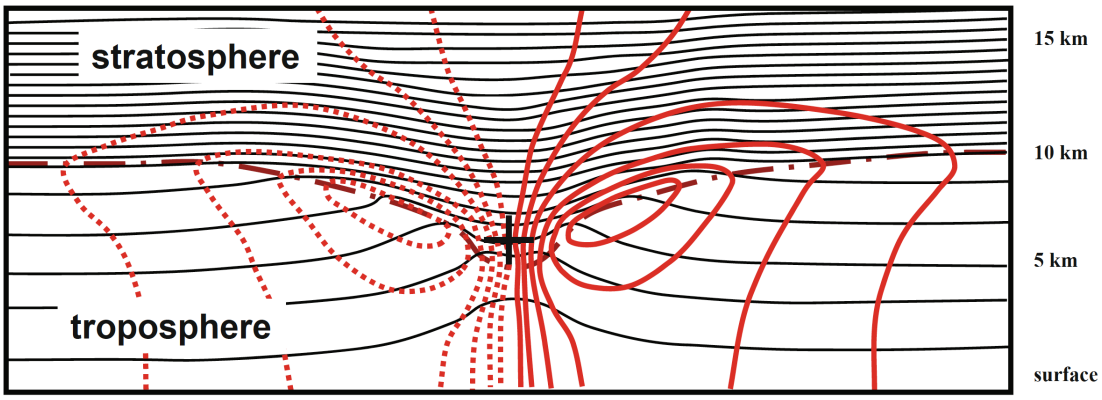

Fig. 8: Demonstration of an Idealized Isentrope Distribution (Black Solid Lines) [14] adapted from [16]

Besides the obvious difference in static stability between Stratosphere and Troposphere a cyclonic PV anomaly, denoted by the black plus sign, is visualized. Red contours are denoting the section-normal wind speed. Solid lines characterize positive values where as dotted lines visualize negative wind speed.

One widely used value when it comes to the understanding of atmospheric processes is the level of the tropopause. And here the PV framework provides a convenient way of defining this quantity. Because of the high static stability in the stratosphere in comparison to the troposphere, one might suggest that the tropopause can be identified as an isosurface of potential vorticity. Therefore we define the *Dynamic Tropopause* as the 2.0 PVU surface of the atmosphere, where $1\,\mathrm{PVU} = 10^{-6}\,\mathrm{Kkg^{-1}m^2s^{-1}}$ denotes one *Potential Vorticity Unit*.

2.5 Weather Fronts

2.5.1 Frontal Dynamics

In section 2.2 we already emphasized that geostrophic advections can disrupt thermal wind balance. However, ageostrophic motions come about in response in order to bring the atmosphere back to thermal wind balance. Frontogenesis is associated with a disruption of thermal wind balance and therefore an ageostrophic *Frontal Circulation* has to arise. Nevertheless, because of the sub-synoptic cross-front length scale, it would be naive to use QG theory in order to describe frontal dynamics. Therefore, a modified form of QG theory, known as *Semigeostrophic* theory, was developed specifically to diagnose the dynamics of frontal zones.
In this section a framework will be presented describing the ageostrophic frontal circulations in *Boussinesq Approximation*. Therefore, differences in density will only be considered in terms multiplied by the Earth's acceleration g, while following the assumption that the differences in inertia are negligible. Height will be used as vertical coordinate and hence the basic state of the atmosphere will be a function of height only, modified by small perturbations

$$\phi' \equiv \frac{p - p_0(z)}{\rho_0};\ \theta' = \theta - \theta_0(z). \tag{2.65}$$

The frictionless momentum equations in the Boussinesq form are given by

$$\begin{aligned} \frac{\mathrm{d}u}{\mathrm{d}t} - fv + \frac{\partial \phi'}{\partial x} &= 0 \\ \frac{\mathrm{d}v}{\mathrm{d}t} + fu + \frac{\partial \phi'}{\partial y} &= 0. \end{aligned} \tag{2.66}$$

Furthermore, the buoyancy as well as the thermodynamic equation can be derived as

$$\begin{aligned} b &\equiv \frac{g\theta'}{\theta_0(z)} = \frac{\partial \phi'}{\partial z} \\ \frac{\mathrm{d}b}{\mathrm{d}t} &= -w\frac{g}{\theta_{00}}\frac{\mathrm{d}\theta_0}{\mathrm{d}z} = -wN_0^2, \end{aligned} \tag{2.67}$$

with the Brunt-Väsiälä frequency N_0^2 and the basic-state potential temperature at the surface θ_{00}.
If we use a constant value of the Coriolis parameter f when defining the geostrophic wind, the geostrophic wind is nondivergent. Furthermore, because the front-parallel wind in particular is assumed to be geostrophic, based on one of the leading pre-conditions (a small Rossby number), we can further investigate

$$\begin{aligned} \frac{\partial u}{\partial x} + \frac{\partial v}{\partial y} &= 0 \\ \frac{\partial v_{ag}}{\partial y} + \frac{\partial w}{\partial z} &= 0. \end{aligned} \tag{2.68}$$

Based on our analysis we are not able to approximate the across-front flow as geostrophic. In order to obtain a state of equilibrium the cross-front thermal gradient has to be in thermal wind balance with the vertical shear of the along-front geostrophic wind component:

$$f\frac{\partial u_g}{\partial z} = -\frac{\partial b}{\partial y}. \tag{2.69}$$

As described above, the cross-front temperature gradient is close to a state of thermal wind balance. Hence, changes or perturbations concerning the strength of the mentioned gradient will lead to a disruption of the balance, therefore giving rise to ageostrophic circulations. One might further use the geostrophic wind relation in order to expand the total derivatives given in (2.66)

$$\frac{\partial u_g}{\partial t} + u_g\frac{\partial u_g}{\partial x} + v_g\frac{\partial u_g}{\partial y} + v_{ag}\frac{\partial u_g}{\partial y} + w\frac{\partial u_g}{\partial z} - fv_{ag} = 0. \tag{2.70}$$

This equation, describing the development of the front-parallel wind component u, also includes ageostrophic advections limited to the cross-front vertical components. This however demonstrates an important departure from quasi-geostrophic dynamics. It is the frontal circulation itself, which favors a modification of the temperature and momentum fields resulting from advective processes, due to the vertical and cross-front ageostrophic flows. The corresponding form of the thermodynamic equation reflects similar considerations:

$$\begin{aligned} 0 &= \frac{\partial b}{\partial t} + u_g\frac{\partial b}{\partial x} + v_g\frac{\partial b}{\partial y} + v_{ag}\frac{\partial b}{\partial y} + w\frac{\partial b}{\partial z} + wN_0^2 \\ \frac{\mathrm{d}}{\mathrm{d}t}\left(\frac{\partial b}{\partial y}\right) &= -\underbrace{\frac{\partial u_g}{\partial y}\frac{\partial b}{\partial x} - \frac{\partial v_g}{\partial y}\frac{\partial b}{\partial y}}_{Q_2} - \frac{\partial v_{ag}}{\partial y}\frac{\partial b}{\partial y} - \frac{\partial w}{\partial y}\frac{\partial b}{\partial z} - \frac{\partial w}{\partial y}N_0^2, \end{aligned} \tag{2.71}$$

where the first two right-hand terms represent the cross-front component of the Q-vector.
By differentiating (2.70) with respect to z we end up with an equation describing the time rate of change of vertical shear of the along-front geostrophic wind component:

$$\frac{\mathrm{d}}{\mathrm{d}t}\left(f\frac{\partial u_g}{\partial z}\right) = -\underbrace{\frac{\partial u_g}{\partial y}\frac{\partial b}{\partial x} - \frac{\partial v_g}{\partial y}\frac{\partial b}{\partial y}}_{Q_2} - f\frac{\partial v_{ag}}{\partial z}\frac{\partial u_g}{\partial y} - f^2\frac{\partial v_{ag}}{\partial z} + \frac{\partial w}{\partial z}\frac{\partial b}{\partial y}. \tag{2.72}$$

One might recognize that Q_2 appears on the right hand side of both equations ((2.71) and (2.72)). This visualizes the fact that geostrophic advections can disrupt thermal wind balance

as described by the appearance of the Q-vectors in the thermal and shear gradient tendency equations. In order to step further, we will take the sum of equation (2.71) and (2.72) while using the thermal wind balance inferred in equation (2.69). This in the end gives rise to a diagnostic equation that includes a forcing term, describing how geostrophic advections may disrupt thermal wind balance, and an ageostrophic circulation, which is exactly the response needed to maintain balance. To further simplify the governing equation one might introduce an ageostrophic streamfunction ψ_{ag}, that is everywhere parallel to the ageostrophic flow in the y–z plane

$$v_{ag} = -\frac{\partial \psi_{ag}}{\partial z};\ w = \frac{\partial \psi_{ag}}{\partial y}. \tag{2.73}$$

Using our streamfunction approach in order to modify the sum of equation (2.71) and (2.72), we arrive at the *Sawyer–Eliassen Equation*

$$\left(N_0^2 + \frac{\partial b}{\partial z}\right)\frac{\partial^2 \psi_{ag}}{\partial y^2} f\left(f - \frac{\partial u_{ag}}{\partial y}\right)\frac{\partial^2 \psi_{ag}}{\partial z^2} - 2\frac{\partial b}{\partial y}\frac{\partial^2 \psi_{ag}}{\partial z \partial y} = 2Q_2. \tag{2.74}$$

With this equation we are able to state arguments describing atmospheric dynamics associated with a wide range of frontal systems by using the insights we could gain in section 2.2. The purpose of equation (2.74) becomes clear when restricting to the isentrope-normal component of the Q-vector Q_n. If Q_n points toward warmer isentropes the geostrophic flow is acting in a frontogenetical sense. In situations where Q_n is directed toward colder isentropes however, the geostrophic flow is acting frontolytically.
In cases where the thermal gradient tightens (for example by the input of solar radiation on the already warmer side of the front, while not warming the pre-colder side for an equal amount), the magnitude of Q_2 increases, because of a strengthened temperature gradient. This requires an even stronger ageostrophic frontal circulation and a feedback is established.
The reason why fronts remain, rather then getting "dissolved" by the counteracting effects of the secondary circulation is based on the weak vertical motions near the surface. Hence, adiabatic temperature changes are comparably small in the lower troposphere and thus several mechanisms work in order to intensify the front near the surface. This includes the primary geostrophic frontogenesis described by the forcing term Q_2, as well as the ageostrophic cross-frontal circulation. This on the other hand explains why we commonly observe the most intense fronts near the surface. In similar situations, the ageostrophic circulation is not able to counteract the primary frontogenesis.

2.5.2 Middle and Upper Level Frontal Zones

As discussed in the last section, mature frontal zones are often most intense near the surface and weaken with height. However, intense upper-level fronts can form as well. One major difference is demonstrated by the tilting component, which unlike considering the dynamics near the surface, can have a significant impact regarding the formation of upper fronts.
The reason for further investigation of upper-level frontal development is related to the role of these systems in exchange of air between the troposphere and stratosphere, due to the associated ageostrophic circulation. As investigated in section 2.4, jet streaks and upper-level frontal circulations can pull stratospheric air with large potential vorticity towards the surface, resulting in stretching and upper trough development.
Upper-level frontal systems require the interaction between the primary forcing due to confluence, shear, etc. and the associated secondary circulation that arises in response to that forcing. There are some situations in which a folding of the tropopause can occur, which is almost invariably associated with the existence of upper-level frontal zones in the vicinity of the folding region. While the ageostrophic circulation connected to the front can lead to the formation of tropopause folding, it is highly expected that an upper trough would form in the surrounding of the jet exit region associated with the front. This mechanism is highly important for describing

the processes leading to tropical transition events and will also be further investigated when considering case study examples in section 5.

2.6 A Simple Baroclinic Instability Analysis

The atmosphere as a whole is characterized by a large variety of instabilities including upright and slantwise convective instability, small-scale Kelvin-Helmholtz instabilities that arise in the presence of large vertical wind shear and *Baroclinic Instabilities*. These different kinds of instabilities however, are distinguishable by taking the energy perspective into consideration. If the energy source needed for further development of the given perturbations is based on the kinetic energy of the background flow, the instability can be described as *Barotropic*. Baroclinic instabilities on the other hand require a baroclinic environment while exerting energy from the basic-state potential energy source.
In this chapter we will see how the static stability of the atmosphere and amplitude of certain perturbations are related to the further evolution of the perturbations themselves. These aspects can already be encountered by considering the *Eady-Model*, one of the simplest models describing baroclinic instability growth. Following observational studies it has been shown that cyclogenesis events are associated with the interaction of preexisting upper- and lower-tropospheric disturbances, which often take the form of cyclonic vorticity maxima associated with depressions of the dynamic tropopause. Therefore this chapter should shed light on the processes leading to the evolution of PV-streamers accompanying with those systems in the first place.
In order to analyse the growth of instabilities on a simple baroclinic flow, one might utilize the Boussinesq equations on a f plane again in order to maximize simplicity. The governing equations assuming adiabatic, frictionless, hydrostatic flow under f-plane QG and Boussinesq conditions are given by

$$\begin{aligned}
\frac{\partial u_g}{\partial t} + u_g\frac{\partial u_g}{\partial x} + v_g\frac{\partial u_g}{\partial y} &= f_0 v_{ag},\\
\frac{\partial v_g}{\partial t} + u_g\frac{\partial v_g}{\partial x} + v_g\frac{\partial v_g}{\partial y} &= -f_0 u_{ag},\\
\frac{\partial u_{ag}}{\partial x} + \frac{\partial v_{ag}}{\partial y} + \frac{\partial w}{\partial z} &= 0,\\
\frac{\partial b}{\partial t} + u_g\frac{\partial b}{\partial x} + v_g\frac{\partial b}{\partial y} &= -N_0^2 w,\\
\frac{\partial \Phi}{\partial z} &= b.
\end{aligned} \tag{2.75}$$

As indicated by figure 9, the domain of consideration is bounded by a rigid lid at $z = H$ on top. It possesses a flat lower boundary at $z = 0$, extends indefinitely in the meridional direction and has periodic lateral boundary conditions in the zonal direction (at $x = 0, L$.)
Further simplifications will be obtained by neglecting meridional variations in the disturbance field due to the chosen symmetry of the domain. Following simplicity, we assume a basic-state flow in hydrostatic and geostrophic balance of the form

Fig. 9: Zonal Area used for the Baroclinic Analysis in the Eady Model

$$u_g = U_g(z) = U\frac{z}{H}, \tag{2.76}$$

where U is a constant parameter denoting the maximum speed of the westerly current at $z = H$. Regarding the thermal wind relation we arrive at

$$\frac{\partial U_g}{\partial z} = \frac{U}{H} = \text{const} = -\frac{1}{f_0}\frac{\partial B}{\partial y}, \tag{2.77}$$

where B, the buoyancy, is obtained by

$$B(y) = -\frac{f_0 U}{H} y$$
$$B = \frac{\partial \Phi}{\partial z}. \tag{2.78}$$

Therefore, the basic-state geostrophic streamfunction takes the form

$$\Phi(y,z) = -f_0 \frac{U}{H} yz. \tag{2.79}$$

For further investigation of the complete set describing zonal wind, buoyancy and pressure, one has to include disturbances as well, leading to

$$\begin{aligned} u &= U_g + u_g^{'} + u_{ag}^{'} & v &= v_g^{'} + v_{ag}^{'};\ \ w = w^{'}(x,z,t) \\ b &= B(y) + b^{'}(x,z,t) & \phi &= \Phi(y,z) + \phi^{'}(x,z,t). \end{aligned} \tag{2.80}$$

Hence we have chosen a domain which is unbounded in the meridional direction, the solutions of interest are restricted to the x-z plane. Therefore, $u_g^{'} = 0$ and the equations (2.75) require that $v_{ag}^{'} = 0$ holds as well and the final set of equations takes the form

$$\begin{aligned} \frac{\partial v_g^{'}}{\partial t} + U_g \frac{\partial v_g^{'}}{\partial x} &= -f_0 u_{ag}^{'}, \\ \frac{\partial b^{'}}{\partial t} + U_g \frac{\partial b^{'}}{\partial x} &= -v_g^{'} \frac{\partial B}{\partial y} - N_0^2 w^{'}, \\ \frac{\partial u_{ag}^{'}}{\partial x} + \frac{\partial w^{'}}{\partial z} &= 0, \\ f_0 + \frac{1}{f_0} \nabla_h^2 \phi^{'} + \frac{f_0}{N_0^2} \left(\frac{\partial^2 \phi^{'}}{\partial z^2} \right) &= q. \end{aligned} \tag{2.81}$$

By considering the buoyancy equation in (2.81) we can infer that variations in the disturbance temperature field can be the result of either advection of the basic-state temperature field or might be the consequence of vertical air motions. Regarding the potential vorticity field we see that this can be understood as a constant basic-state value f_0, modified by vorticity in the meridional perturbation geostrophic flow, as well as by stability anomalies characterized by the last term on the right hand side of the equation.
In order to apply a stability analysis to a given problem one might commonly start with testing solutions of normal-mode form. If we could find a set of these modes, which maintain a fixed structure in time characterized by instability, we state that the one, exhibiting the largest growth rate, would dominate with time.
One advantageous guess is the assumption of sinusoidal wave-like solutions of the form

$$\phi^{'} = \mathrm{Re}\left[\hat{\phi}(z) \mathrm{e}^{\mathrm{i}k(x-ct)} \right]. \tag{2.82}$$

Here, the vertical structure of the solution is given by $\hat{\phi}(z)$, while the part containing the wave-like structure is given by the exponent. Furthermore, $k = 2\pi/\lambda$ is describing the wavenumber, whereas c denotes the complex phase speed of the wave ($c = c_r + \mathrm{i}c_i$). Hence, the growing or decaying part of the solution can be isolated:

$$\phi^{'}(t) = \mathrm{e}^{kc_i t}. \tag{2.83}$$

This statement gives rise to the fact that amplifying solutions depend on the existence or development of a nonzero imaginary component of the phase speed.

To further analyze how instabilities would affect the interior domain in the Eady model we will take a look on to the potential vorticity relation. By regarding the Boussinesq as well as the quasi-geostrophic framework under consideration of the f-plane assumption, we end up with

$$q = f_0 + \frac{1}{f_0}\nabla_h^2\phi + \frac{f_0}{N_0^2}\left(\frac{\partial^2\phi}{\partial z^2}\right). \tag{2.84}$$

Where the full expression for ϕ is given by

$$\phi = \Phi(y,z) + \phi^{'}(x,z,t) = -f_0\frac{U}{H}yz + \phi^{'}. \tag{2.85}$$

This can then further be used to rewrite the quasi-geostrophic potential vorticity equation

$$q = f_0 + \frac{1}{f_0}\nabla_h^2\phi^{'} + \frac{f_0}{N_0^2}\left(\frac{\partial\phi^{'}}{\partial z^2}\right). \tag{2.86}$$

Since the basic-state $\Phi-$field is linear in y and z, one might understand this equation in the form of $q = Q + q^{'}(x,z,t)$, where $Q = f_0$ denotes the basic-state PV, whereas $q^{'}(x,z,t)$ takes the given disturbances into account. Since we are studying the development of disturbances which would grow spontaneously, the initial perturbation amplitude is infinitesimally small. Therefore, $q^{'}(x,z,t=0)$ is zero and also has to stay zero within the domain $(0 < z < H, 0 < x < L)$, because of the constant basic-state PV in combination with PV-conservation

$$q^{'} = \frac{1}{f_0}\frac{\partial^2\phi^{'}}{\partial x^2} + \frac{f_0}{N_0^2}\left(\frac{\partial^2\phi^{'}}{\partial z^2}\right) = 0. \tag{2.87}$$

Using our assumption of a wave-like solution given by equation (2.82), we further end up with a second-order ordinary differential equation for the vertical structure function $\hat{\phi}$

$$\frac{\mathrm{d}^2\hat{\phi}}{\mathrm{d}z^2} - \frac{k^2N_0^2}{f_0^2}\hat{\phi} = 0. \tag{2.88}$$

This then leads to the following solution

$$\hat{\phi} = A(k)\sinh\left(\frac{N_0kz}{f_0}\right) + B(k)\cosh\left(\frac{N_0kz}{f_0}\right), \tag{2.89}$$

where the coefficients A and B can be calculated regarding the given boundary conditions. Following several calculation steps (given for example in [14] p. 178 ff.), we end up with the following dispersion relation:

$$c = \frac{U}{2} \pm \frac{U}{2}\left[1 - 4\left(\frac{f_0}{N_0kH}\right)^2\left\{\frac{N_0kH}{f_0}\coth\left(\frac{N_0kH}{f_0}\right) - 1\right\}\right]^{\frac{1}{2}}. \tag{2.90}$$

By introducing a nondimensional wavenumber s and the Rossby radius of deformation L_R

$$L_R = \frac{N_0H}{f_0};\;\; s = \frac{N_0kH}{2f_0} = k\frac{L_R}{2} \tag{2.91}$$

and considering the Eady growth rate, which is the coefficient multiplying time in the exponent given by (2.83)

$$kc_i = \left(\frac{U}{L_R}\right)[(\coth(s) - s)(s - \tanh(s))]^{\frac{1}{2}} = \frac{U}{H}\frac{f_0}{N_0}[(\coth(s) - s)(s - \tanh(s))]^{\frac{1}{2}}, \tag{2.92}$$

we are finally able to gain a lot of qualitative insight regarding the reasons for instability growth in general.

The growth rate, given in equation (2.92), is proportional to the basic-state shear U/H and inversely proportional to the basic-state static stability $N_0 = \frac{g}{\theta_{00}} \frac{\mathrm{d}\theta_0}{\mathrm{d}z}$. Furthermore, it is also characterized by a latitudinal dependence. To determine the wavenumber of maximum growth rate, we can take $\partial c_i / \partial s$ into account and set the result equal to zero to solve for the maximum

$$kc_{i\,\max} = 0.31 \frac{f_0}{N_0} \frac{U}{H}, \tag{2.93}$$

which corresponds to a maximum nondimensional wavenumber of $s_{max} = 0.8031$. Considering typical synoptic-scale values ($L_R \sim 1000\,\mathrm{km}$) yields a wavelength of maximum growth of $\sim 4.000\,\mathrm{km}$, which corresponds to wavenumber 6 or 7 at $45°N$ latitude.
All factors, given in equation (2.92), can be easily understood in the PV-framework, as we will see subsequently. However, before providing physical analysis of the growth and cut-off wavelengths one might further examine the vertical structure of disturbances.
The growth rate, scaled by the basic-state shear (U/H), is inversely proportional to the basic-state static stability ($g/\theta_{00}\,\mathrm{d}\theta_0/\mathrm{d}z$) and has latitudinal dependence. All of these factors are consistent with observations and with the material discussed in chapter 5. As we will see subsequently, they are easily interpreted in the PV framework. By using the results for A and B

$$B = 1; \;\; A = -\frac{f_0}{N_0 k} \frac{U}{cH}, \tag{2.94}$$

we can analyze the vertical motion by also defining the Rossby depth H_R

$$\hat{\phi}(z) = -\frac{H_R}{H} \frac{U}{c} \sinh\left(\frac{z}{H_R}\right) + \cosh\left(\frac{z}{H_R}\right), \quad H_R \equiv \frac{f_0}{N_0 k}. \tag{2.95}$$

By expressing the hyperbolic functions in the form of exponentials it becomes evident that the Rossby depth H_R is the particular value which gives rise to the vertical length scale of disturbances. Since our model is based on the assumption of vanishing initial PV perturbations in the interior of the domain, the amplitude of the disturbances within this region will depend on the extent to which the boundary PV anomalies reach into the vertical. Intuitively, it is clear that the amplitude of arising disturbances should be proportional to the latitude and should also inversely scale with basic-state static stability and wave number. However, using $v_g' = 1/f_0 \cdot (\partial \phi'/\partial x)$ and $b' = \partial \phi'/\partial z$, we would further be able to compute the disturbance streamfunction, geostrophic and ageostrophic wind, as well as the potential temperature fields.

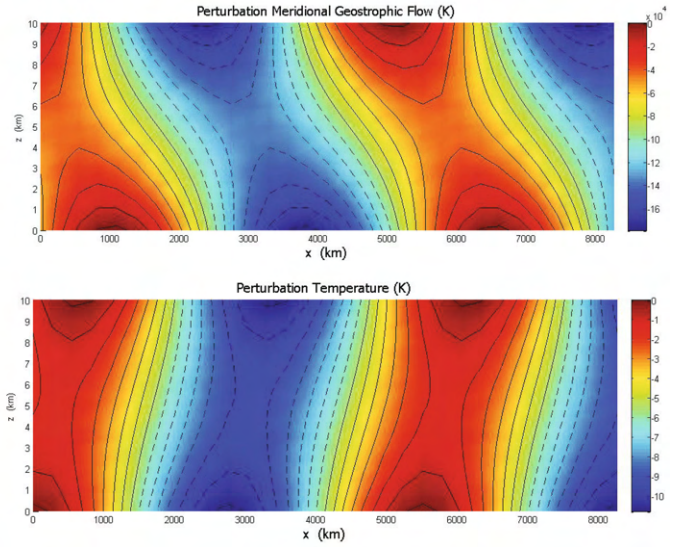

Fig. 10: Perturbation Meridional Geostrophic Flow (top) and Perturbation Temperature (bottom) following the Solutions of the Eady Model [14]

Concerning the disturbance streamfunction vizualized by figure 11, we see that there is a phase shift between the upper and lower disturbances. In section 3.1 we will further investigate this characterisitc and its importance when it comes to the formation of cyclones in the mid-latitudes.

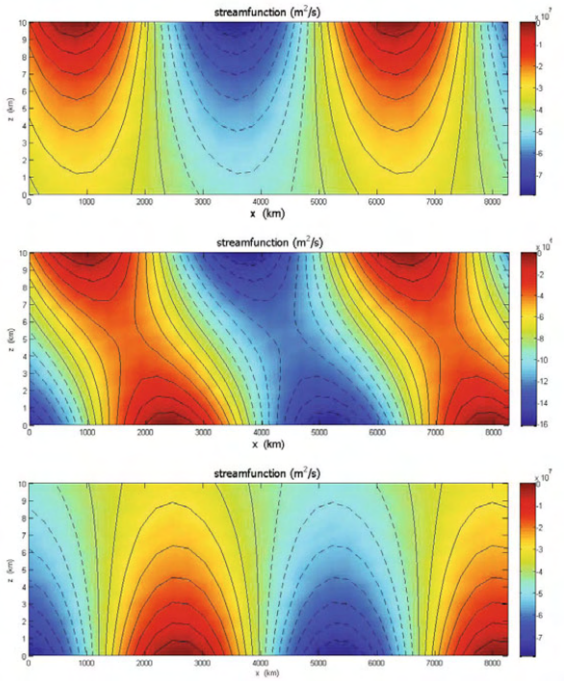

Fig. 11: Visualization of the Perturbation Streamfunction for the Most Unstable Eady Mode [14]
We emphasize the top and bottom disturbance by considering the upper and lower figure respectively. The central graph is representing the full solution.

A comparison of figure 10 (top) and 11 shows that the southerly perturbation geostrophic wind maximises to the east of the trough, whereas the northerly perturbation geostrophic wind maximises to the west of it.
The structure of the disturbance temperature (figure 10 (bottom)) leans in the opposite direction in comparison to that of the geopotential, consistent with warm lower troughs and cold upper troughs [14].
As will be described in section 3.1, the phase speed of a developing trough at the level of the tropopause is typically slower than the mean flow, while the associated warm anomaly in the lower boundary is characterized by a faster propagation speed in comparison to the mean flow. Given a situation in which the upper wave is faster than the lower one, northerly cold potential temperature advection would act in order to slow the phase speed of the upper wave, while the southerly warm advection on the lower boundary associated with the upper wave will increase the eastward movement of the latter. The probability for such a successful *Phase Locking* process can be interpreted by regarding the Rossby depth H_R, which gives rise to the vertical extent of the boundary-based disturbance amplitude. An environment characterized by a large static stability is also described by small Rossby depth as explained earlier. Hence, the disturbances will not be able to phase lock in this case. The normalized wavenumber s is related to the Rossby depth by

$$s = \frac{N_0 k H}{f_0} = \frac{H}{H_R}. \tag{2.96}$$

Therefore, disturbances associated with a small wavelength are denoted by smaller vertical penetration into the interior of the domain, hence, leading to a smaller probability for the associated waves to phase lock.

When the vertical extent of the boundary circulations falls below some critical fraction of the depth of the troposphere, the disturbances no longer interact and mutually amplify. Additionally, the wave number of the given perturbations also affects their phase speed as a result of the dispersion relation given by equation (2.90), therefore also contributing to the realization of the phase locking process. If the necessary pre-conditions are met, the upper and lower disturbances would travel at the same speed while facilitating phase locking and growth of themselves.
However, one might also mention the existence of a long-wave cutoff which describes the scenario in which the wavelength becomes large enough, such that the upper and lower disturbances would move apart as a result of the propagation effect.
By investigating the latter sections one should have gained a severe understanding of the basic effects dominating and leading to most of the driving processes in atmospheric dynamics. Emphasizing the knowledge we gained concerning quasi-geostrophic theory, basic concepts describing vertical air motion, the insights we achieved using the PV-framework and understanding of the fundamentals of frontogenesis and baroclinic instability growth, we are now able to further investigate the leading differences in extratropical and tropical cyclones. The comparison of these two mature hazards, affecting the state of our daily weather, will be subject of the next section in order to build a bridge between the theoretical background and its application when analyzing certain storms and weather systems in particular. This in the end will give us the building blocks to dig deeper into the topic of tropical cyclogenesis and further investigation of the processes involved.

3 Cyclones in the Earth's Atmosphere

Following the argumentation given in the preceding chapters, one might infer several frameworks with which one is able to describe the evolution and development of various types of synoptic weather systems. Consideration of the quasi-geostrophic perspective gives rise to the importance of ageostrophic air motions associated with a secondary circulation that arises in response to the disruption of thermal wind balance by the primary geostrophic flow. The quasi-geostrophic height tendency equation, which can be interpreted as a statement for potential vorticity conservation, demonstrates the leading effects connected to the development or decay of weather systems.
In this section we will apply the QG framework as well as the isentropic analysis and PV consideration presented in section 2.3 and 2.4, in order to understand the meteorological aspects in the vicinity of extratropical and tropical cyclones.

3.1 Extratropical Cyclogenesis

3.1.1 General Understanding

As we have seen in section 2, cyclonic vorticity maxima are one of the main drivers leading to the development of several different atmospheric disturbances like tropical and extratropical cyclones, upper troughs, frontal systems, lee troughs, and jet streaks for example. Hence, if one is interested in describing the processes interrelated with cyclogenesis, the vorticity equation given by (2.18) serves as a good starting point. Cyclones are generally observed to frequently form along preexisting frontal boundaries because of the enhanced cyclonic vorticity associated with them.

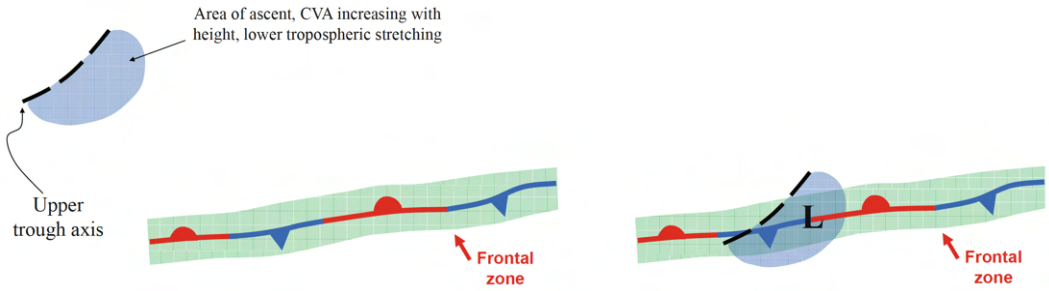

Fig. 12: Sketch of an Upper-Trough reaching a Stationary Weather Front [14]
The preexisting region of enhanced relative cyclonic vorticity associated with the front leads to the development of a surface low (L) after frontal-upper trough contact.

In order to gain a simple understanding of cyclogenesis we will firstly restrict the consideration on to the vorticity change near the surface in the vicinity of a uniform frontal boundary, as demonstrated in figure 12. Since it is reasonable to neglect the advection and tilting term near the surface, the stretching term in (2.18) ($\zeta_a(\partial\omega/\partial p)$) remains and serves as the main driver concerning vorticity production. Describing the general situation in which an upper-tropospheric trough tracks toward the described boundary, we would expect forcing for ascent resulting in lower-tropospheric stretching ahead of the trough axis. In this very situation, a low pressure system will typically not form until the upper-trough axis has reached the front, which can be understood by analyzing the stretching term itself. By investigating the latter we see a direct proportionality to the relative vorticity. Hence, a given amount of upward vertical motion is more effective in enhancing the absolute vorticity in areas, where the vorticity is already large. This feedback mechanism can also be understood by solving the frictionless vorticity equation for a point, moving with the surface cyclonic vorticity center, while restricting ourselves to the stretching term only

$$\frac{\mathrm{d}\zeta_a}{\mathrm{d}t} = -\zeta_a(\nabla\cdot\vec{V}); \quad \frac{\mathrm{d}(\ln(\zeta_a))}{\mathrm{d}t} = -(\nabla\cdot\vec{V}). \tag{3.1}$$

Further consideration of the antilog on each side and integrating to obtain an expression for the vorticity as a function of time, leads to

$$\zeta_a(t) = \zeta_a(0)\exp(-(\nabla \cdot \vec{V})t). \tag{3.2}$$

Equation (3.2) describes the fact that a constant value of convergence will lead to an exponential growth of vorticity with time, proportional to the initial absolute vorticity at the point of evaluation. While friction will naturally limit the growth rate in the lower troposphere, the value of convergence will also tend to increase with the intensity of the storm system as well, which affects the temporal realization of the spin-down. Therefore, strongly developing storm systems can exhibit exponential vorticity growth over a long time, which characterizes the most dominant reason for extratropical cyclone formation.

3.1.2 Description from a Potential Vorticity Standpoint

As described in section 2.6, the flow associated with a given PV anomaly is inversely proportional to the static stability. Hence, a PV anomaly present in unstable environments will extend a greater distance into the vertical, relative to the scenario given in stable atmospheric situations. Further already inferred factors concerning the peculiarity of PV anomalies are the horizontal scale of the anomaly itself, as well as the disturbance amplitude. Given that the highly stable stratosphere is the primary source region of cyclonic PV for upper-tropospheric disturbances, observations reveal the presence of preexisting upper-tropospheric cyclonic PV anomalies for the majority of extratropical cyclogenesis events [17]. One advantageous precondition concerning the formation of upper-level PV anomalies is the existence of an upper-level frontal zone. Upper-level frontal systems leading to vertical air motion, as described in section 2.5, can force stratospheric air to descend or even result in the deformation of the dynamic tropopause itself.
The most common description of mid-latitude cyclones in the PV-framework is based upon four anomalies demonstrated in figure 13

1. The stratospheric upper-level PV maximum
2. A diabatically produced cyclonic lower-tropospheric PV anomaly
3. A surface-based warm potential temperature anomaly
4. A diabatically produced anticyclonic upper-level PV anomaly

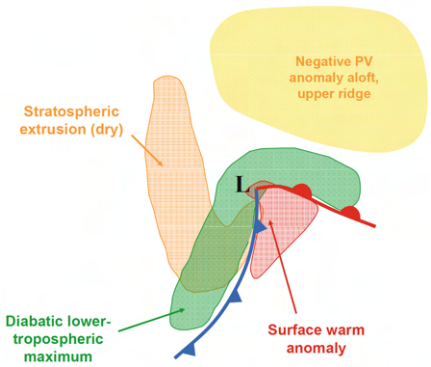

Fig. 13: PV Anomalies leading to the Formation of an Extratropical Cyclone [14] - adapted from [18]

The extratropical cyclogenesis process can be seen as an interaction between these anomalies in order to constructively interfere. The building blocks leading to a growth of PV anomalies can differ in several ways, which is why we restrict ourselves to the ones most important for cyclogenesis, which are mutual amplification and diabatic growth [19].
Regarding figure 14, we can emphasize the existence of an upper-level cyclonic PV maximum, visualized as a cold anomaly of potential temperature at the level of the dynamic tropopause. The blue arrows denote the direction of the cyclonic circulation. If the necessary preconditions are satisfied (significant trough amplitude and scale, as well as a relatively low static stability of the environmental air, as described in section 2.6), the cyclonic circulation associated with the upper trough will extend towards the surface. In a situation, in which a meridional temperature gradient is present, as would be found in the vicinity of the jet stream for example, the resulting southerly flow at the surface would lead to the development of a lower-level warm potential temperature anomaly by advection. In cases, where a surface warm anomaly is already present, the

flow associated with the upper-level trough could lead to further amplification of the anomaly itself. On the other hand, a surface warm anomaly is characterized by a cyclonic circulation, as is visualized by the red vectors. Hence, this could also lead to cold potential temperature advection in the center of the upper-level trough and further amplification of the already existing cyclonic anomaly, if the necessary preconditions are met. If the essential environmental conditions are fulfilled, the disturbances will amplify each other in a process that has been described as the "essence" of baroclinic instability by Hoskins [20].

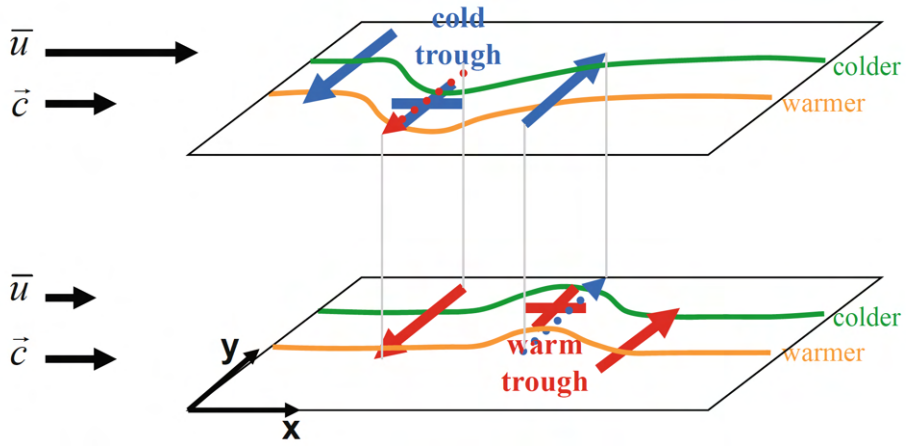

Fig. 14: Reciprocal Amplification of Tropopause-Level and Surface Potential Temperature Anomalies [20]

Hence potential temperature anomalies are equivalent to cyclonic PV anomalies the plus signs on each level denote the cyclonic PV anomaly center. The associated circulations are visualized by the arrows where as the arrows on the left characterize the mean flow and phase wave speed respectively.

As already emphasized in section 2.6, the propagation direction of the upper-level disturbance is towards the west, in comparison to the background basic-state flow. Due to the cyclonic circulation, the cold potential temperature advection to the west side of the trough serves in order to reinforce the cyclonic sign of potential temperature, which leads to a phase speed of the trough considerably slower than the velocity of the mean basic-state flow. In the same way, we are able to understand that the warm advection to the east of the trough leads to a faster phase velocity in comparison to the background flow, regarding the lower tropospheric boundary. Visualized by the bold arrows, we can infer that the mean westerly wind at upper levels in a baroclinic flow is stronger than that near the surface, leading to a critical counter-propagation effect already intimated in section 2.6. Propagation at similar speeds extends the duration of mutual amplification and constructive advection, therefore leading to more intensive storm systems. *Phase locking*, a process we already inferred in section 2.6 as well, describes the realization of individual changes in phase speed due to cross advections, which also leads to enhanced mutual amplification.
Additionally, the analysis of several piecewise PV inversion studies demonstrates, that the diabatic PV feature can contribute up to 50% of the surface cyclonic circulation. Hence, the propagation effects of the diabatic PV anomaly can affect the ability of upper and lower PV anomalies to phase lock [19].

3.2 Tropical Cyclones - Characterisitics and Development

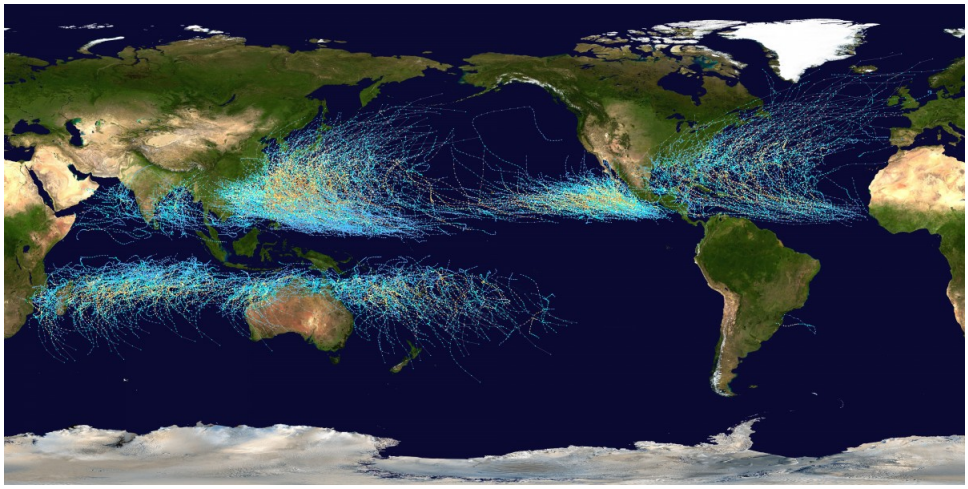

Fig. 15: Visualization of all Tropical Cyclone Tracks between 1985 and 2005 [21]
Colors denoting the associated level on the Saffir-Simpson Hurricane Scale with bright yellow ones depicting stage 1 *and red members characterizing stage* 5 *hurricanes.*
Cyan colored tracks visualize tropical storms.

Following the definition of the National Oceanic and Atmospheric Administration of the USA, a tropical cyclone is a generic term for a low-pressure system that formed over tropical waters (25° S to 25° N) with thunderstorm activity near the center of its closed cyclonic winds. The main driver of tropical cyclones is characterised by the "extraction" of energy from the vertical temperature gradient. Consequently, they convert potential energy into kinetic energy, are described by a symmetric shape and posses the structure of a warm core system [22]. Hence, in comparison to the content of section 3.1, mechanisms through which tropical cyclogenesis occurs, are distinctly different from those through which temperate cyclogenesis occurs. There are several factors which favor the formation of a tropical storm:

1. High sea surface temperatures with values greater than 26.5° C within the upper 70 m of the ocean.
2. Presence of the Coriolis force strong enough to create a cyclonic vortex
3. Small variations in the vertical wind speed
4. Sufficient amount of moisture in the Mid-Troposphere in order to drive the vortex
5. A preexisting weak low-pressure area or lower-level cyclonic circulation
6. Upper divergence above the sea level system

Regarding figure 15, one might recognize that tropical cyclones form mostly on the western margins of the oceans. The depth of the warmer waters should be characterized by a minimum of $60\,\mathrm{m} - 70\,\mathrm{m}$ in order to neglect the mixing of cooler waters below, resulting from deep convection currents in the ocean. This condition restricts our analysis to the western tropical oceans, because of the warm ocean currents flowing from east to west, while forming a thick layer of water associated with temperatures greater than 27° C near the surface and providing the necessary amount of moisture in order to drive the cyclone. Because of the existence of cold ocean currents in the eastern parts of the tropical oceans, tropical cyclogenesis is rarely observed in those regions.
Tropical cyclones occur mostly in the late summer months. This is partly due to the specific heat of water, which results in a maximum of ocean temperatures in the northern hemisphere,

generally attained in the middle of August. On the other hand, this is also due to the enhanced whirling motion in the atmosphere, which is commonly observed when the doldrums over the oceans are most far away from the equator, coinciding with the time from August to September. Since the Coriolis force is needed in order to realize the development of a vortex-structure, we are generally not able to find tropical cyclones at the equator. However, about 65% of cyclonic activity occurs between 10° and 20° latitude.
Another important factor is demonstrated by the necessary existence of lower-level disturbances in the form of easterly waves, forming in the Inter-Tropical Convergence Zone (ITCZ) in order to serve as seeds for tropical cyclogenesis. Several low pressure systems are produced by the abundance of small local differences in the temperature of water and air, which leads to a weak cyclonic circulation around each of those areas. Hence, rising air motion associated with the existence of warm humid air in the environment enhances the probability for strong cyclonic vortex development.
One of the most important restrictions for tropical cyclogenesis is the impact of vertical wind shear. There is increased understanding of how vertical wind shear affects genesis, particularly the sensitivity in different environments. The alignment of the lower- and mid-level vortices is associated with genesis and subsequent intensification [23]. "Unsuccessful" cyclogenesis in high shear environments occurs, when heat is advected farther away from the lower-level center, leading to a reduced secondary circulation strength and weakening vortex precession. However, tropical cyclones at higher latitudes [24] and at higher sea surface temperatures [23] are able to better resist vertical wind shear presence.
Additionally high humidity $(50-60)\%$ is required in the mid-troposphere, in order to increase the probability of cumulonimbus cloud formation. Furthermore, well-developed divergence in the upper layers of the atmosphere is important as well, such that the low pressure area at the center of the cyclone can be maintained.
In general, one could summarize the formation of tropical cyclones as follows.
Given a situation, in which multiple thunderstorms originate over the oceans, a merger of those storms will result in the formation of an intense low pressure system near the surface. Since the existence of thunderstorms is associated with vertical air motion, condensation of water vapor occurs at a certain height derivable by the dry and adiabatic lapse rate respectively. Condensation then leads to latent heat release and further uplifting. The lower troposphere is constantly refilled by fresh moisture laden air demonstrating a cycle, which is repeated as long as the moisture can be supplied. Further intensification of the storm occurs due to the excess moisture over the oceans, leading to higher wind speeds near the surface. Additionally, the wind field undergoes deflection due to the Coriolis force, leading to the formation of a cyclonic vortex, which will weaken significantly in intensity, whenever the supply of moisture is cut off. Understanding the latter demonstrates why tropical cyclones dissipate really fast when reaching land masses and undergoing land fall.
There are much more aspects which affect tropical cyclogenesis as well. For example dynamic-thermodynamic interactions, the role of cloud-microphysics, the existence of radiative-convective equilibrium and radiative feedback, etc.
However, since this work aims towards a better understanding of the PV development associated with the *Transition* of weather systems, leading to the evolution of tropical cyclones, we will further lay an important focus on this transition process itself.

3.3 Differences of Extratropical and Tropical Cyclones in the PV-framework

The Knowledge of the physical processes responsible for the observed PV distribution and its development provides information about the formation and evolution of given weather systems. Hence, we are able to infer the contrasting characteristics in the PV structures accompanying different cyclone types, as shown in figure 16.

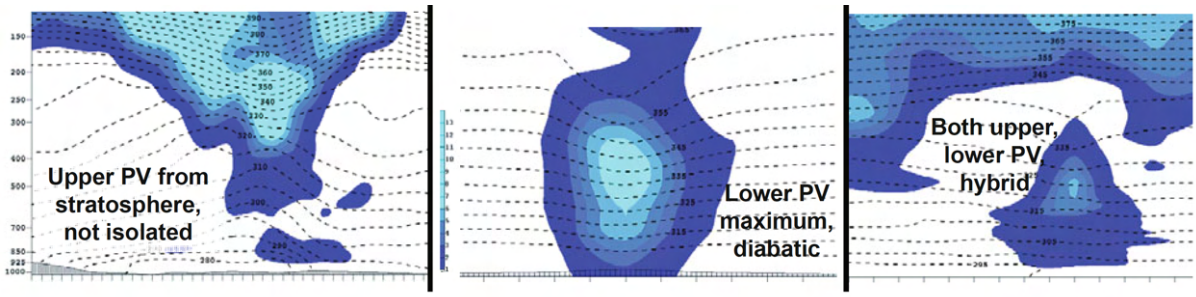

Fig. 16: PV Visualization on Dashed Isentropic Levels (Shaded Above $1PVU$ with Shade Interval of also $1PVU$) for Three Different Exemplary Situations [14]
A wintertime extratropical cyclone (left) in the year 2000, PV structure of Hurricane Katrina on 0000 UTC 29 August 2005 (middle) and a hybrid subtropical cyclone in 2008 (right)

An extratropical cyclone (figure 16 (a)) is characterized by the fact that the main cyclonic PV feature is of stratospheric origin, with some contributions of diabatic processes in the lower troposphere. Furthermore, it is represented by an asymmetric shape and a cold core structure, which describes the fact that the isentropes are squeezed towards the cyclone center.
However, for tropical cyclones, the diabatic PV tower is the dominant feature, consistent with a warm-core structure, depicting the stretching of isentropes in the center region and the absence of stratospheric influence. This PV tower structure is the natural result of the latent heat release due to the condensation of water vapor, associated with the formation of cumulonimbus clouds. Naturally, combinations of both types of storm systems are also possible and realized in nature. Hybrid systems, characterized by strong PV maxima of both, stratospheric and diabatic origin, cover a wide range of weather phenomena, such as recurving tropical cyclones, extratropical cyclones accompanied by heavy precipitation or also the transition phase between an extratropical and a tropical cyclone further investigated in this study.

4 The Tropical Transition Process - Data and Methods

Until the 1950s, there was a clear general conviction that tropical cyclones had a life cycle (formation, development, maturity and decay), that was distinct from extratropical cyclones. As described in [25], tropical cyclones form over warm water, intensify from wind-driven evaporation and the resulting latent heat release, while decaying over colder water or land. Several studies also analyzed the natural structure of extratropical cyclones. Those storms, which form in the mid-latitudes, mainly as a consequence of temperature gradients, vertical wind shear and PV anomalies, are characterized by a comparably high asymmetry and decay due to the removal of the instability associated with an occlusion process ([26], [27], [28]). However, there was little knowledge about the mixture forms of both types, which is primarily due to the lack of high-resolution satellite observations.
From 2000 to 2003, nearly half of the Atlantic tropical cyclones formed due to the existence of an extratropical precursor [8]. This development, characterized by the transition of a cold- into a warm-core system and its importance for the understanding of weather dynamics and forecast, was therefore defined as *Tropical Transition* (TT). In order to understand the reasons for particular TT events, one might investigate the wide variety of precursor anomalies, with anticyclonic wave breaking describing the most dominant type ([29], [30]). Penetration of an upper-level precursor potential vorticity (PV) trough into the (sub)tropics might lead to the development of an antecedent extratropical or subtropical cyclone [1]. One special characteristic, which differs in the description of TT and other cyclogenesis pathways, is marked by the interplay between the upper-tropospheric PV trough and a lower-level baroclinic zone, which further facilitates the organization of convection [2]. This convection then eventually diminishes the PV gradients above the cyclone center, which leads to a reduction in vertical shear, as can be inferred by regarding equation (2.64), and results in a transformation of the environment further favoring tropical cyclogenesis (see section 3).
Tropical Transition processes account for approximately 16% of all tropical cyclone formations around the globe [3]. Depending on the strength of the initial lower level circulation, these events can be divided into two main groups [3]. *Weak TT Events* are characterized by a weak extratropical cyclone precursor, where near-surface winds are not strong enough to enhance surface fluxes sufficiently to sustain the vortex [31]. *Strong TT Events*, on the other hand, can be identified by near-surface winds, which are capable to trigger wind-induced surface heat exchange sufficiently to promote the growth of a self-sustaining circulation [9].

4.1 Cyclone-Phase-Space Diagrams

In order to ensure a proper analysis of the processes involved during TT, the most relevant differences between the two cyclone structures must first be understood. Hence, using an appropriate phase space which entails the strength of the warm-core and cold-core structure respectively, as well as describing the stage of extratropical development, demonstrates a legitimate starting point [32]. In the following, the same three parameters will be used as described in [32], to further facilitate the investigation of case study examples demonstrated by Hurricane Leslie and Paulette.
Because of the high asymmetry of extratropical cyclones resulting from the existence of large vertical wind shear in comparison to the symmetric properties of tropical cyclones, a measure of horizontal temperature gradients will be used to identify the frontal structure of the described system. This frontal nature is defined as the storm-motion-relative $900\,\mathrm{hPa} - 600\,\mathrm{hPa}$ thickness asymmetry across the cyclone within 500 km radius

$$B = h(\overline{Z_{700\,\mathrm{hPa}} - Z_{925\,\mathrm{hPa}}}|_R - \overline{Z_{700\,\mathrm{hPa}} - Z_{925\,\mathrm{hPa}}}|_L). \tag{4.1}$$

Here, Z denotes the isobaric height, R indicates the right side of the current storm motion, L describes the left side of storm motion, h characterizes the considered hemisphere ($+1$ for Northern Hemisphere, -1 for Southern Hemisphere) and the overbar indicates the areal mean

over a semicircle of radius 500 km. Originally, the denoted pressure range, mentioned by Hart et al. (2003) ((900 − 600) hPa and (600 − 300) hPa) is chosen to assure the neglect of boundary-layer-based disturbances. However, Picornell et al. [33] suggested choosing the (925 − 700) hPa and (700 − 400) hPa pressure range instead, because of their more enhanced suitability for higher latitudes connected with lower tropopause heights. Since no major hurricane had associated with it a value of B that exceeded 10 m [34], a legitimate threshold for distinguishing a tropical from a nontropical thermal gradient is $B = 10\,\mathrm{m}$.
Furthermore, the thermal structure of a considered system can be described by the isobaric height gradient and geostrophic wind magnitude, which is why one might use this to differentiate between a cold-core (geostrophic wind magnitude increases above the cyclone center) and warm-core (geostrophic wind magnitude decreases above the cyclone center) system. The cyclone height perturbation ($\Delta Z = Z_{Max} - Z_{Min}$) evaluated within the respective radius of 500 km is used to calculate the scaled thermal wind V_T^L and V_T^U respectively

$$\begin{aligned} \frac{\partial(\Delta Z)}{\partial(\ln(p))}\bigg|_{925\,\mathrm{hPa}}^{700\,\mathrm{hPa}} &= -\left|V_T^L\right| \\ \frac{\partial(\Delta Z)}{\partial(\ln(p))}\bigg|_{700\,\mathrm{hPa}}^{400\,\mathrm{hPa}} &= -\left|V_T^U\right|. \end{aligned} \tag{4.2}$$

Analysis of the equations (4.2) and the associated vertical structure of the geopotential height perturbation further culminates in the description of the system as cold- or warm-core. As already investigated in section 3.3, a cold-core structure is characterised by a larger perturbation of geopotential heights at the top of the respective layer, whereas it is the other way round when describing the characteristics in the vertical structure of warm-core systems.
In order to facilitate the analysis of phase transitions within the life cycle of the considered storms, a 24 h moving average is applied in further investigations to obtain smoother trajectories, as was also done by Hart et al. [32].

4.2 The Coupling Index as a Measure for Bulk Convective Stability

The scientific analysis of Mauk and Hobgood [35], published in 2012, sheds light on to the necessary preconditions needed for realizing tropical cyclogenesis over the comparatively cooler waters of the North Atlantic Ocean. Because of the baroclinic environment in which the precursor features are embedded, Mauk and Hobgood state, that the majority of *Low-SST* formations can be classified as strong tropical transitions. As mentioned above, a study by McTaggart-Cowan et al. [3] from 2013 shows, that 16% of all tropical cyclones arise from baroclinic precursors, while developing into a warm-core system in association with the redistribution of mass and momentum [35]. McTaggart-Cowan et al. [9] (2015) goes even further by suggesting to consider the evolution of a different parameter instead of the common used sea surface temperature threshold of 26.5° C, when it comes to the understanding of tropical cyclogenesis events in a baroclinic environment. The *Coupling Index* (CI), which is calculated as the difference between the potential temperature on the dynamic tropopause (2 PVU-Isosurface) and the equivalent potential temperature at a level of 850 hPa, links the upper and lower levels, while demonstrating a measure for tropospheric depth and bulk convective stability [9]. A cold air mass aloft, described by large values of cyclonic PV, therefore representing an intrusion of stratospheric air for example (see section 2.4), reduces the bulk tropospheric stability. Following our understanding, presented in section 2.6, this then leads to an increased Rossby penetration depth, which in turn promotes vertical connections between the upper- and lower perturbations. Hence, resulting in a significantly stronger secondary circulation and enhanced vertical motions downshear of the anomaly [36]. It is this reduction in bulk convective stability, which led McTaggart-Cowan et al. [9] to the result of using a CI-threshold of 22.5° C, instead of utilizing the common SST-threshold of 26.5° C when it comes to the description of tropical cyclogenesis associated with TT events.
In further sections, the CI development in the case of Hurricane Leslie and Paulette will be

further investigated in order to differentiate between the necessary preconditions concerning the environmental characteristics connected with those two storms. In this context, we will also try to shed light on to the importance of regarding the CI development in comparison to the evolution of the PV structures, which leads to, or counteracts the realization of Tropical Transition scenarios.

4.3 Tracking and Group Partitioning

4.3.1 Cyclone Tracking and Dynamic Time Warping

In order to get an overview about the storm systems of both case study examples, the next section provides an investigation of the synoptic development at first. Hereby, calculations are based on *ECMWF Reanalysis - ERA5*. As presented in section 6, temperature, relative humidity and horizontal velocity data on the $50, 100, 200, 250, 300, 400, 500, 700, 850$ and $925\,\mathrm{hPa}$ isobars are applied. To further investigate the ensemble weather predictions in later sections, the perturbed ensemble weather forecast of the ECMWF is applied.
When using ensemble weather prediction forecast in order to analyze the behavior of extratropical and tropical cyclones, one firstly has to track the specific storm in an ordinary way. Since this serves as the base for further investigations, the computations implied in this study are based on the cyclone tracking algorithm by Hodges et al. [37]. In this case, the 6-hourly relative vorticity on the $850\,\mathrm{hPa}$ and $700\,\mathrm{hPa}$ isobars is applied. Serra et al. [38] showed that more coherent tracks can be produced by using the vertical average of $850\,\mathrm{hPa}$- to $600\,\mathrm{hPa}$ relative vorticity. However, since relative vorticity on the level of $600\,\mathrm{hPa}$ is not available in the ECMWF database, we restricted ourselves to the two levels mentioned above, which also already shows a sufficient improvement. A further initial identification is performed by applying a vorticity threshold of $5 \cdot 10^{-6}\,\mathrm{s}^{-1}$. Additionally, the maximum $10\,\mathrm{m}$ wind speed and minimum pressure are added to the forecast tracks in order to serve for verification against the IBTrACS data. To analyze the correct position, the nearest mean sea level pressure minima within a $5°$ radius and the wind speeds in a vicinity of $6°$ from the vorticity center are considered. Further restrictions, inferable by considering the work of Hodges et al. [37], can be found in the cited literature.
Applying this tracking algorithm to the analysis track of the operational weather forecast leads to the *Analysis Track*, which will further be used as a reference to the reanalysis data. To investigate rather the tracked cyclone of a particular ensemble member would match to the analysis track, we will further use a dynamic time warping technique adapted to the work of Di Muzio et al. [39]. Limiting ourselves to the calculation of spatial distances might result in matched storm tracks characterized by an accurate prediction in space but slight deviation in time, due to the lag in precursor PV dynamics for example [1]. The main task, when it comes to the application of this technique, is the computation of the so-called *Shortest Warp Path* d_{DTW} [1]. In order to match the analysis track, an ensemble forecast track is required to start and end not earlier or later than $12\,\mathrm{h}$ compared to the analysis track. Furthermore, concerning spatial distances, a forecast track is considered to match with the analysis track, whenever the spatio-temporal average of the shortest warping path $\overline{d_{DTW}}$ does not exceed $700\,\mathrm{km}$.

4.3.2 Cyclone and Transition Group Members in the Ensemble Weather Forecast

While applying the tracking algorithm introduced in the preceding section, we firstly divide every ensemble weather forecast into a *Cyclone* and *No-Cyclone* group respectively. This is done in order to shed light on to the contrasting PV dynamics leading for or against a fulfilled tropical transition scenario. Rather an ensemble member belongs to the first or second group depends on the tracking algorithm and the difference between the analysis and forecast track used in the dynamic time warping technique. Hence, a particular forecast member is added to the *Cyclone* group whenever it predicts a matched or similar track.
However, before analyzing the ensemble weather forecast, it is important to gain a basic understanding of the most relevant features, leading to the real tropical transition events we could

witness and measure in association with the two given storm systems we have chosen. Therefore, we will start our case study analysis by firstly investigate the synoptic evolution and thermostructural development given by the reanalysis data.
While the separation into *Cyclone* and *No-Cyclone* group ensures the selection of only those members associated with the formation of a cyclone sufficiently similar to the analysis track, we now divide the cyclone group even further. The additional division into *Transition* and *No-Transition* group is done in order to separate the spatio-temporal matched cyclone members with respect to the realization of a significantly clear tropical transition scenario. As it was already done in [1], we divide the members of the cyclone group by investigating the maximum of the $-V_T^U$ value, concerning the time domain between 0000 UTC 26 September 2018 to 0000 UTC 29 September 2018 and 0000 UTC 18 September 2020 to 0000 UTC 21 September 2020 regarding the Leslie and Paulette case respectively. This ensures a division into groups, where some members roughly complete a shallow warm seclusion [40], whereas other TTs are characterized by the formation of a tropical storm associated with a widespread deep convection [1]. The ± 12 h window used by applying the dynamic time warping technique is respected. A separation into *Colder*-core, *Intermediate*-core and *Warmer*-core group can be inferred by considering the results presented in section 5.1.1.2. Here, a particular member is added to the colder-core group whenever the maximum value of $-V_T^U$ does not exceed a value of -25. However, it is added to the warmer-core group, if the maximum of $-V_T^U$ is characterized by a value larger than 0 and attached to the intermediate-core group, when acquiring values between those two criteria. This separation, firstly visualized in section 5.1.1.2, represents a sufficient technique in order to differentiate between the particular cases. This can further be inferred by concerning the Coupling Index development of each ensemble member also presented in section 5.1.1.2 and 5.1.2.2.

5 A Twofold Case Study Analysis

This section provides a rather detailed description of the development of the considered storm systems of Leslie and Paulette. It it used in order to examine the environmental conditions leading to the respective TT scenarios. By investigating the PV dynamics in the upper and lower troposphere, we will infer reasons resulting in the measured storm tracks and development pathways associated with the baroclinic character of the environment in which the storms where embedded.

5.1 Investigation of Reanalysis and Ensemble Tracks

5.1.1 Hurricane Leslie

5.1.1.1 Synoptic Development

The main reason for the realization of the pre-Leslie extratropical low pressure region is based on the later development stages of another high intensity storm system. The advection of PV remnants associated with Hurricane *Florence* leads to the formation of a frontal boundary. Following the evolution of an extratropical low on September 22, 2018, anticyclonic wave breaking firstly results in the loss of the cyclone's frontal features near $34° \text{ N}, 48° \text{ W}$ (as demonstrated in figure 17), visualizing the transition of the system into a subtropical storm.

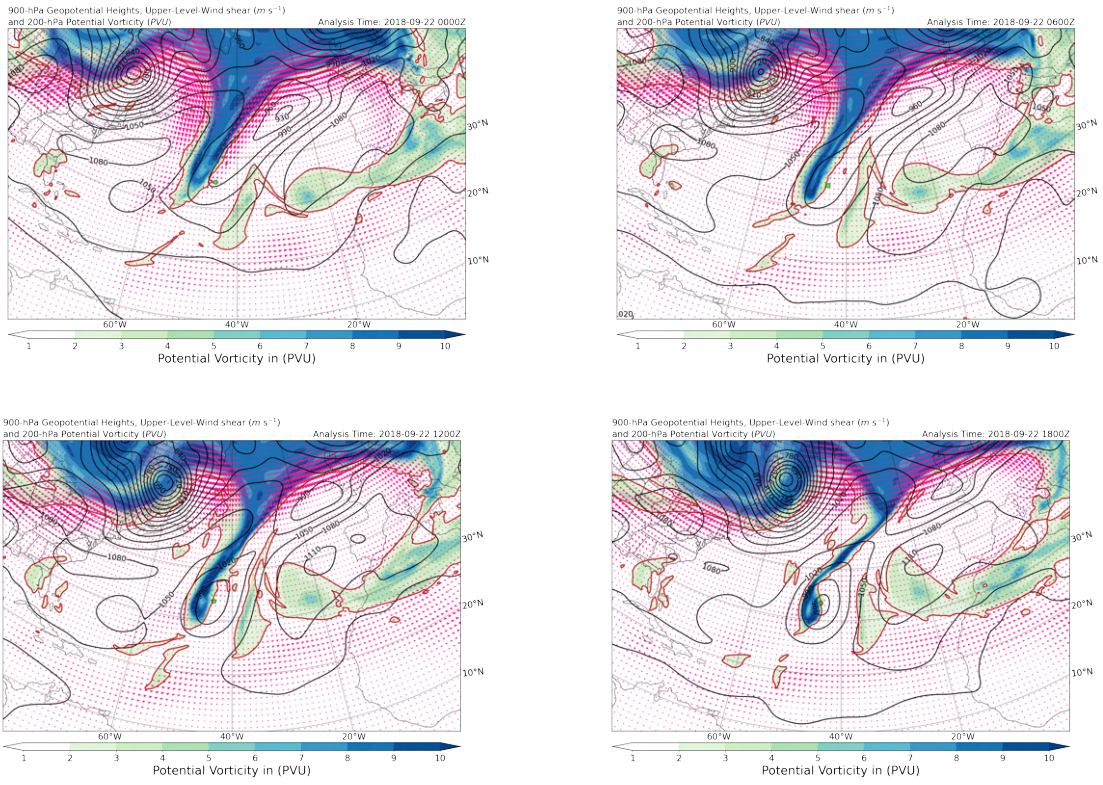

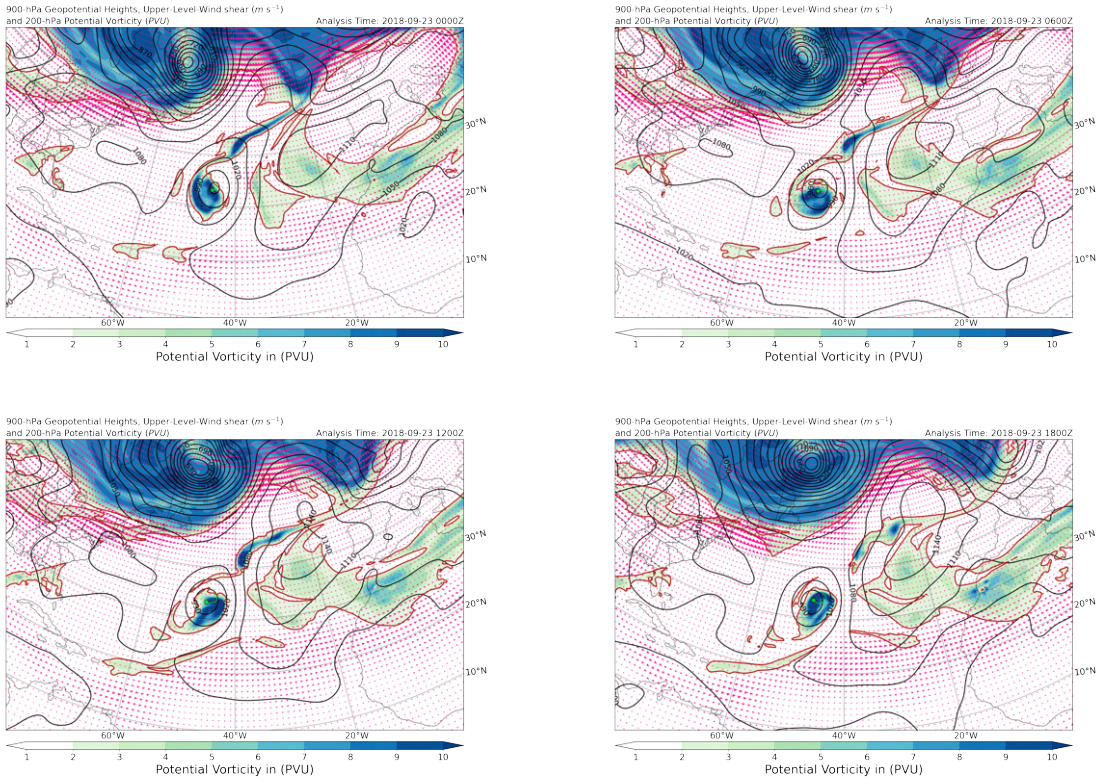

Fig. 17: Upper-Level (200 hPa) PV Development during Subtropical Storm Evolution associated with the Life Cycle of Leslie between 0000 UTC 22 September and 1800 UTC 23 September. *Colorbars highlight the PV in PVU while red arrows denote the intensity of upper-level wind shear. The latter is calculated by taking the difference of the* 200 hPa *and* 500 hPa *horizontal wind velocity. Black lines characterize geopotential values at* 900 hPa *indicated by the numbers labeled to them.*

Due to the embedment in an environment of weak steering currents and vertical shear, together with an input of relatively dry air, the system weakens to a subtropical depression, while following an existing PV feature to the east.
Around 1800 UTC 25 September, Leslie starts to move counterclockwise, while merging with another frontal zone and acquiring extratropical storm status again (figure 18). Since the trough associated with this interaction marks the starting point for the TT process in the Leslie case, we will use 0000 UTC 25 as an initial time for further ensemble analysis.

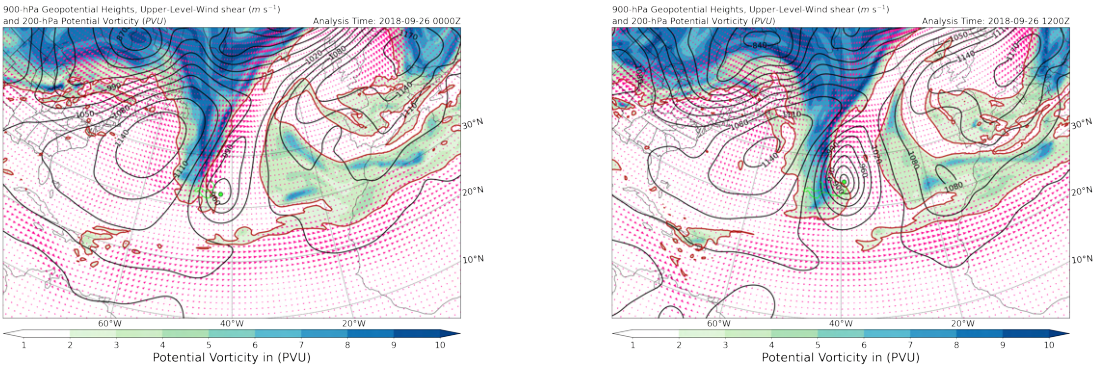

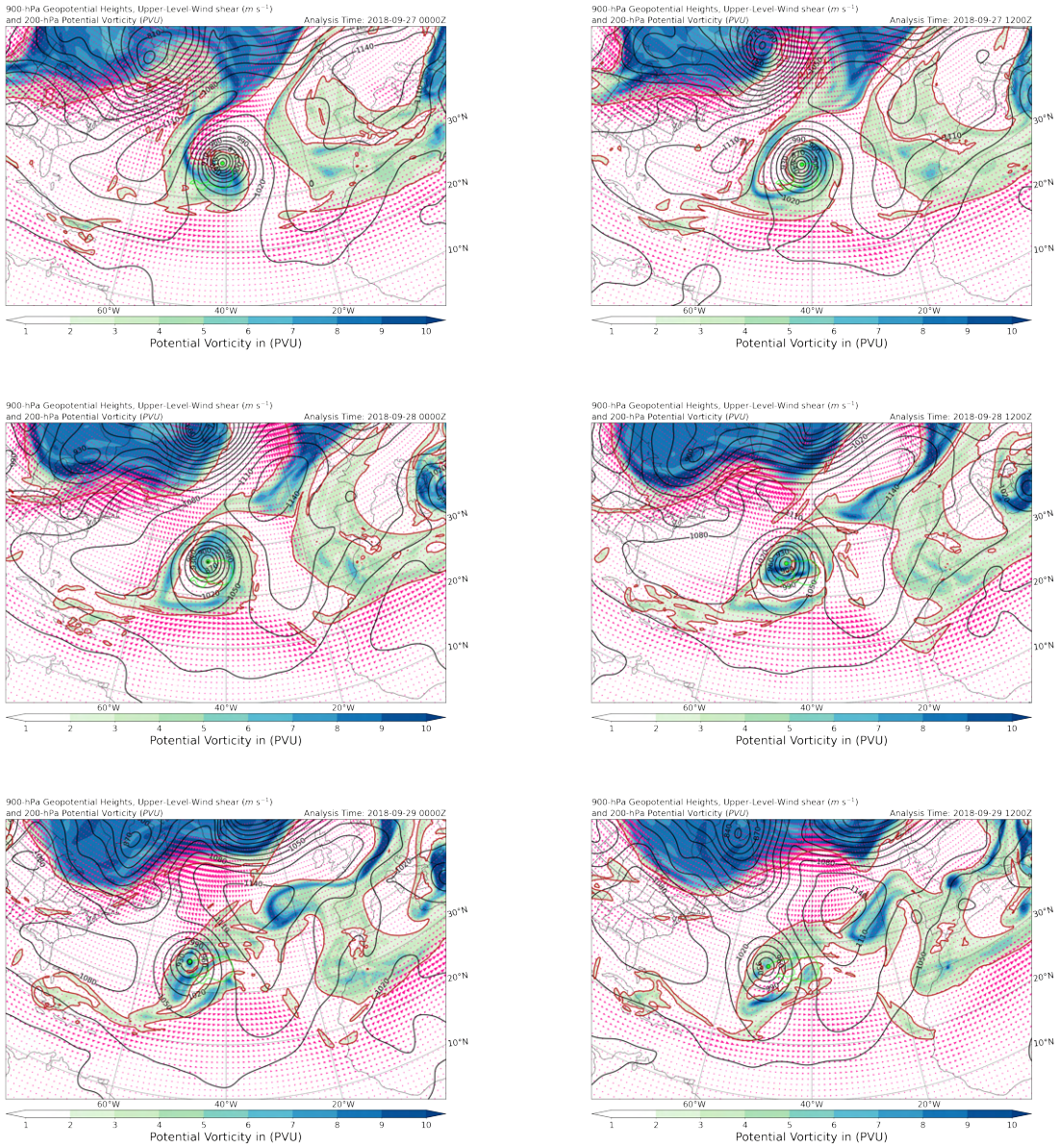

Fig. 18: Upper-Level (200 hPa) PV Development during Subtropical Storm Evolution associated with the Life Cycle of Leslie between 0000 UTC 26 September and 1200 UTC 29 September. *Colorbars highlight the PV in PVU while red arrows denote the intensity of upper-level wind shear. Black lines characterize geopotential values at* 900 hPa *indicated by the numbers labeled to them.*

The cyclonic roll-up of the upper-level PV streamer is associated with the development of a surface low, characterized by a large frontal structure visualized by figure 19. Continuing its movement along the western side of a deep-layer cyclonic circulation, intensity changed marginally, while deep-convection becomes even more pronounced in the vicinity of the cyclone center. This redistribution of potential temperature, associated with negative potential temperature advection below and positive potential temperature advection aloft, finally leading to the formation of tropical cyclone Leslie, can be inferred by investigating the plots shown in figure 20.

Later stages of development show the evolution into a hurricane on October 3, the weakening trend starting on October 4, as well as the restrengthening and reacquiring of hurricane status on October 10. However, in the next sections the time domain between September 25 and September 30 will be matter of further investigation, hence we restrict ourselves to a more in depth analysis of the tropical transition process.

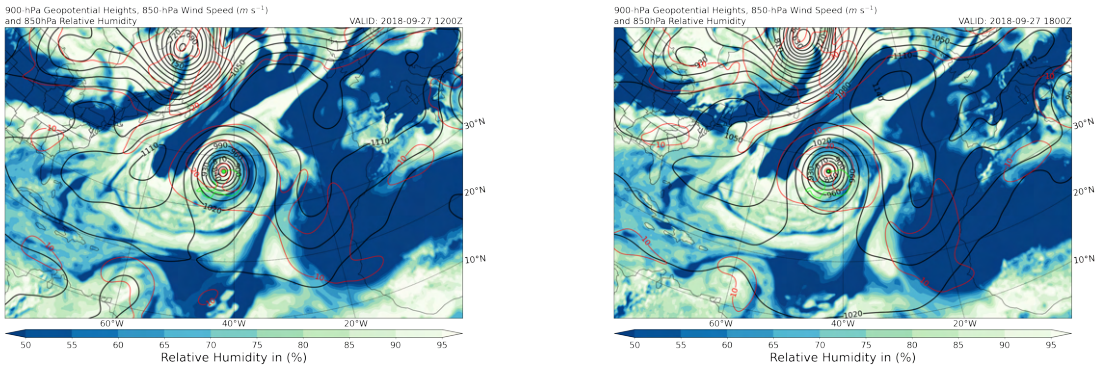

Fig. 19: Lower-Level (850 hPa) Relative Humidity Development associated with the Life Cycle of Leslie at 1200 UTC 27 September and 1800 UTC 27 September.
Colorbars highlight relative humidity while red lines denote the horizontal wind speed at levels mentioned in the upper left of the figures. Black lines characterize geopotential values at 900 hPa *indicated by the numbers labeled to them.*

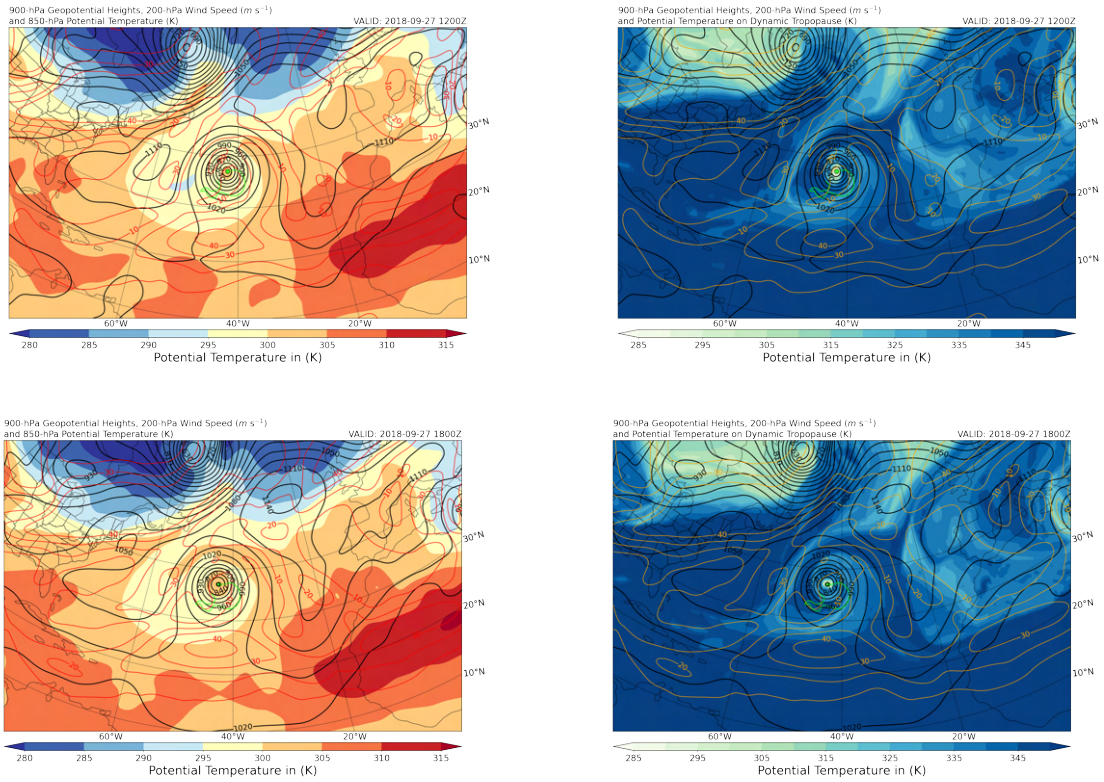

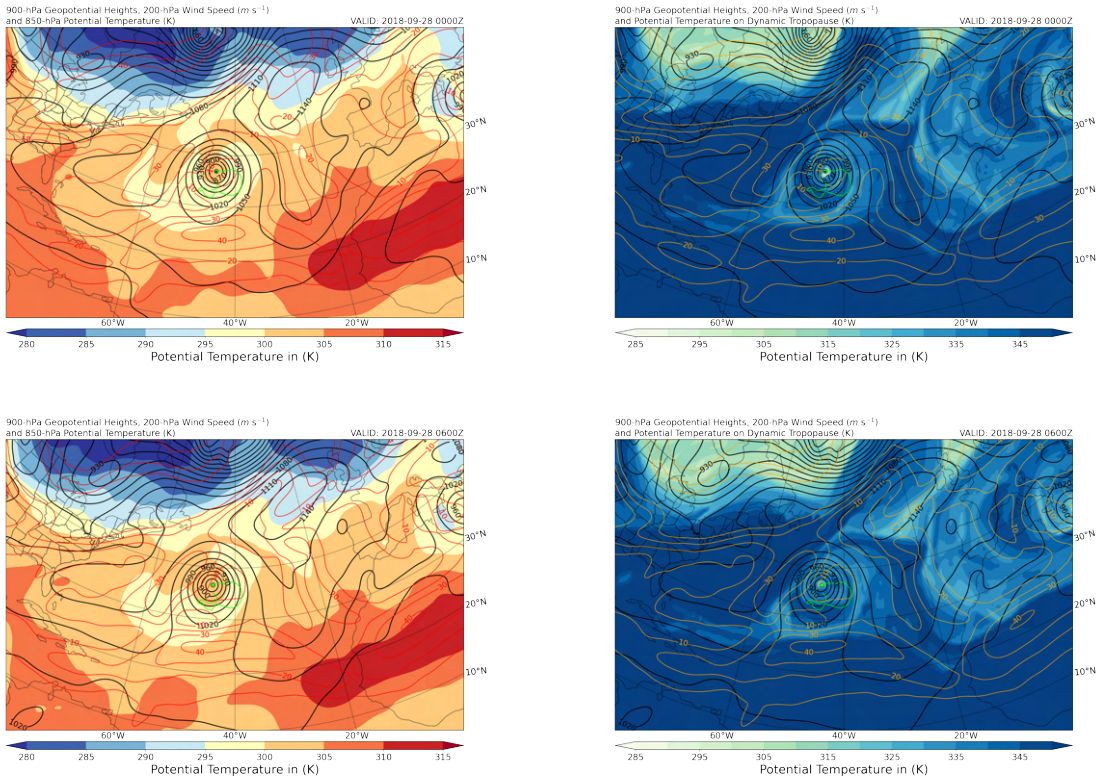

Fig. 20: Potential Temperature Development on the Dynamic Tropopause and at 850 hPa associated with the Life Cycle of Leslie between 1200 UTC 27 September and 0600 UTC 28 September.

Colorbars highlight the potential temperature in K while red/yellow lines denote the horizontal wind speed at levels mentioned in the upper left of the figures. Black lines characterize geopotential values at 900 hPa *indicated by the numbers labeled to them.*

5.1.1.2 Thermostructural Evolution

Cyclone-Phase-Space Analysis

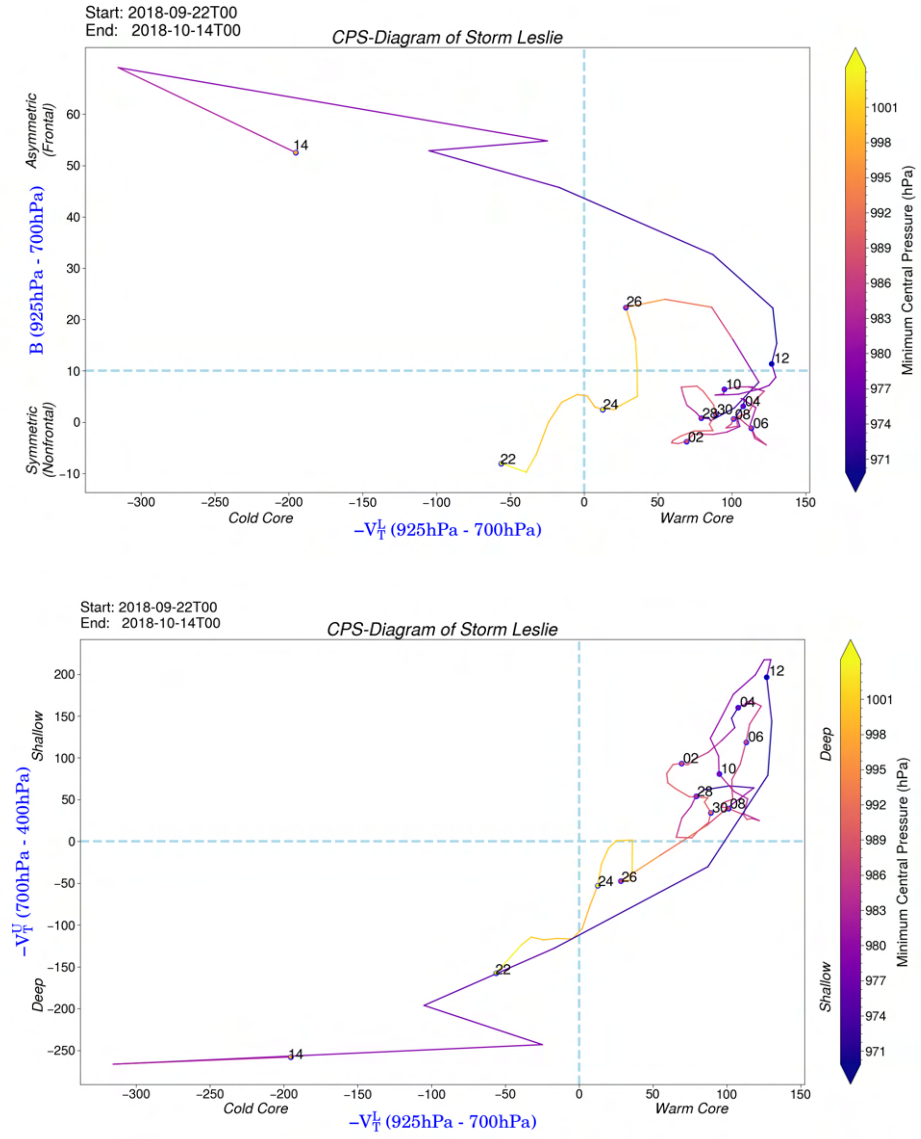

Fig. 21: CPS-Diagrams of Hurricane Leslie

Represented are the computed trajectories for the period from 0000 UTC 22 September 2018 to 0000 UTC 14 October 2018.

Two dotted blue lines are separating four quadrants characterizing each thermo-structural stages. The colorbar on the right visualizes the minimum central pressure of the storm based on physical measurements instructed by the government of the USA included in the IBTrACS database. Dates are labeled at 0000 UTC concerning the different days while being marked with a color denoting the average intensity of the respective day itself.

In the beginning of Leslie's life cycle, the formation of a subtropical storm system follows an anticyclonic wave breaking event as described in the prior section. The subtropical storm status can be inferred by regarding the B vs $-V_T^L$-diagram in figure 21, demonstrating the existence of a symmetric cold core system at the early stages of development. The reacquirement of the extratropical properties on September 25, 2018 is characterized by a comparably higher asymmetry, as well as by the transition from a deep into a more shallow warm core system (figure 21 ($-V_T^U$ vs $-V_T^L$)). As deep convection becomes more prominent due to favorable environmental conditions associated with a large frontal structure, the system undergoes tropical transition, while fully acquiring subtropical storm status on 1200 UTC 28 September 2018. This however, one might also infer by considering the development into a deep warm core structure, while being described by significant symmetry (figure 21). On 1800 UTC 29 September, deep convection, interrelated with the synoptic system itself, leads to the description as tropical storm referring to the reports of the National Hurricane Center of the USA. After remaining tropical storm and even hurricane status for a long time, Leslie was picked up by the mid-latitude westerlies and finally transitioned back into an extratropical cyclone (asymmetric cold core system), before vanishing over the Bay of Biscay on October 14, 2018 (later stages in figure 21).
Restricting ourselves to further investigate the cyclone group, we will consider two different initialization times concerning the ensemble weather forecast for each specific storm (already mentioned in section 4). Hereby, we firstly infer the cyclone-phase-space development of all four ensemble weather forecasts respectively, in order to ensure the separation in colder-, intermediate- and warmer-core groups, as mentioned in section 4.3.2.

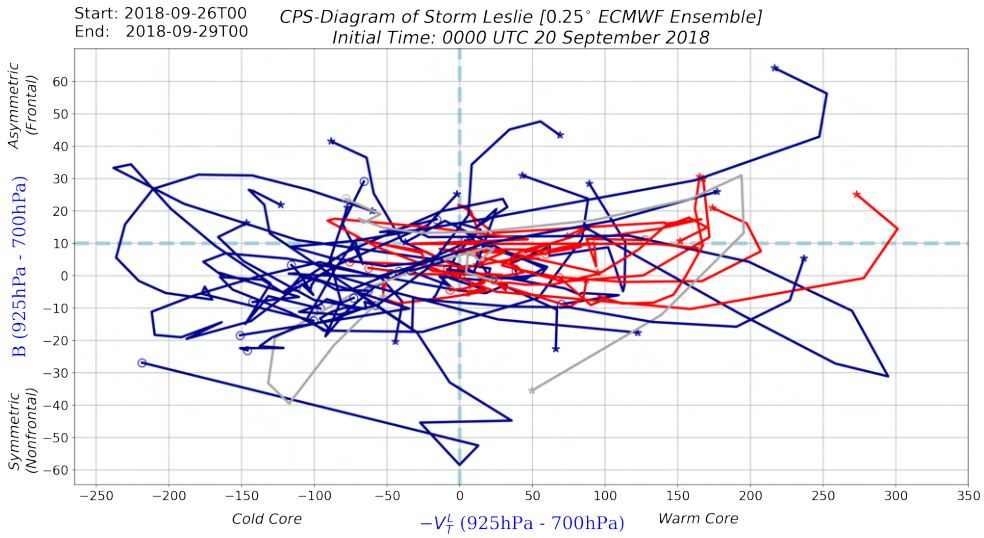

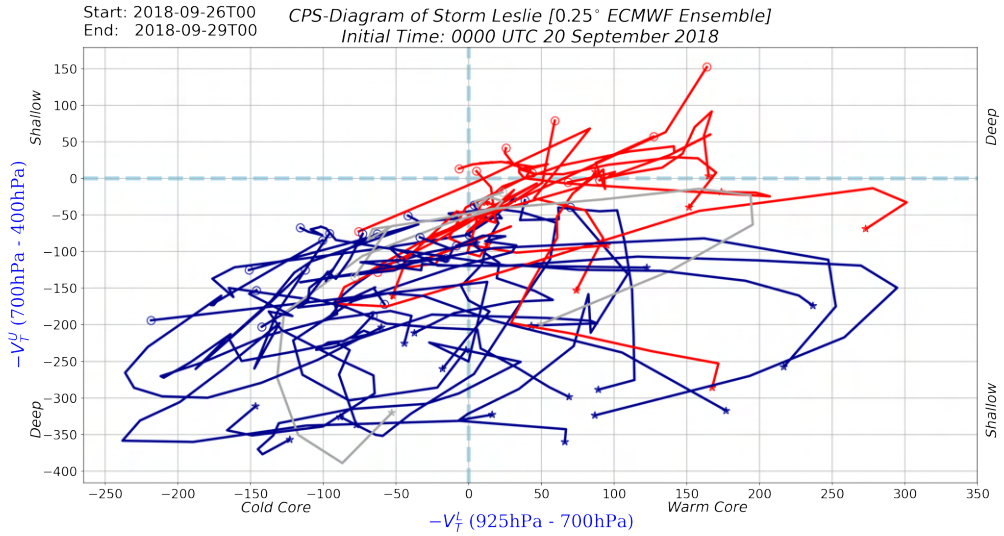

Fig. 22: CPS-Diagrams of the Ensemble Weather Prediction for Hurricane Leslie
Initialization Time: 0000 UTC 20 September 2018
Two dotted blue lines are separating four quadrants characterizing each thermo-structural stages. Stars (Start) and circles (End) are used in order to denote the start and end points of the tracks. Different colors are chosen to differentiate between the Colder-core (Blue), Intermediate-core (Grey) and Warmer-core (Red) members in adaption to [1].

Concerning the first initialization time chosen for Hurricane Leslie (0000 UTC 20 September 2018), one might infer the colder-core dominated separation of the 34 Cyclone group members into the colder-core (21 members), intermediate-core (2 members) and warmer-core (11 members) group. A rather clear distinction between the colder- and warmer-core group development can be observed by regarding the ($-V_T^U$ vs. $-V_T^L$)-diagram in particular. Colder-core members start under significantly shallower warm core conditions in comparison to the warmer-core group, while also being characterized as deep cold core systems in the end of their respective life cycle. However, the (B vs. V_T^L)-diagram, denoting the symmetry development of each specific member, does also show a clear separation of the different members. The colder-core group, while showing comparably more variability, is mostly characterized by an end point falling into the cold core section, whereas the warmer-core members are situated in the more symmetric warm core section at the end of September 29, 2018.
The presented development already solidifies the separation into the transition (warmer-core) and no-transition (colder-core) groups and works as a base in order to further investigate the interrelated PV dynamics in later sections.

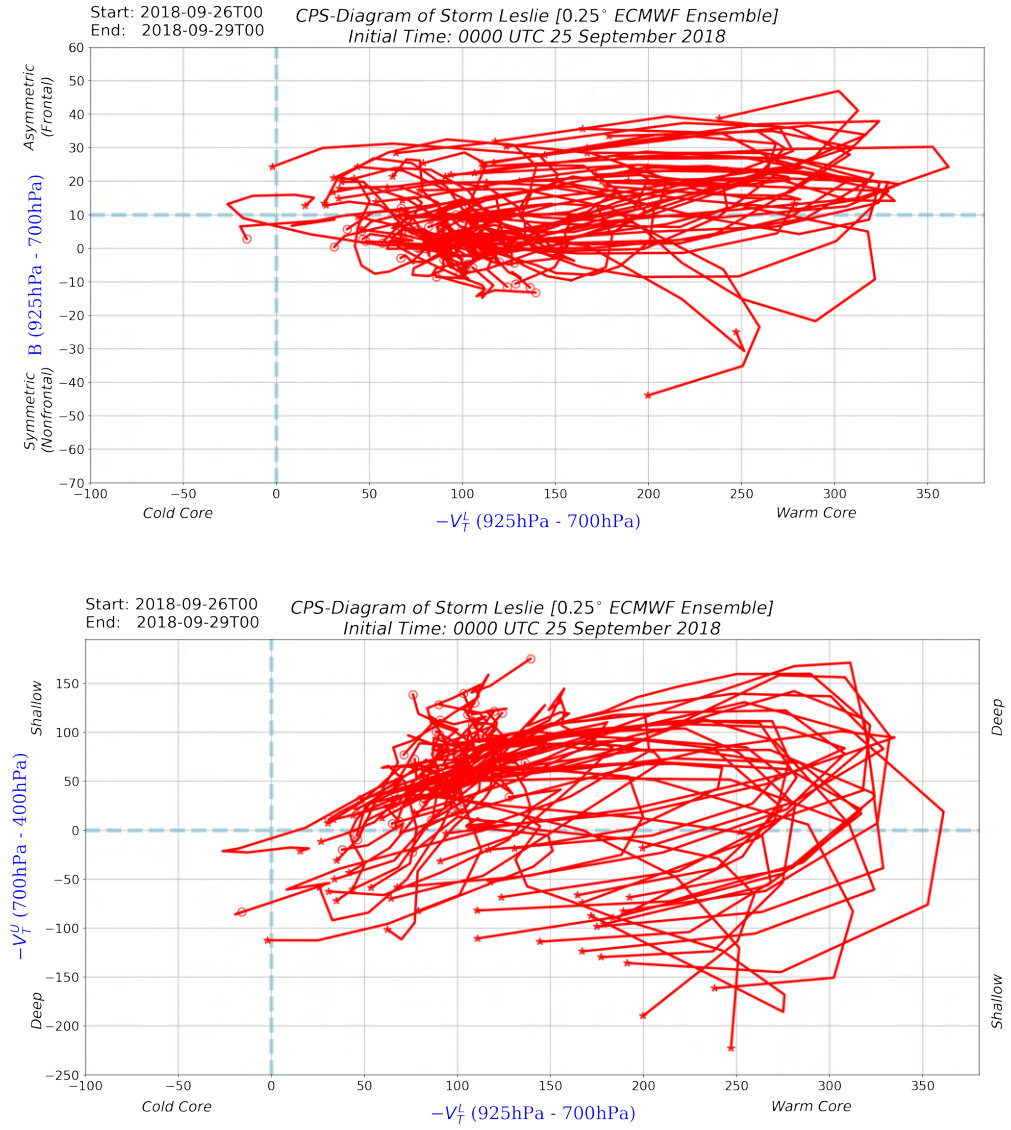

Fig. 23: CPS-Diagrams of the Ensemble Weather Prediction for Hurricane Leslie
Initialization Time: 0000 UTC 25 September 2018
Two dotted blue lines are separating four quadrants characterizing each thermo-structural stages. Stars (Start) and circles (End) are used in order to denote the start and end points of the tracks. As in figure 22, a red color is chosen to highlight the belonging to the Warmer-core (Red) group in adaption to [1].

In comparison to the ensemble development of Hurricane Paulette we will investigate in the next section, one might recognize that Leslie is characterized by a comparably ordinary tropical transition scenario. When regarding the CPS development concerning the second initialization time chosen for the analysis, we see that each of the 50 ensemble members is added to the transition group. This gives rise to the assumption, that the more complex dynamical processes, determining rather a tropical cyclone will form, must have had happen earlier than the second initialization time. This visualizes the necessity of further investigation of the pre-tropical transition conditions, which will also be demonstrated by analyzing the associated PV dynamics in section 6.

Coupling Index Progression

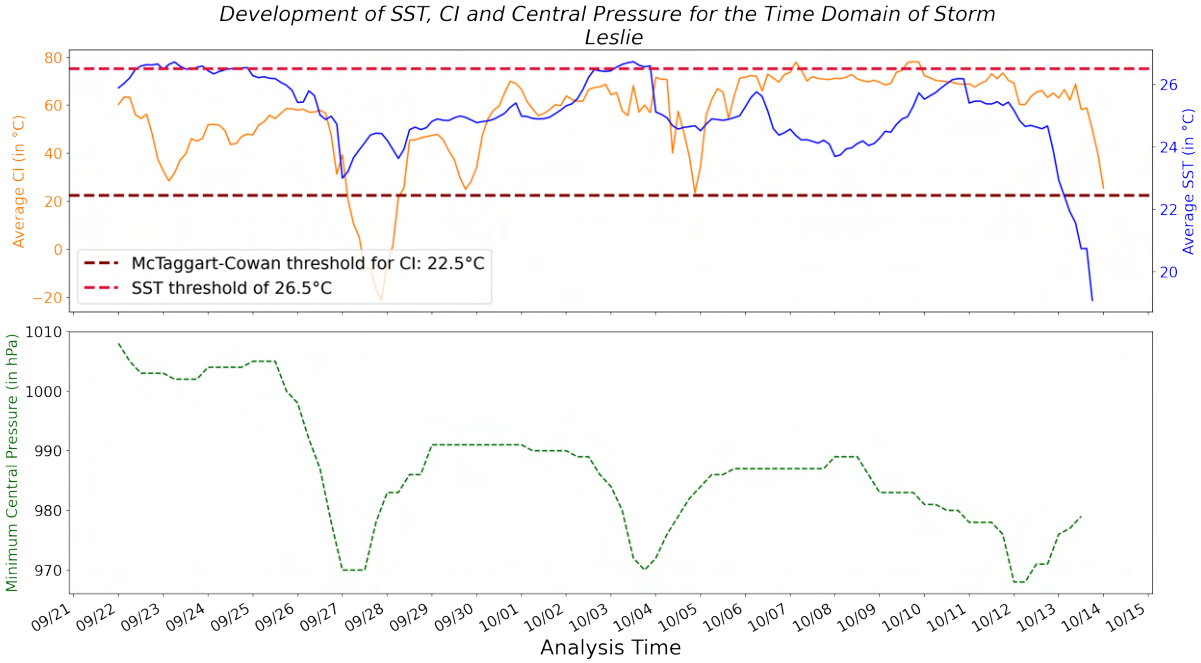

Fig. 24: CI, SST and Minimum Central Pressure Development associated with the Time Domain of Hurricane Leslie

SST (Blue solid line) and CI (Orange solid line) values are shown as a function of the analysis time. While the minimum central pressure is depicted in the lower figure, dashed lines in red and brown denote the thresholds for SST and CI respectively.

The equivalent potential temperature at 850 hPa *was calculated using the formula of Bolton (1980) [41].*

The visualized CI and SST values characterize spatial averages calculated by taking a deviation of 0.5° *with respect to the particular position of the storm (IBTrACS) into account. The minimum central pressure of the storm was inferred in the same way as given in figure 21.*

To analyze the importance of convective stability characterizing the atmospheric portion in which Leslie was embedded, one might consider the Coupling Index development, as described in section 4.2. Concerning figure 24, we can infer the highly pronounced tropical transition scenario marked by the first significant dip in the minimum central pressure of the storm on September 27, 2018. Furthermore, this intensity growth is matched by a remarkably low Coupling Index, describing the environmental conditions of also rather low bulk convective stability, which results in the realization of a larger Rossby penetration depth (section 2.6). On the other hand, sea surface temperatures fall significantly below the common used threshold for tropical cyclogenesis of 26.5° C during this time interval. Hence, the Coupling Index development describing the TT scenario in the Leslie case matches perfectly with the insights gained from the study of McTaggart-Cowan et al. [9], while characterizing the formation of a tropical cyclone over cooler waters induced by the existence of an upper-level trough. Further inspection of figure 24 sheds light on to the transition into the hurricane stage on October 3, 2018, visualized by the second drop in the minimum central pressure of the system. However, the time domain between September 26 and September 29 demonstrates the most important part for a more in-depth TT-analysis, which we will further examine by analyzing the ensemble weather forecast.

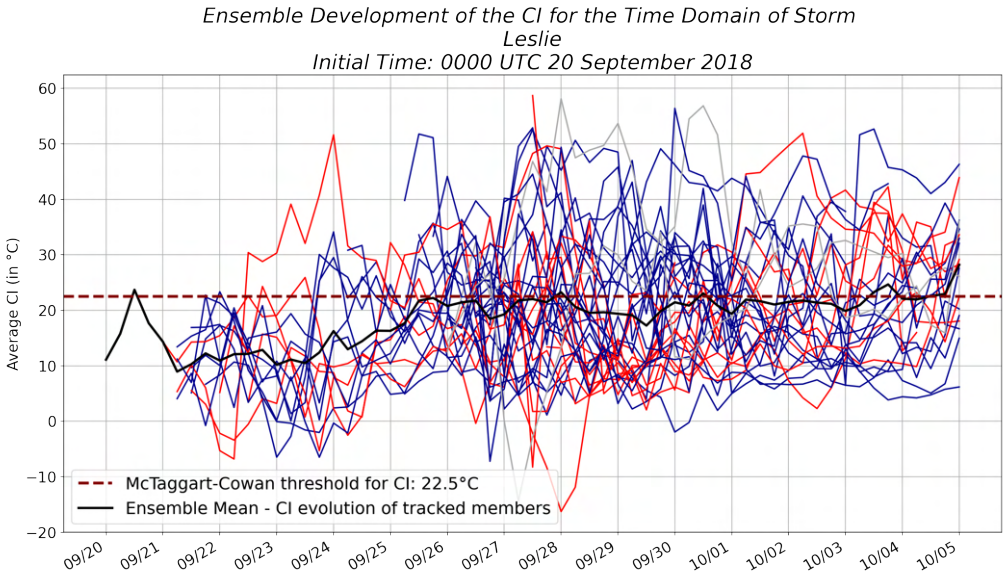

Fig. 25: Ensemble CI Development associated with the Time Domain of Hurricane Leslie
Initialization Time: 0000 UTC 20 September 2018
Colder-core (Blue solid line), Warmer-core (Red solid line) and Intermediate-core (Grey solid line) members are shown respectively. The brown dashed line is denoting the CI threshold stated in [9] while the black solid line characterizes the Ensemble Mean CI value.
The equivalent potential temperature at 850 hPa *was calculated using the formula of Bolton (1980) [41].*
The visualized CI values characterize spatial averages calculated by taking a deviation of 0.5° *with respect to the particular position of the storm (ECMWF) into account.*

Presented by figure 25, one can observe the Coupling Index development for each ensemble member concerning an initialization time of 0000 UTC 20 September 2018. Since we investigate a large variety in the realized CI value with respect to time, a restriction to each partitioning group seems advantageous. Concerning the differences in the CI development marked in figure 26, we can infer a significantly larger variety of the Coupling Index by regarding the evolution of the colder-core members. Furthermore, the dashed green line is denoting the average value of the CI restricted to a four day time window including the tropical transition event itself.

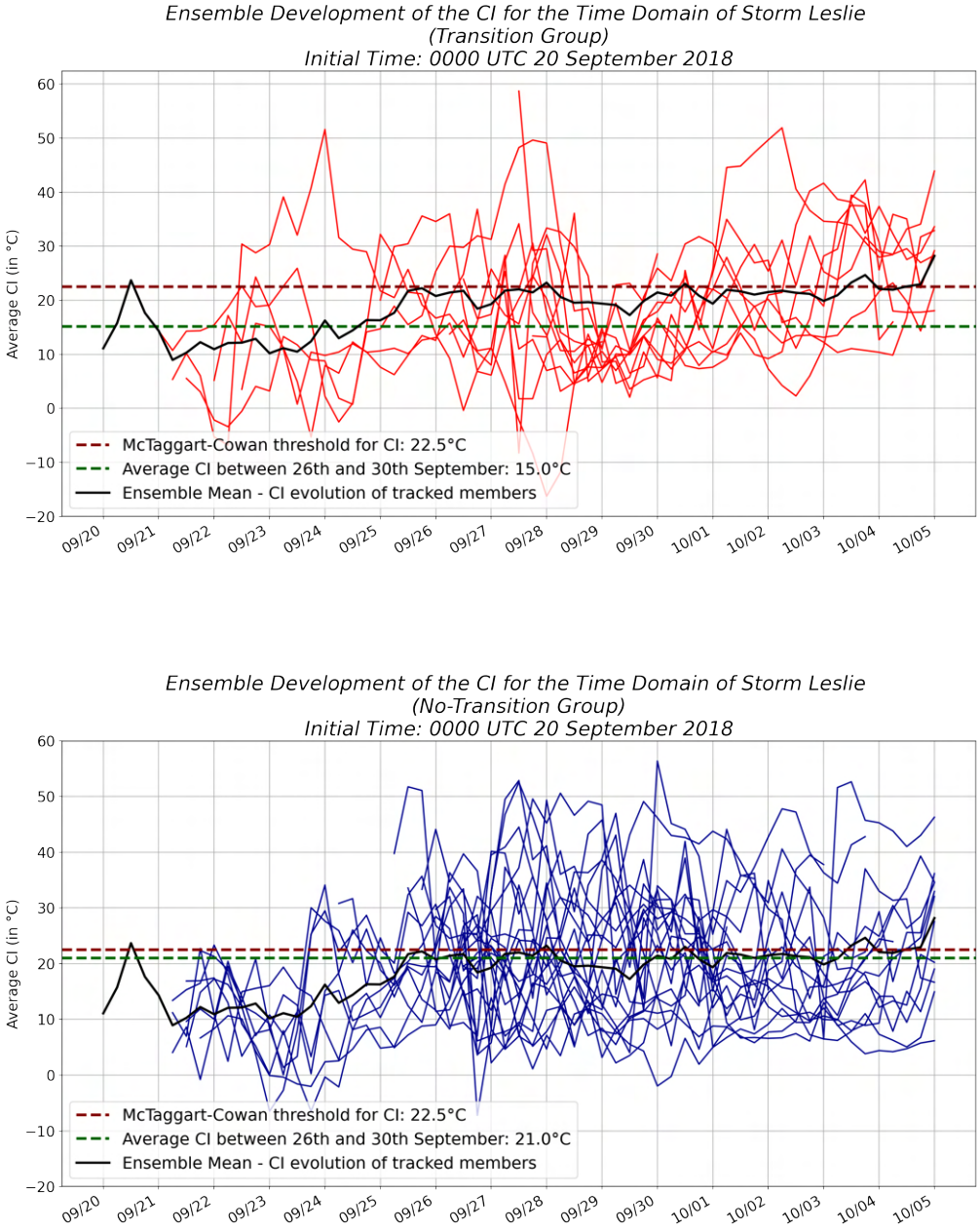

Fig. 26: Ensemble CI Development associated with the Time Domain of Hurricane Leslie
Initialization Time: 0000 UTC 20 September 2018
Colder-core (Blue solid line) and Warmer-core (Red solid line) members are shown separately. The brown dashed line is denoting the CI threshold stated in [9] whereas the dark green dashed line characterizes the calculated average of the Coupling Index for the time domain already investigated in the CPS diagrams. The black solid line characterizes the Ensemble Mean CI value.
The equivalent potential temperature at 850 hPa *was calculated using the formula of Bolton (1980) [41].*
The visualized CI values characterize spatial averages calculated by taking a deviation of 0.5° *with respect to the particular position of the storm (ECMWF) into account.*

In the case of Hurricane Leslie, we are investigating a significantly lower CI average during the TT development for the transition group in comparison to the no-transition members, which depicts the logical result one might expect. A lower Coupling Index constitutes a larger Rossby penetration depth, as investigated in section 2.6, therefore demonstrating a more pronounced coupling of upper and lower tropospheric dynamics, leading to a higher probability for TT realization.

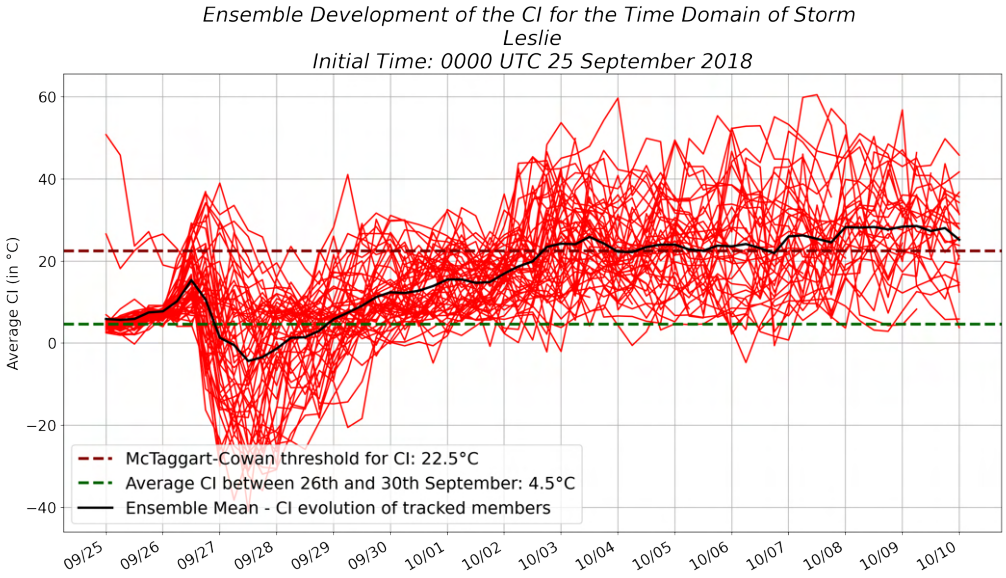

Fig. 27: Ensemble CI Development associated with the Time Domain of Hurricane Leslie
Initialization Time: 0000 UTC 25 September 2018
Colder-core (Blue solid line) and Warmer-core (Red solid line) members are shown separately. The brown dashed line is denoting the CI threshold stated in [9] whereas the dark green dashed line characterizes the calculated average of the Coupling Index for the time domain already investigated in the CPS diagrams. The black solid line characterizes the Ensemble Mean CI value.
The equivalent potential temperature at 850 hPa *was calculated using the formula of Bolton (1980) [41].*
The visualized CI values characterize spatial averages calculated by taking a deviation of 0.5° *with respect to the particular position of the storm (ECMWF) into account.*

As already stated in section 5.1.1.2, all members of the second initialization step belong to the transition group. This can also be inferred by regarding the CI development given in figure 27, where one recognizes the average CI value of 4.5° C, falling below the hypothesised threshold of McTaggart-Cowan et al. [9]. Furthermore, the drop in the respective CI development on late September 26, as visualized in the synoptic overview section, becomes clearly visible in figure 27. This represents a difference in comparison to the evolution initialized on September 20, 2018.
To conclude the given findings, we state that favorable conditions concerning convective stability might not be crucial points in realizing a successful TT process in the Leslie case. Transition group members might be characterized by a significantly lower CI average in comparison to the no-transition cluster. However, all groups fulfill the criterion of falling below the threshold stated by McTaggart-Cowan et al..

5.1.2 Hurricane Paulette

5.1.2.1 Synoptic Development

Evolution and development of Hurricane Paulette are quite distinctive from the pathway which characterizes the temporal progression of storm Leslie in 2018. Following the interaction of an African easterly wave and a low pressure system to the west, the pre-Paulette tropical depression forms on 0000 UTC 7 September 2020. Processes associated with the embedment of the storm system in an environment of deep layer shear, due to the presence of an upper-level trough, lead to several intensity changes over the next couple of days.

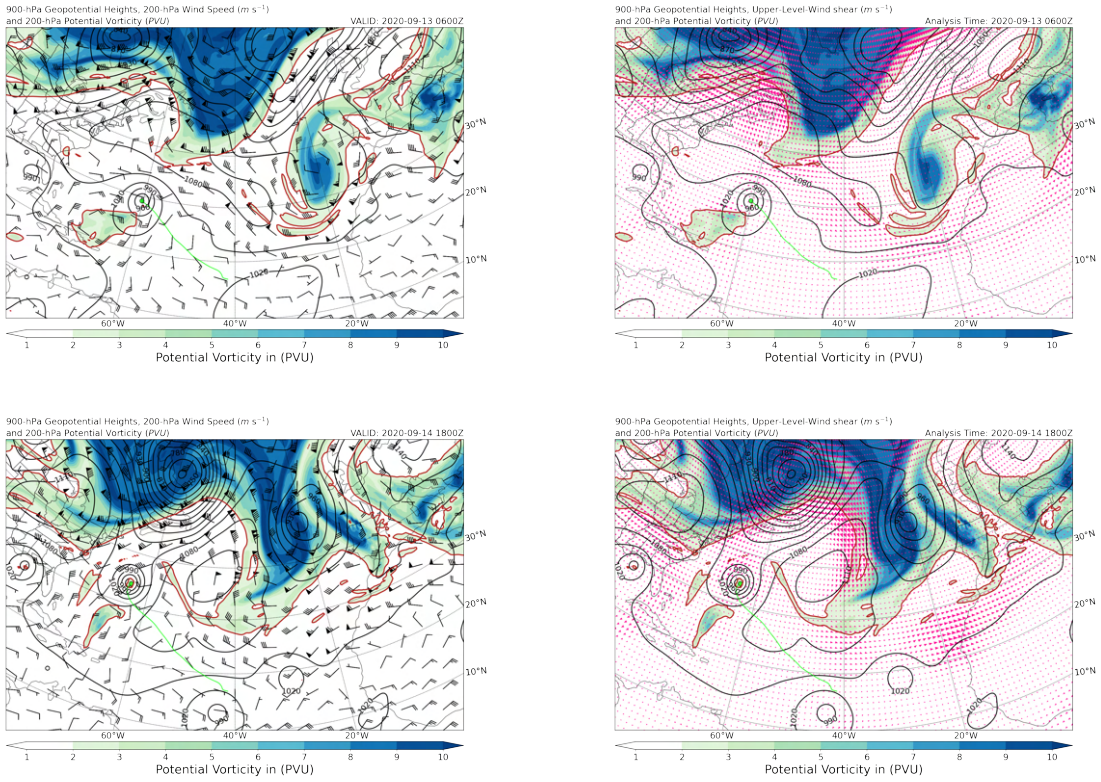

Fig. 28: Upper-Level (200 hPa) Potential Vorticity Development associated with the Life Cycle of Paulette on 0600 UTC 13 September and 1800 UTC 14 September.
Colorbars highlight potential vorticity in PVU while red arrows denote upper-level wind shear and black barbs characterize the wind speed in Beaufort scaling. Black lines characterize geopotential values at 900 hPa *indicated by the numbers labeled to them.*

As a result of the weakening trend of the deep layer shear, the storm intensifies and reaches a stage, at which the associated winds reach hurricane force on September 13, 2020. Peak intensity is reached at 1800 UTC 14 September 2020 (figure 28). While moving further north, the hurricane interacts with a mid-latitude baroclinic zone (characterized by deep layer shear (figure 29)) and undergoes an extratropical transition process on September 15, 2020, prior to its inclusion into the ridge itself.

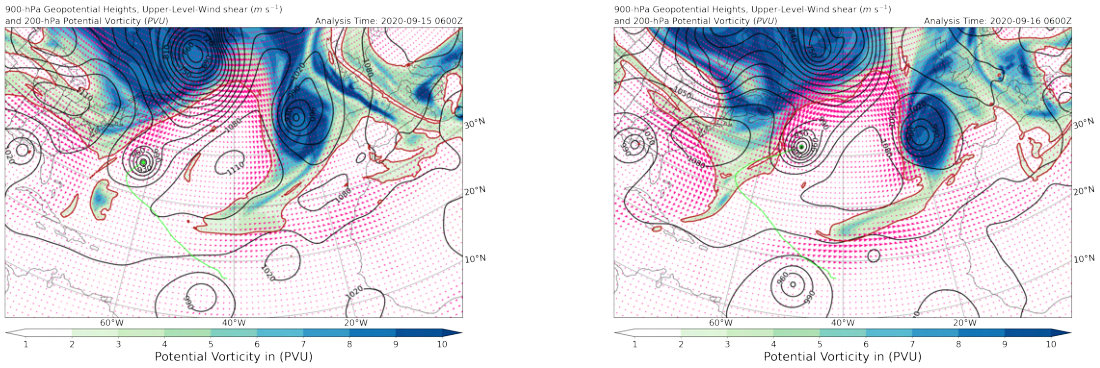

Fig. 29: Upper-Level (200 hPa) Potential Vorticity Development associated with the Life Cycle of Paulette on 0600 UTC 15 September and 0600 UTC 16 September.
Colorbars highlight potential vorticity in PVU while red arrows denote upper-level wind shear respectively. Black lines characterize geopotential values at 900 hPa *indicated by the numbers labeled to them.*

The development of Paulette following September 19, 2020 will be of further interest for our analysis concerning TT processes. While embedded in a flow connected with a broad cluster of comparably large upper-level PV, the frontal features associated with the storm system itself become less pronounced (figure 30).

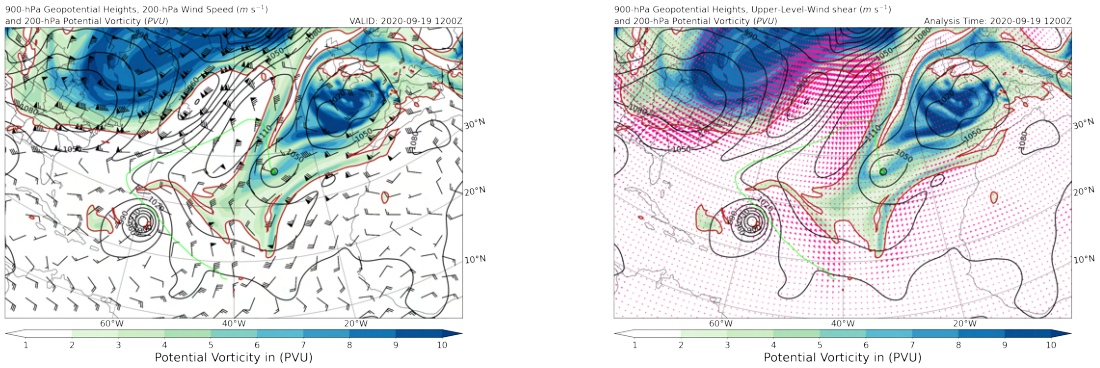

Fig. 30: Upper-Level (200 hPa) Potential Vorticity Development associated with the Life Cycle of Paulette on 1200 UTC 19 September.
Colorbars highlight potential vorticity in PVU while red arrows denote upper-level wind shear and black barbs characterize the wind speed in Beaufort scaling. Black lines characterize geopotential values at 900 hPa *indicated by the numbers labeled to them.*

While the steering flow dies out, demonstrating the early stages of the development of an extraordinary PV tongue, the convection interrelated with the existence of the low becomes even more sufficient in order to realize tropical cyclogenesis on 1800 UTC 20 September 2020 (figure 31).

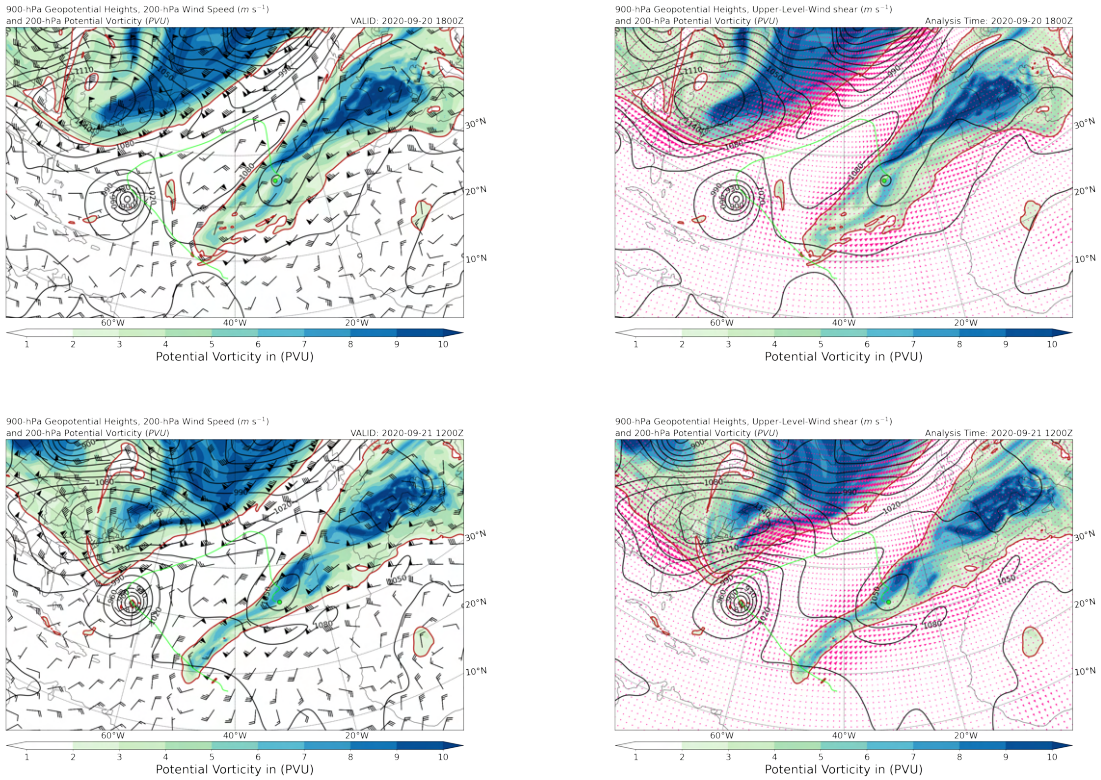

Fig. 31: Upper-Level (200 hPa) Potential Vorticity Development associated with the Life Cycle of Paulette on 1800 UTC 20 September and 1200 UTC 21 September.
Colorbars highlight potential vorticity in PVU while red arrows denote upper-level wind shear and black barbs characterize the wind speed in Beaufort scaling. Black lines characterize geopotential values at 900 hPa *indicated by the numbers labeled to them.*

The secondary peek in intensity is reached at 0000 UTC 22 September, which can also be seen by regarding the CI analysis presented in later sections. A significant growth of upper-level shear confronting the storm at later stages leads to a weakening trend and realization of the post-tropical cyclone status. Finally, the interaction with another baroclinic zone leads to a second restrengthening of the storm on September 23, 2020, before being embedded in an environment characterized by cooler surface waters and dry stable air, which marks the end of Paulette's life cycle.

5.1.2.2 Thermostructural Evolution

Cyclone-Phase-Space Analysis

In contrast to the initial storm status described in the Leslie case, our investigation of Paulette starts with the formation of a tropical depression and tropical storm later on, resulting from a tropical easterly wave precursor. This however can be inferred by regarding figure 32 (B vs $-V_T^L$), demonstrating the starting point in the lower right corner, while describing an already existing symmetric warm core structure. The posterior intensity changes, as well as the acquirement of peak intensity on late September 14, 2020, described in section 5.1.2.1, are highlighted by the development of the minimum central pressure of the storm.

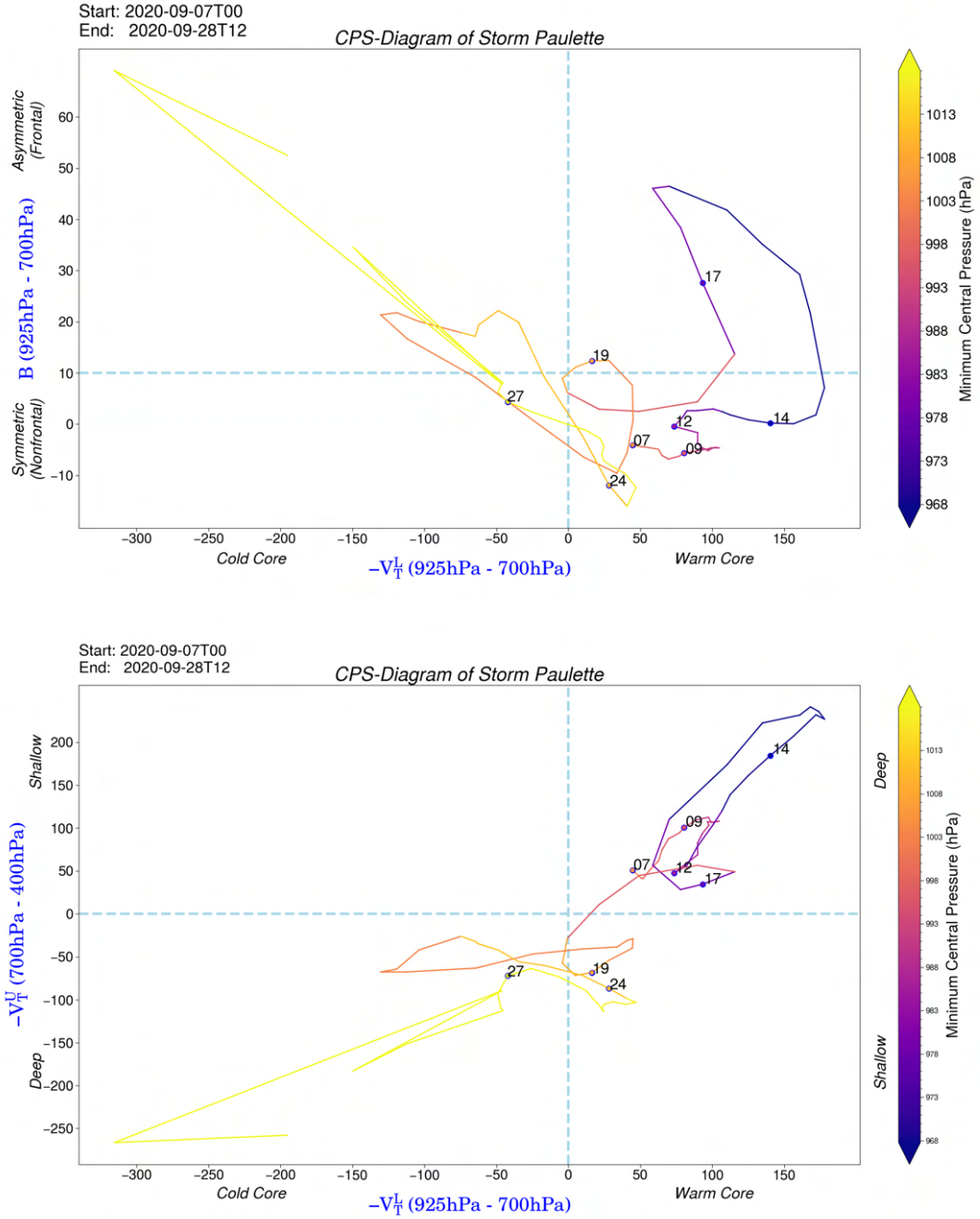

Fig. 32: CPS-Diagrams of Hurricane Paulette
Represented are the computed trajectories for the period from 0000 UTC 07 September 2020 to 1200 UTC 28 October 2020.
Computations were done as already presented in the description of figure 21.

The extratropical transition process, while not obviously pronounced in figure 32 ($-V_T^U$ vs $-V_T^L$), might be inferred by the initial development into a highly asymmetric warm core system, demonstrated in Graph 32 (B vs $-V_T^L$). However, the process of acquiring extratropical characteristics culminates on late September 18, 2020, with the transition into a deep asymmetric cold core system for a small amount of time. Following the synoptic evaluation, convection becomes more pronounced when sufficient environmental conditions for tropical cylogenesis are present, due to the already described existence of a low pressure system. This process is characterized by the

re-transition into a symmetric warm core system of significant deepness on September 20, 2020, visualized in figure 32.
Following a certain weakening trend, due to larger upper-level shear values, one might further infer the third peak in intensity on September 23, resulting from the storm-barocinic zone interaction. The later stages are obviously characterized by the same sort of development as already investigated in the Leslie case. The final evolution of the storm is described by the transition from a symmetric warm core system into an asymmetric cold core, followed by the later vanishing of the storm as such.

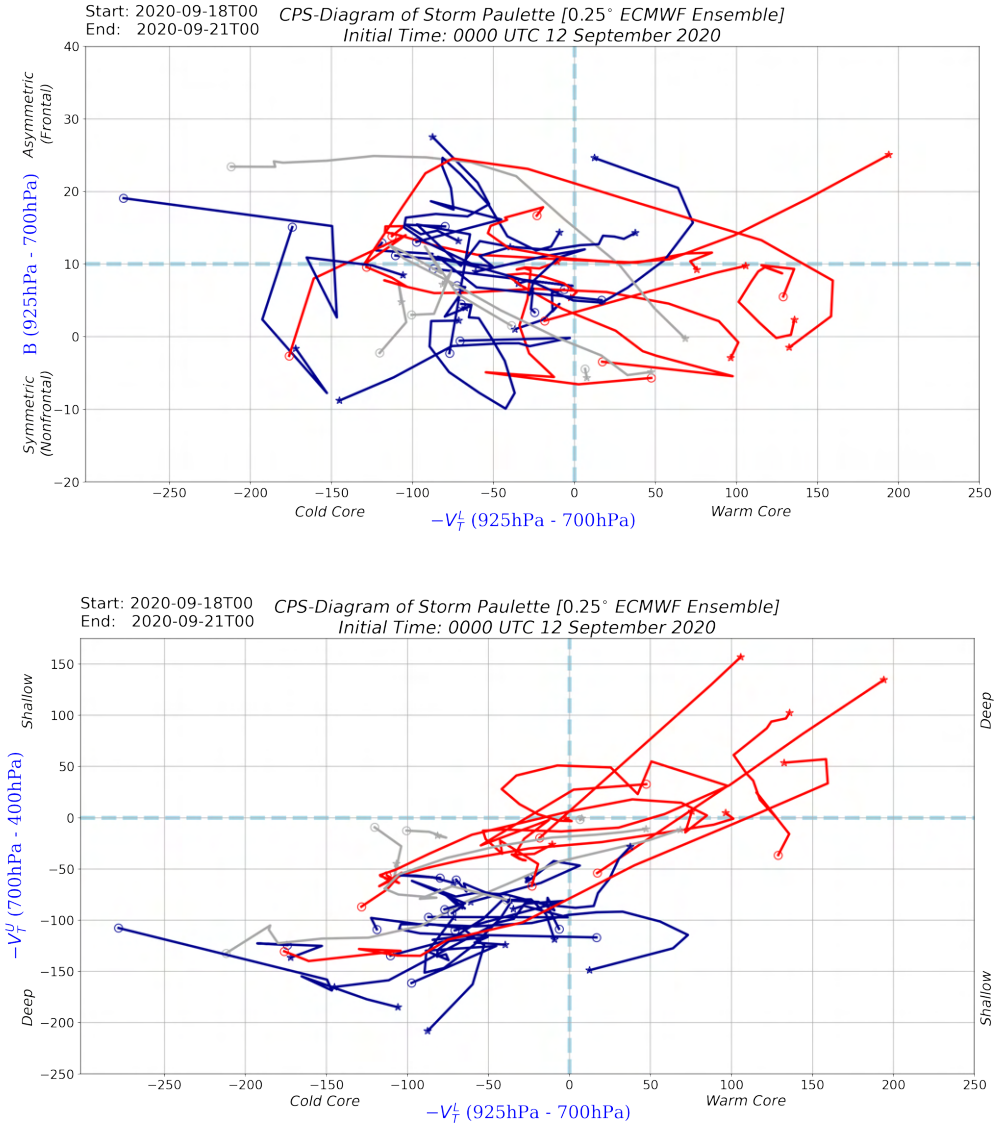

Fig. 33: CPS-Diagrams of the Ensemble Weather Prediction for Hurricane Paulette
Initialization Time: 0000 UTC 12 September 2020
Two dotted blue lines are separating four quadrants characterizing each thermo-structural stages. Stars (Start) and circles (End) are used in order to denote the start and end points of the tracks. As in figure 22, different colors are chosen to differentiate between the Colder-core (Blue), Intermediate-core (Grey) and Warmer-core (Red) members in adaption to [1].

Regarding the ensemble weather prediction development for the first initialization time (0000 UTC 12 September 2012) in the Paulette case, we are able to infer the evolution of 27 cyclone group members. Here, a similar partitioning as already investigated for the Leslie case is applied, with 9 members belonging to the warmer-core group, while 14 members are added to

the colder-core section. The most significant difference can be seen by regarding the ($-V_T^U$ vs. $-V_T^L$)-diagram, where most of the warmer-core members start in an environment associated with a deep warm core characteristic, while colder-core members are more restricted to the lower left corner in the mentioned diagram.

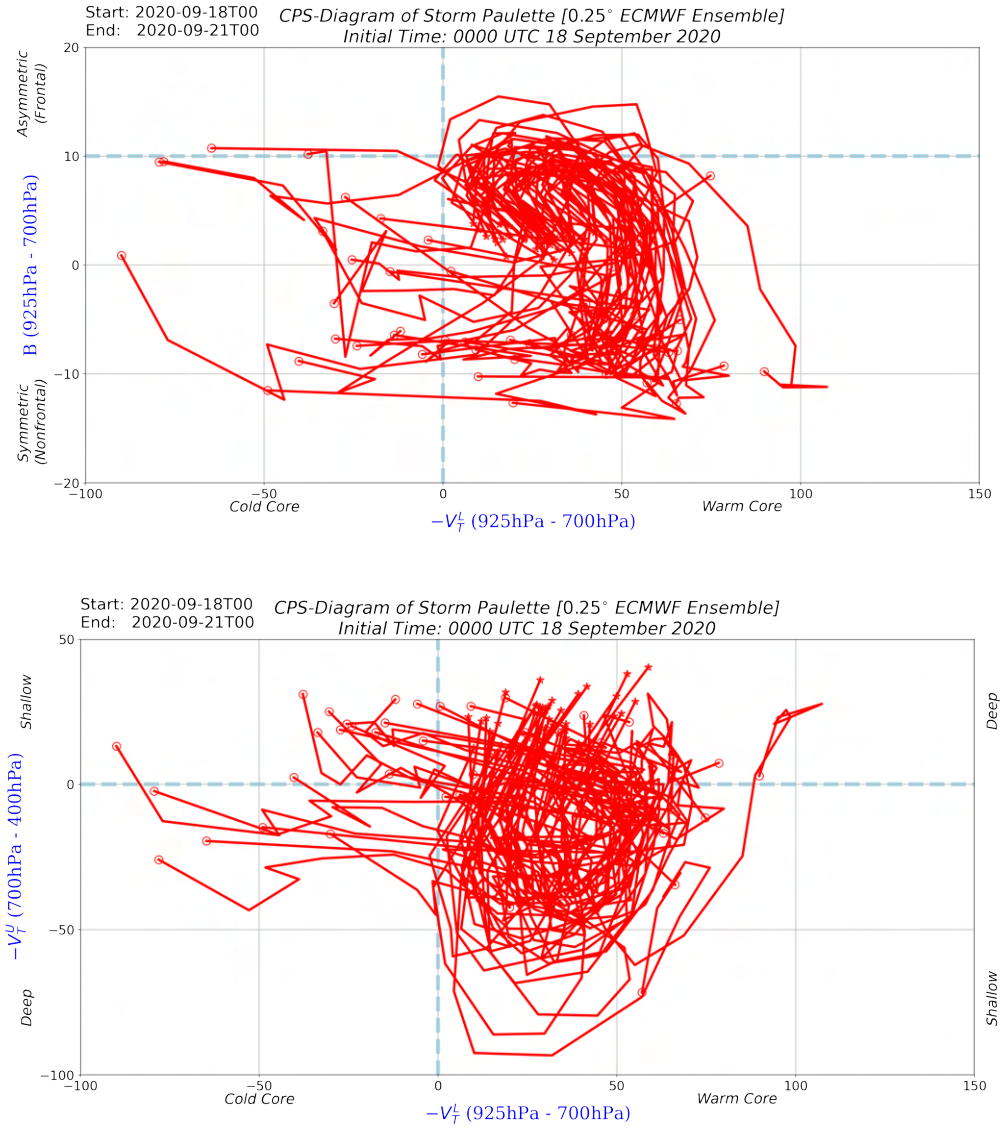

Fig. 34: CPS-Diagrams of the Ensemble Weather Prediction for Hurricane Paulette Initialization Time: 0000 UTC 18 September 2018

Two dotted blue lines are separating four quadrants respectively, characterizing each thermo-structural stages. Stars (Start) and circles (End) are used in order to denote the start and end points of the tracks. A red color is chosen to highlight the belonging to the Warmer-core (Red) group in adaption to [1].

In accordance with the analysis of the second initialization step in the Leslie case, the ensemble weather forecast concerning storm Paulette, initialised on 0000 UTC 18 September 2020, is also characterized by the occurrence of transition group members only. The given group partitioning demonstrates, that further investigation of the pre-tropical transition conditions, preceding the second initialization step, is necessary to gain a better understanding of the reasons leading to the respective TT scenario itself. Later on, this legitimates the restriction on to the analysis of the first initialization step, when it comes to the inspection of the 3-D PV evolution in the Paulette and Leslie case as well.

Coupling Index Progression

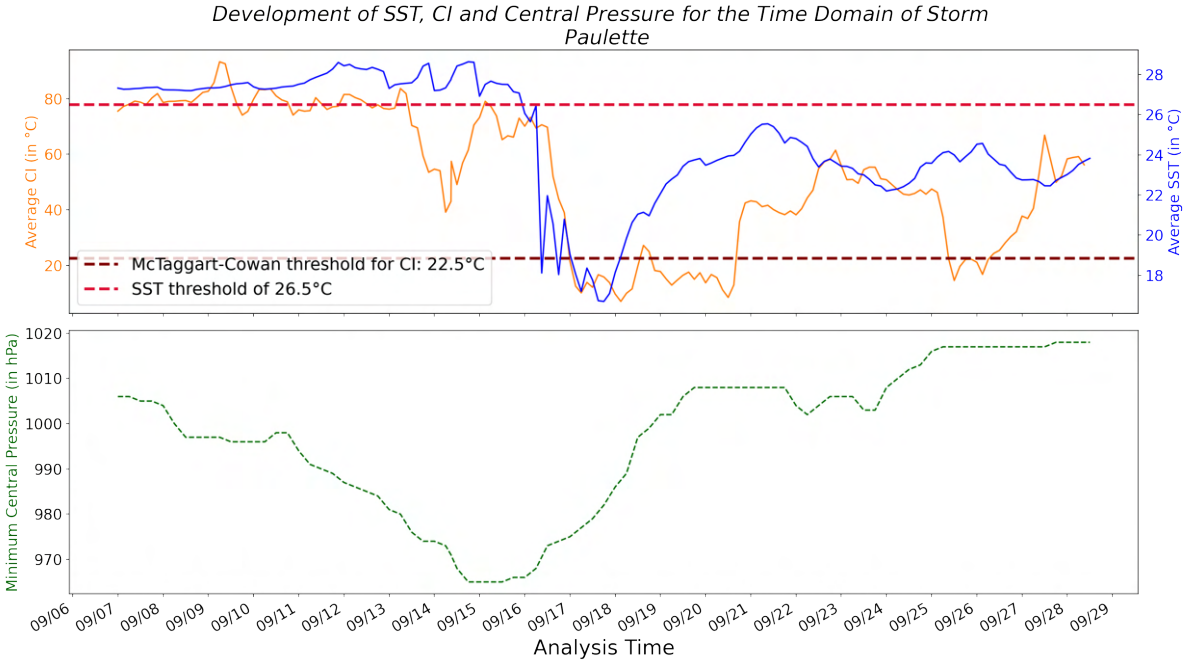

Fig. 35: CI, SST and Minimum Central Pressure Development associated with the Time Domain of Hurricane Paulette
Computations and style of demonstration follow the one already given in figure 24.

By investigation of figure 35, one recognizes the hurricane development of storm Paulette and acquisition of peak intensity on September 14, 2020, marked by a significant pressure drop. The enhancement of convection associated with the upper level low, leading to the tropical transition process, can be inferred by regarding the evolution on September 19 in figure 35. As observed in the Leslie case, Paulette's development confirms the statements given by McTaggart-Cowan et al. [9]. While embedded in an environment, characterized by a Coupling Index falling below the mentioned threshold of 22.5° C, baroclinic induced TT is realized over remarkably cooler waters in comparison to the sea surface temperature threshold common used to describe a necessary precondition for tropical cyclogenesis. Also denoted are the two post-tropical restrengthening cycles on September 23 and September 24, marked by the pressure drops at these stages of development.
As can already be inferred, the development of Hurricane Paulette visualizes a more extraordinary evolution in comparison to the scenarios investigated in the Leslie case. The marginal environmental conditions near the Azores led to significant difficulties in the prediction of tropical cyclone development. An investigation of the ensemble weather forecast, associated with the storm systems studied in the sections above, will shed even more light on to the relevant differences in physical environmental development.

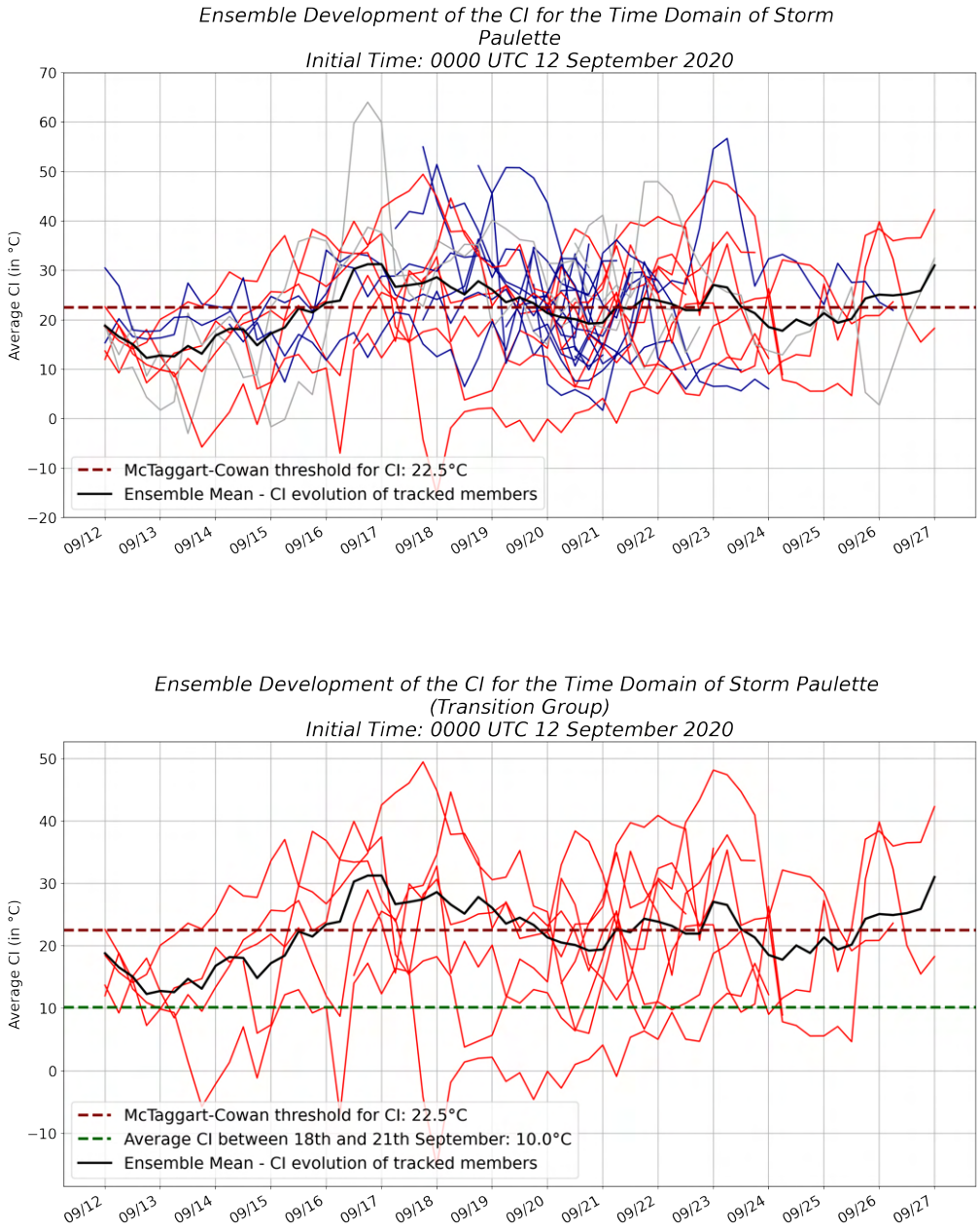

Fig. 36: Ensemble CI Development associated with the Time Domain of Hurricane Paulette
Initialization Time: 0000 UTC 12 September 2020
Colder-core (Blue solid line) and Warmer-core (Red solid line) members are shown separately. The brown dashed line is denoting the CI threshold stated in [9] whereas the dark green dashed line characterizes the calculated average of the Coupling Index for the time domain already investigated in the CPS diagrams. The black solid line characterizes the Ensemble Mean CI value.
The equivalent potential temperature at 850 hPa *was calculated using the formula of Bolton (1980) [41].*
The visualized CI values characterize spatial averages calculated by taking a deviation of 0.5° *with respect to the particular position of the storm (ECMWF) into account.*

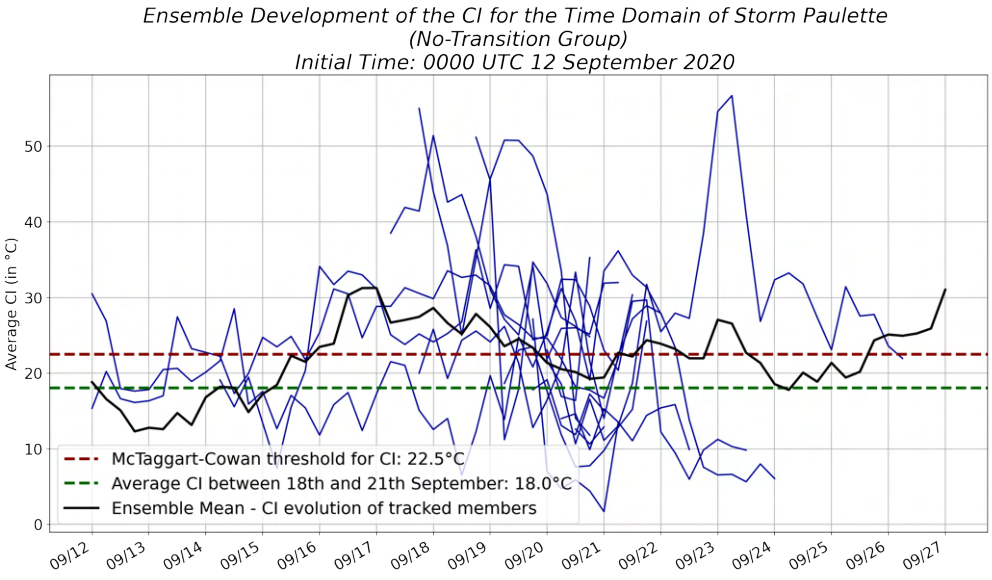

Fig. 37: Ensemble CI Development associated with the Time Domain of Hurricane Paulette (No-Transition Group)
Initialization Time: 0000 UTC 12 September 2020
The brown dashed line is denoting the CI threshold stated in [9] whereas the dark green dashed line characterizes the calculated average of the Coupling Index for the time domain already investigated in the CPS diagrams. The black solid line characterizes the Ensemble Mean CI. Equivalent potential temperature was calculated using the formula of Bolton (1980) [41]. The visualized CI values characterize spatial averages calculated by taking a deviation of 0.5° *with respect to the particular position of the storm (ECMWF) into account.*

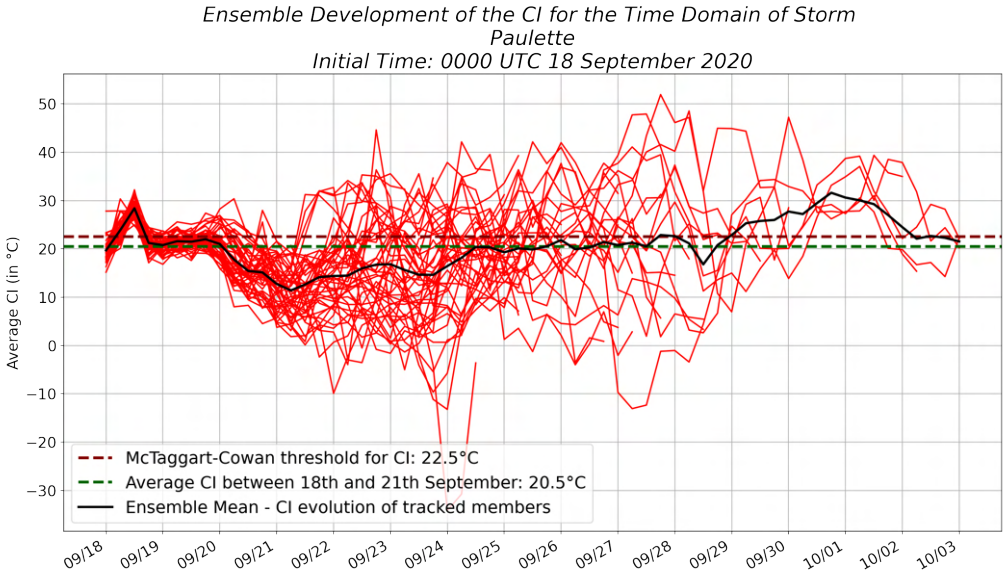

Fig. 38: Ensemble CI Development associated with the Time Domain of Hurricane Paulette
Initialization Time: 0000 UTC 18 September 2020
Only Warmer-core (Red solid line) members are shown. The brown dashed line is denoting the CI threshold stated in [9] whereas the dark green dashed line characterizes the calculated average of the Coupling Index for the time domain already investigated in the CPS diagrams. The black solid line characterizes the Ensemble Mean CI value.
Equivalent potential temperature was calculated using the formula of Bolton (1980) [41]. The visualized CI values characterize spatial averages calculated by taking a deviation of 0.5° *with respect to the particular position of the storm (ECMWF) into account.*

Similar to the Leslie case, the ensemble CI development of Hurricane Paulette shows a significantly lower CI average value when concerning the members of the transition group of the first initialization step.
However, considering the CI development investigated by using the second initialization time (figure 36), the difference of the average CI value in comparison to the mentioned threshold becomes marginal. This depicts the complex TT realization on September 20, 2020, as already inferred in the synoptic overview (see section 5.1.2.1). Nevertheless, concerning the fact that the average CI value of all partition group members falls below the threshold investigated by McTaggart-Cowan et al., one might assume that the convective stability does not represent a crucial point in influencing the realization of TT the Paulette case. At the same time, this also points to the necessity of further investigation of the environmental conditions preceding September 18, 2020.
The synoptic overview of Leslie and Paulette, as well as the CPS and CI analysis, represents the extraordinary development of these storm systems. One special characteristic, which stands out in both descriptions, is the necessity of an upper level trough structure or PV streamer, serving as a catalyst for the tropical transition scenarios in the presented cases. Hence, in the next sections we will further examine the given PV features in a more detailed way, while also using Met.3D in order to visualize the associated streamers in three dimensions.

6 3-D Potential Vorticity Examination

In order to ensure a proper 3-D potential vorticity analysis, the same algorithm as introduced in [12] is used. Based on temperature and horizontal velocity data on the 50, 100, 200, 250, 300, 400, 500, 700, 850 and 925 hPa isobars, PV is calculated on isentropic levels, while applying an interpolation, to guarantee a resolution of 2 K necessary for results of sufficient accuracy. Nevertheless, a visualization on pressure levels is chosen to ensure better comparability with studies in other fields of atmospheric sciences. Data on the presented isobars is used, because of the limited availability of ECMWF ensemble data, which is applied to investigate the development of the different members in section 6.2. Since the focus of these case studies is a synoptic analysis, a spatial resolution of 0.5° is utilized in this particular case.
To firstly reemphasize the synoptic development of both, Leslie and Paulette, the next section outlines a 3-D analysis of the already inferred findings in the PV framework.

6.1 PV Development based on ERA5 Reanalysis

Investigation of Storm Leslie

Referring to section 5.1.1, the cyclonic roll-up of the upper-level PV streamer on September 27, 2018 is associated with the development of a surface low characterized by a large frontal structure. This frontal structure is further visualized by the strongly pronounced rainband feature demonstrated in figure 39.

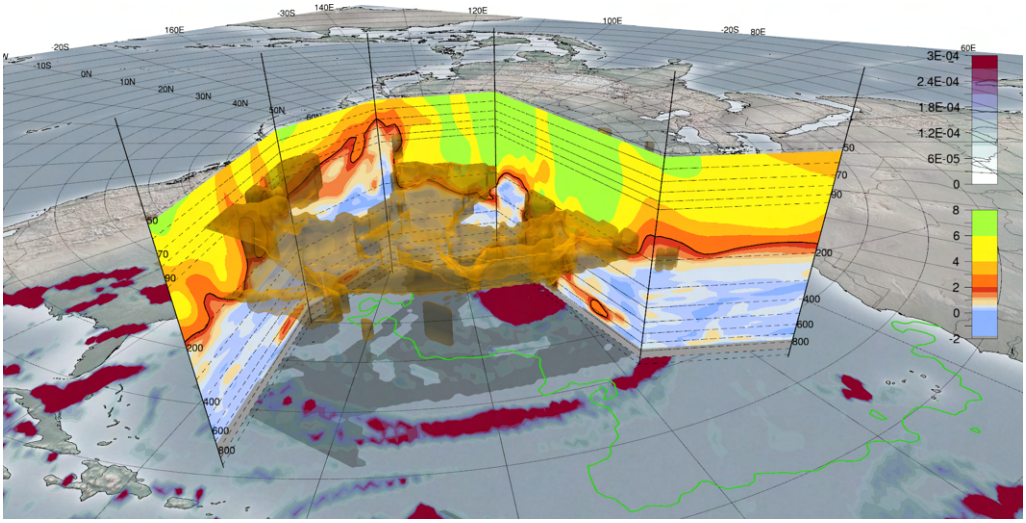

Fig. 39: PV Development of Tropical Storm Leslie based on ERA5 Reanalysis
The PV streamer associated with storm system Leslie is shown for 0600 UTC 27 September 2018.
A vertical cross section is used to visualize the PV (in PVU) on pressure levels denoted by the colorbar on the right hand side.
The respective streamer is colored in brown, while the total precipitation in meters accumulated over one hour is characterized by the colorbar on the right as well.
A lime colored isoline is added in order to visualize the 26.5° C *sea surface temperature threshold.*

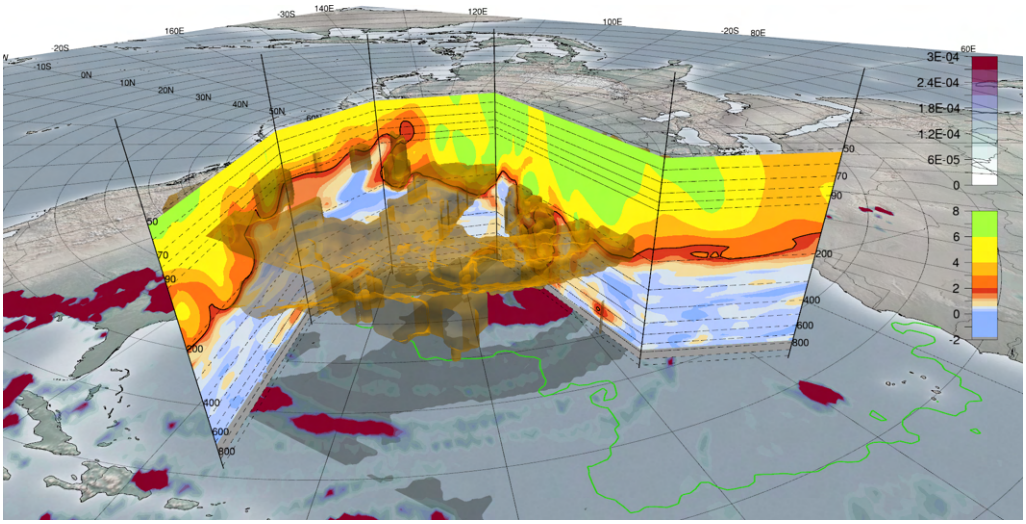

Fig. 40: PV Development of Tropical Storm Leslie based on ERA5 Reanalysis
The PV streamer associated with storm system Leslie is shown as it is done in figure 39, but for 1200 UTC 27 September 2018
What should be highlighted is the pronounced PV tower structure on the eastern side of the vertical cross section.

The further development of the PV tower structure is not only characteristic for the evolution of a tropical storm but also for the embedment of the system in an environment with low vertical shear (as already stated in section 5.1.1). Such an evolution would not be possible otherwise because of the significantly more inefficient heating due to the asymmetry of the system (see section 2.4). Looking into later development stages of Leslie, it becomes evident that the hurricane domain is characterized by a less pronounced upper-level PV field. This is because the heating due to latent heat release, as a result of the condensation of water vapor, leads to negative PV advection above the heating region as already stated in section 2.4 as well.

Investigation of Storm Paulette

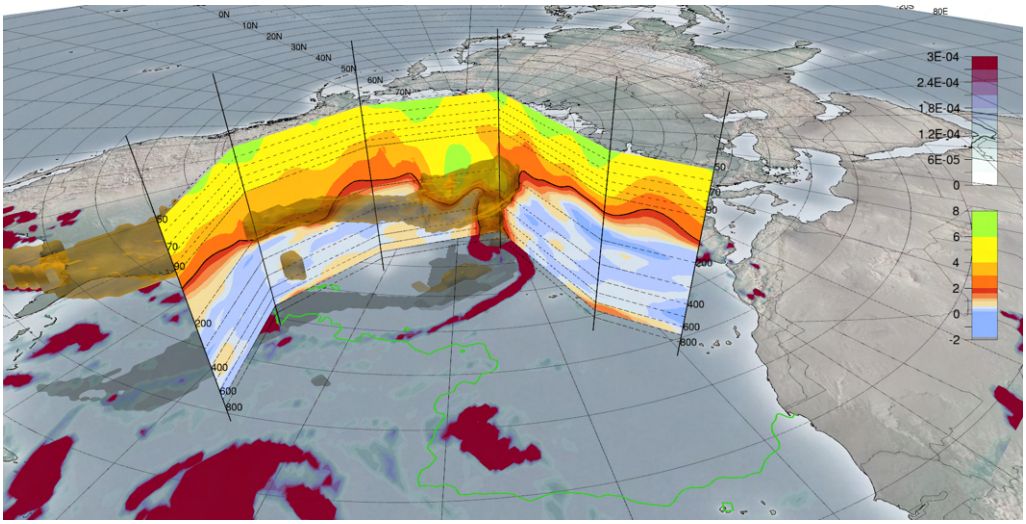

Fig. 41: PV Development over the North Atlantic Ocean associated with Tropical Storm Paulette based on ERA5 Reanalysis
The PV streamer associated with storm system Paulette is shown as it is done for storm Leslie in figure 39, but for 1200 UTC 17 September 2020.

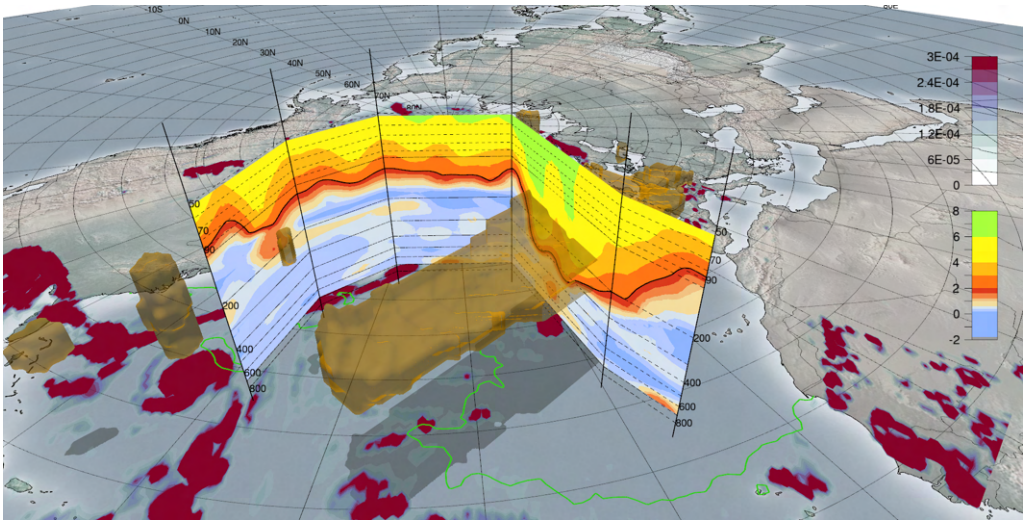

Fig. 42: PV Development over the North Atlantic Ocean associated with Tropical Storm Paulette based on ERA5 Reanalysis
The PV streamer associated with storm system Paulette is shown as it is done in figure 41, but for 1800 UTC 20 September 2020.
One is able to infer the clearly visible PV tongue which interacts with the storm system itself.

As presented in section 5.1.2.1, the development stages of Paulette, which are of further interest to us, start with the description of the system as a hurricane on September 15, 2020. This hurricane stage is visualized in the form of a PV tower anomaly in the 3-D analysis associated with an enhanced total precipitation in the vicinity of the storm. Considering the figures, we can infer the extratropical transition of the system later on as well as the inclusion of the storm into a region characterized by a highly pronounced elongated PV anomaly. The potential vorticity perspective shows that there is a large and significant contrast between the region over which the PV tongue is situated and where it is absent.
The boundaries of the PV anomaly region shown in figure 42 characterize regimes of large upper-level wind shear because of the enhanced PV gradients at these locations. This will be of further interest when analyzing the ensemble development in the next section.
Understanding the PV dynamics associated with the reanalysis data of the two storm systems lays the foundation for a deeper analysis of the *Transition* and *No-Transition* group members investigated in section 5.1.1.2. By analyzing the development of the 3-D potential vorticity anomalies associated with different ensemble members in the next section, we are trying to find restrictions or characteristics a certain PV anomaly should exhibit in order to work as a sufficient seed for *Tropical Transition* scenarios in the considered case study examples.

6.2 Potential Vorticity Analysis of the Perturbed Ensemble Weather Forecast

Storm Leslie

The 3-D development of the PV streamer associated with the example of Leslie will show the necessity of considering the PV shape evolution in order to ensure a better quality of the associated weather forecast. Furthermore, we will see that the separation of the members into *Transition* and *No-Transition* group was reasonable (as stated in section 5.1.1.2) and that favorable conditions in terms of convective stability, as described by the Coupling Index, are of less importance. In the following we restrict ourselves on to the ensemble analysis with an initialization time being chosen at 0000 UTC 20 September 2018.

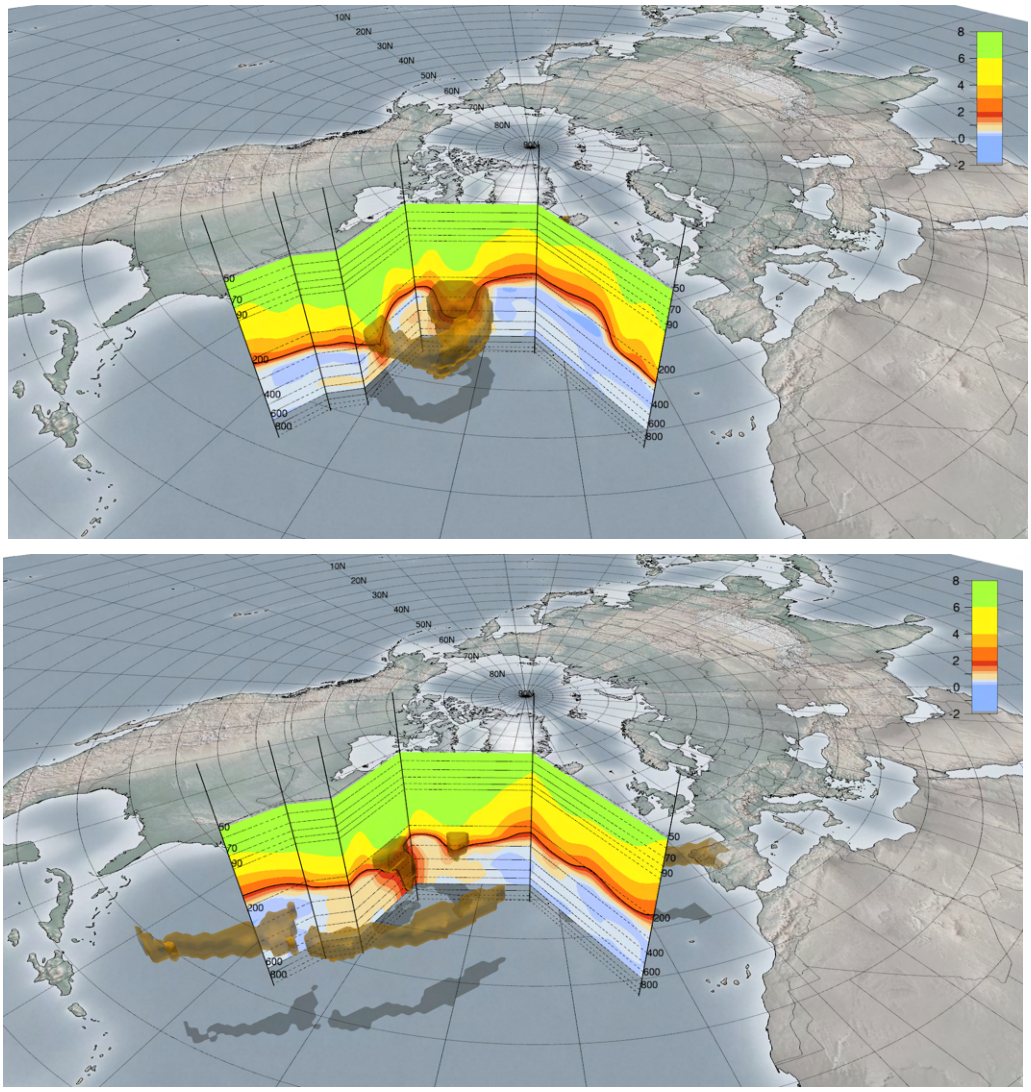

Fig. 43: PV Development over the North Atlantic Ocean associated with Tropical Storm Leslie based on ECMWF Ensemble

The PV streamer associated with storm system Leslie is shown for ensemble member 10 at 0600 UTC 27 September (top) and 1200 UTC 28 September (bottom) 2018.

A vertical cross section is used to visualize the PV (in PVU) on pressure levels denoted by the colorbar on the right hand side.

The respective streamer is colored in brown.

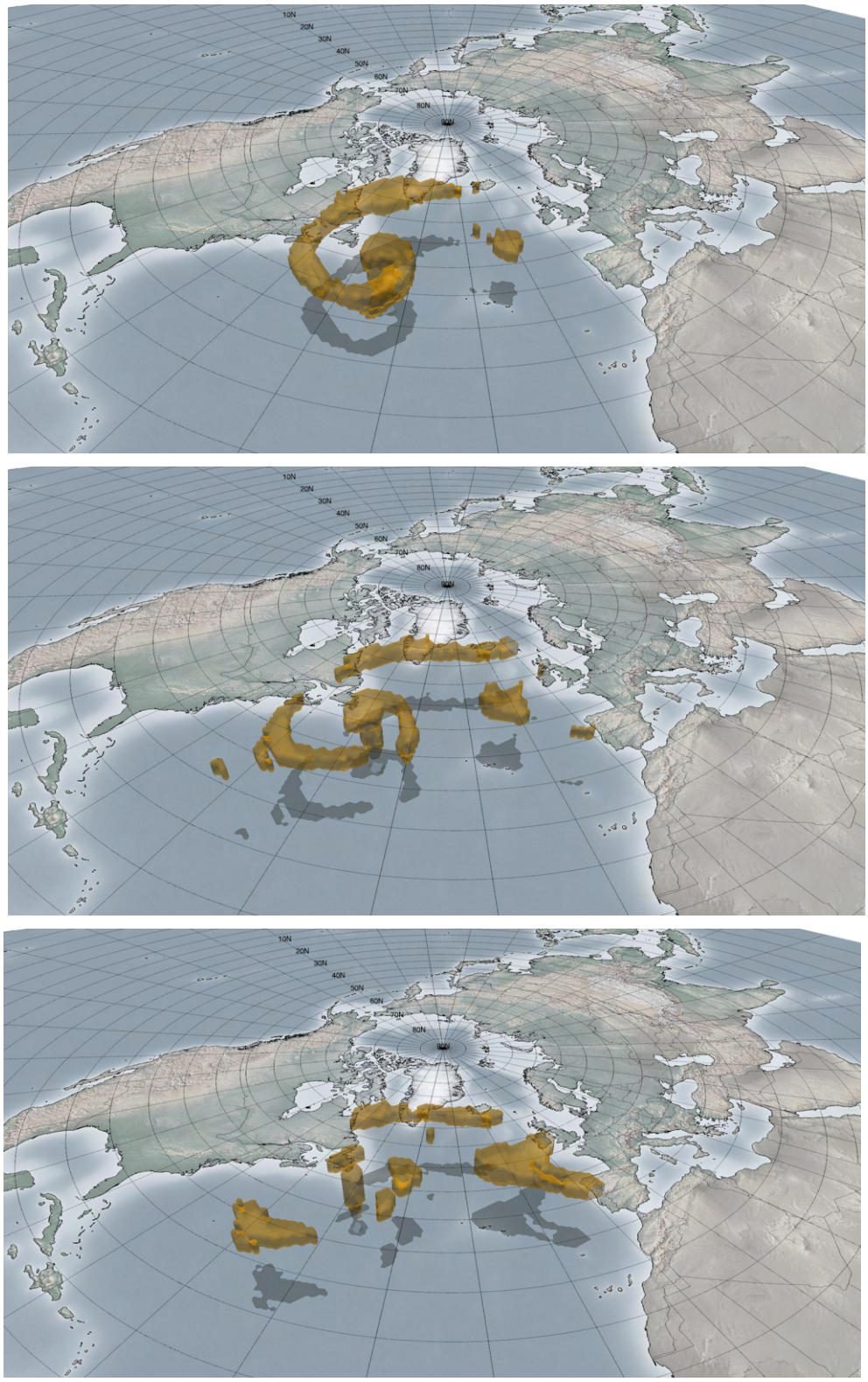

Fig. 44: PV Development over the North Atlantic Ocean associated with Tropical Storm Leslie based on ECMWF Ensemble

The PV streamer associated with storm system Leslie is shown for ensemble member 10 at 0600 UTC 27 September (top), 1200 UTC 27 September (middle) and 1800 UTC 27 September (bottom) 2018.

This example is used in order to visualize the present negative PV advection aloft.

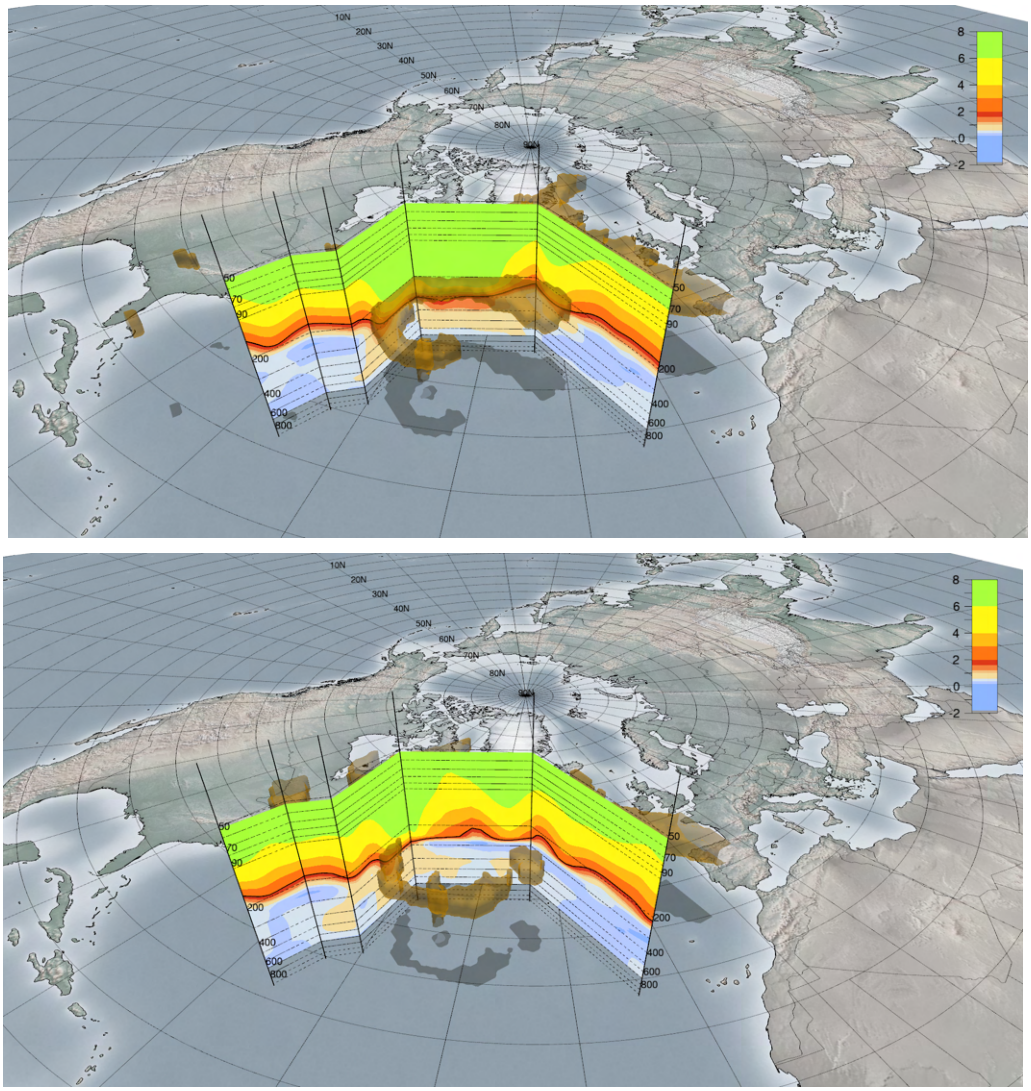

Fig. 45: PV Development over the North Atlantic Ocean associated with Tropical Storm Leslie based on ECMWF Ensemble

The PV streamer associated with storm system Leslie is shown for ensemble member 16 at 0000 UTC 29 September (top) and 1200 UTC 29 September (bottom) 2018.

The pronounced Hook shape structure as well as the negative PV advection is visualized by this development pathway.

9 out of 11 transition group members show the formation of a pronounced PV tower structure which also reaches all the way down to the 800 hPa pressure surface[1]. This visualizes the enhanced relative humidity in the vicinity of the storm system characterizing the organization of moist convection. Hence, 8 out of 11 transition group members show negative PV advection above the described convection zone (as shown in figure 44 and 46 for example), vertical wind shear is weakened and the characterization of the system as *Tropical Storm* becomes legitimate.

[1] Further information about the structural properties of the PV streamer accompanying the different ensemble members is given in table 1 of appendix section A.

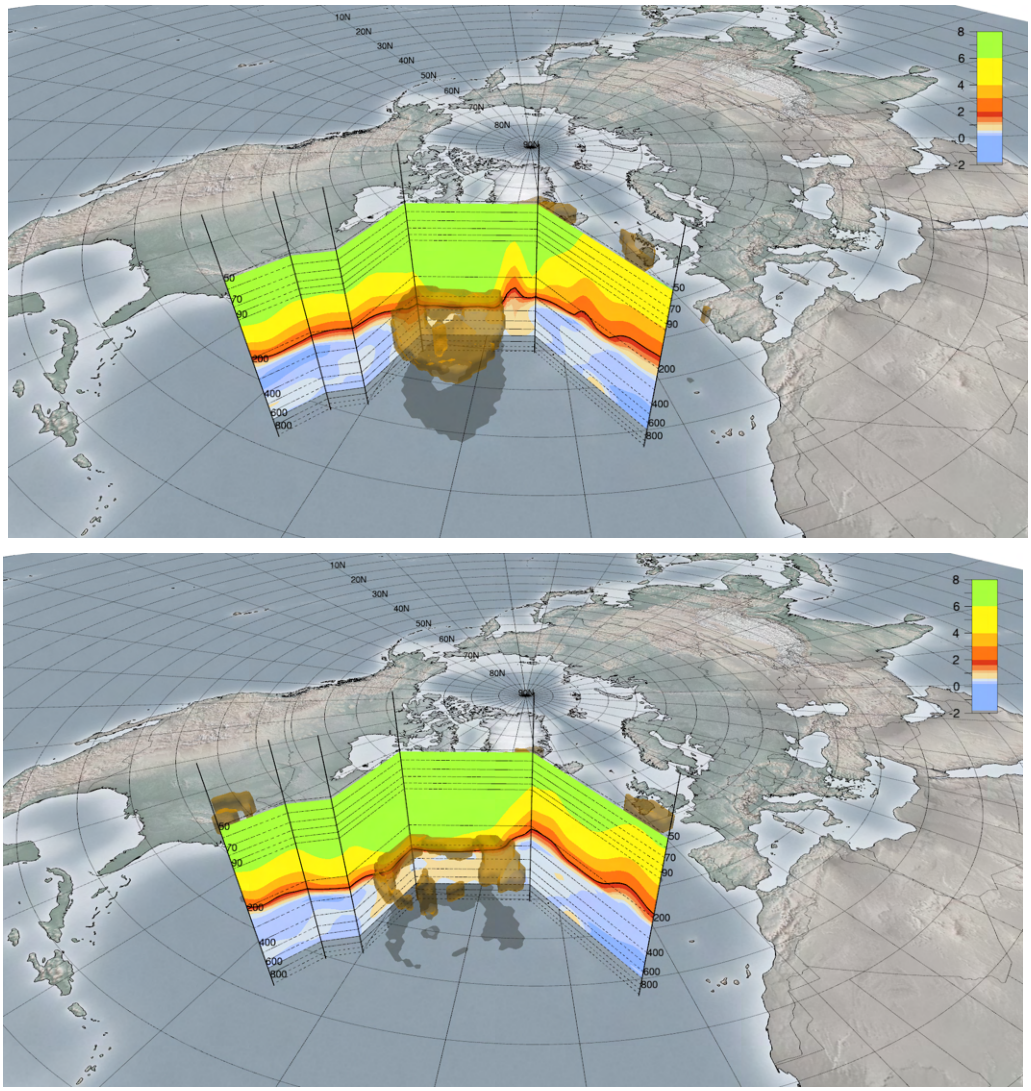

Fig. 46: PV Development over the North Atlantic Ocean associated with Tropical Storm Leslie based on ECMWF Ensemble
The PV streamer associated with storm system Leslie is shown for ensemble member 20 at 0600 UTC 28 September (top) and 1800 UTC 28 September 2020 (bottom).
Negative PV advection on top of the PV tower becomes evident.

Furthermore, most of the transition group members show a *Hook Shape* development of the associated streamer (as can be seen in figure 44 for example). This feature, which organizes a more pronounced warm seclusion, leads to an enhanced value of relative humidity in the vicinity of the storm center and therefore further strengthens the development of a tropical storm.
In contrast to the transition group, the no-transition group shows significant differences concerning the intensity and penetration depth of the PV tower as well as variations concerning the shape of the streamer itself.
Considering the development of the example members presented in figure 47, we observe one of the major restrictions for TT in the no-transition group. The associated PV streamer does not form a clearly visible hook shape in 9 out of 21 cases, therefore leading to a less pronounced warm seclusion and a lower value of relative humidity in the vicinity of the PV tower. This is also characterized by the penetration depth of the PV tower itself, which is not reaching the 800 hPa pressure surface in 19 out of 21 no-transition cases.

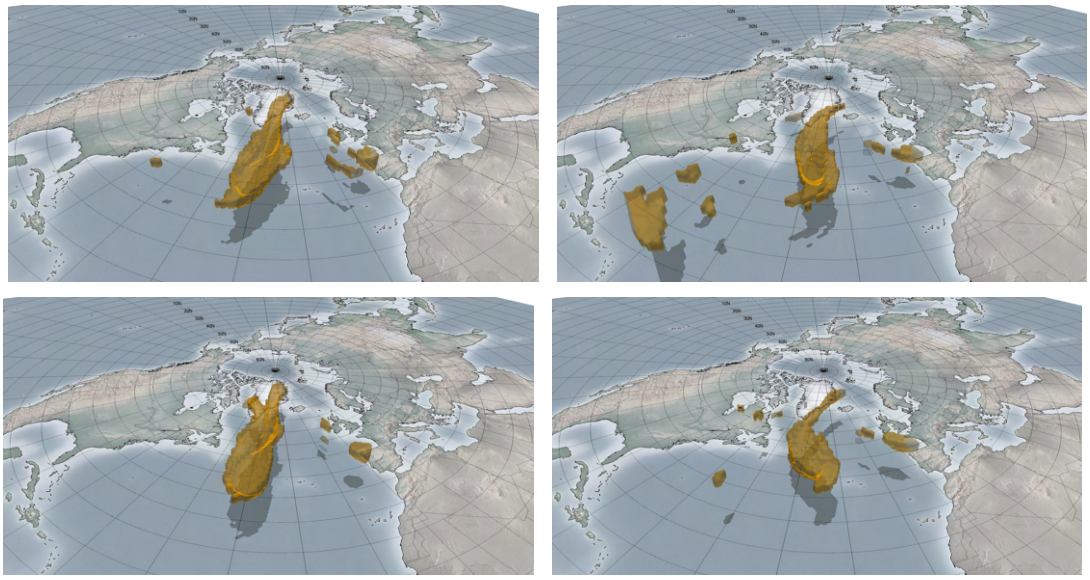

Fig. 47: PV Development over the North Atlantic Ocean associated with Tropical Storm Leslie based on ECMWF Ensemble
The PV streamer associated with storm system Leslie is shown for ensemble member 1 (left) and 21 (right) at 1200 UTC 27 September (top) and 1800 UTC 27 September (bottom) 2018. No pronounced Hook shape structure is visible.

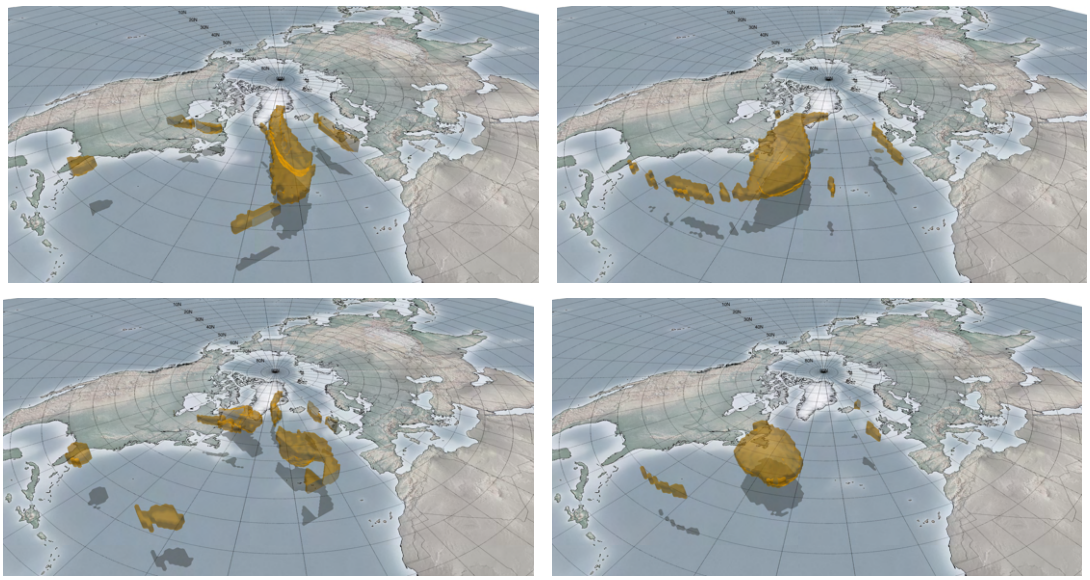

Fig. 48: PV Development over the North Atlantic Ocean associated with Tropical Storm Leslie based on ECMWF Ensemble
The PV streamer associated with storm system Leslie is shown for ensemble member 17 (left) and 26 (right) at 1200 UTC 27 September (top) and 0000 UTC 28 September (bottom) 2018. The associated PV anomaly is either located too far East (left) or West (right) in comparison to the reanalysis.

Another important feature which restricts a "successful" TT scenario is the location of the PV tower in the cyclonic roll-up region itself. As demonstrated in figure 48, the associated streamers are situated either relatively further to the east or to the west in comparison to the transition group development. This might represent the embedment of the storm in an environment of high vertical wind shear or more dry conditions restricting TT. Hence the PV

tower structures associated with the members of the no-transition group do not penetrate as deep into the troposphere as it was the case for the transition group members, there is no destruction of upper-level PV visible when analyzing the associated field evolution.
To summarize the given findings, we can state that the more pronounced hook shape of the PV streamers in the transition group, as well as the deeper penetration depth of the PV tower connected with negative PV advection aloft and the location of the tower itself are the most critical and important features leading to the TT scenario in the Leslie case.

Storm Paulette

As already stated in section 5.1.2.2, the development of tropical storm Paulette was rather complicated and extraordinary in comparison to the storm system of Hurricane Leslie. In contrast to the analysis of the latter, the differences in the 3-D PV development of the transition and no-transition group in the Paulette case are not significantly clear.
To allow for better comparison we restrict ourselves on to the ensemble analysis characterized by an initialization time being chosen at 0000 UTC 12 September 2020.

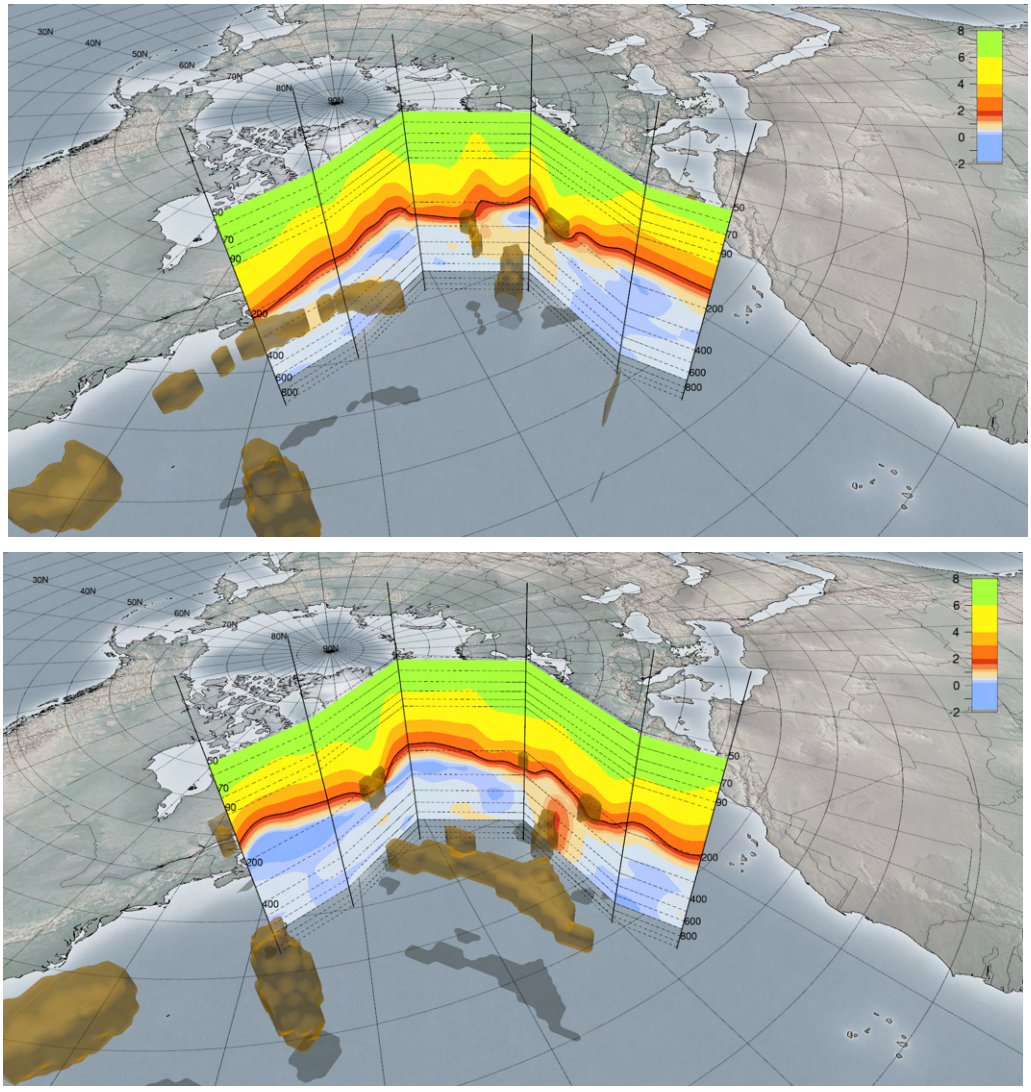

Fig. 49: PV Development over the North Atlantic Ocean associated with Tropical Storm Paulette based on ECMWF Ensemble
The PV streamer associated with storm system Paulette is shown for ensemble member 17 at 1200 UTC 19 September (top) and 1200 UTC 20 September 2020 (bottom)
The PV tower structure to the left denotes another hurricane present in this season

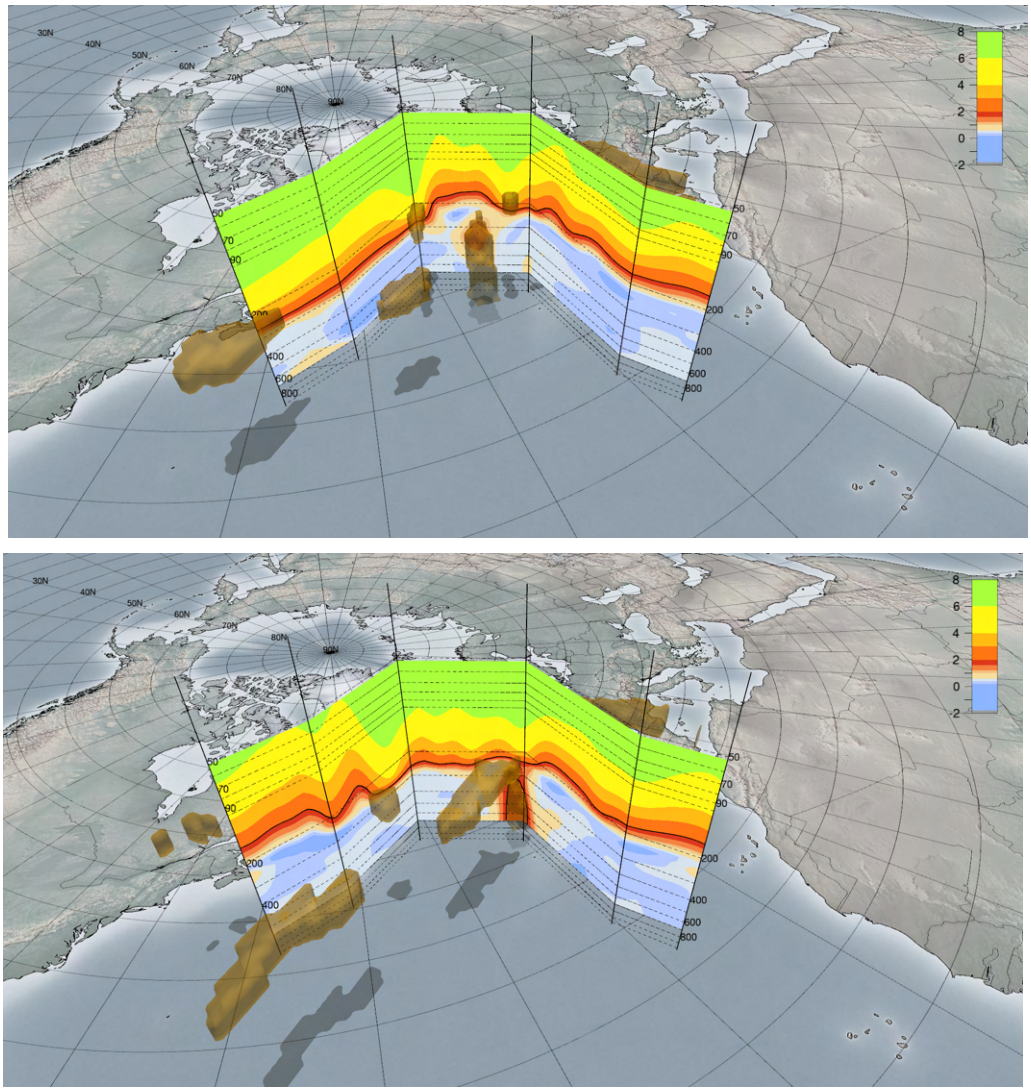

Fig. 50: PV Development over the North Atlantic Ocean associated with Tropical Storm Paulette based on ECMWF Ensemble
The PV streamer associated with storm system Paulette is shown for ensemble member 10 at 1200 UTC 19 September (top) and 1200 UTC 20 September 2020 (bottom)

Figure 49 as well as figure 50 show the PV evolution associated with two members of the transition group. While observing the consistency of the respective PV tower, the existence of the highly pronounced PV tongue observed in the reanalysis data is not as clearly visible as expected[2]. Furthermore, another two members of the transition group are characterized by pronounced PV tower structures as well, while being located too far North or South in comparison to the reanalysis. Additionally, there is no important characteristic one might deduce when analyzing the development of the other five members. Each member undergoes a substantial different evolution which gives rise to the fact that the analysis of the PV structure does not provide any conclusion about the realization of TT in this particular case. The selection of the 12th September, 2020 as initial date for analyzing the ensemble weather predictions might have been too early in this case in order to understand the TT scenario of storm system Paulette sufficiently to propound an adequate weather forecast. This visualizes the complexity of the TT process associated with the restrengthening phase of the storm itself. Nevertheless, an analysis of the no-transition group will shed light on to the most suspected reason concerning the deficiency in predicting the restrengthening phase in the Paulette case.

[2] Further information about the structural properties of the PV streamer accompanying the different ensemble members is given in table 2 of appendix section A.

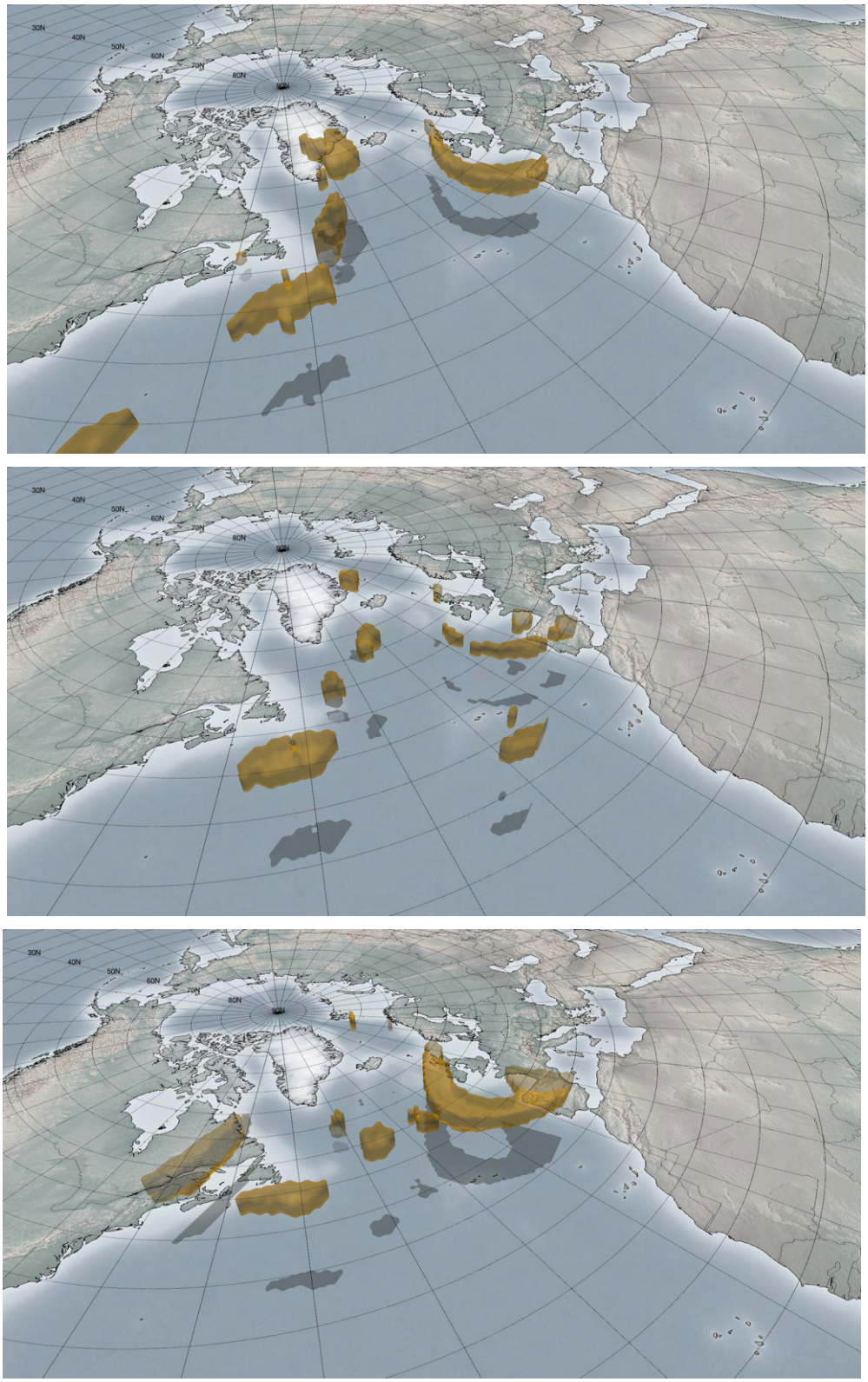

Fig. 51: PV Development over the North Atlantic Ocean associated with Tropical Storm Paulette based on ECMWF Ensemble

The PV streamer associated with storm system Paulette is shown for ensemble member 40 at 0000 UTC 19 September (top), 1200 UTC 19 September (middle) and 0000 UTC 20 September (bottom) 2018.

To highlight is the initial existence of the PV tower structure, but also its rapid diminishment during the evolution of this development pathway.

Figure 51 shows one of two members of the no-transition group which are characterised by the existence of a PV tower associated with the hurricane stage in the beginning of the investigated time window. However, the PV tower weakens and rapidly diminishes in these cases, giving rise to the embedment of the storm in a region of high vertical wind shear (see section 5.1.2.1).

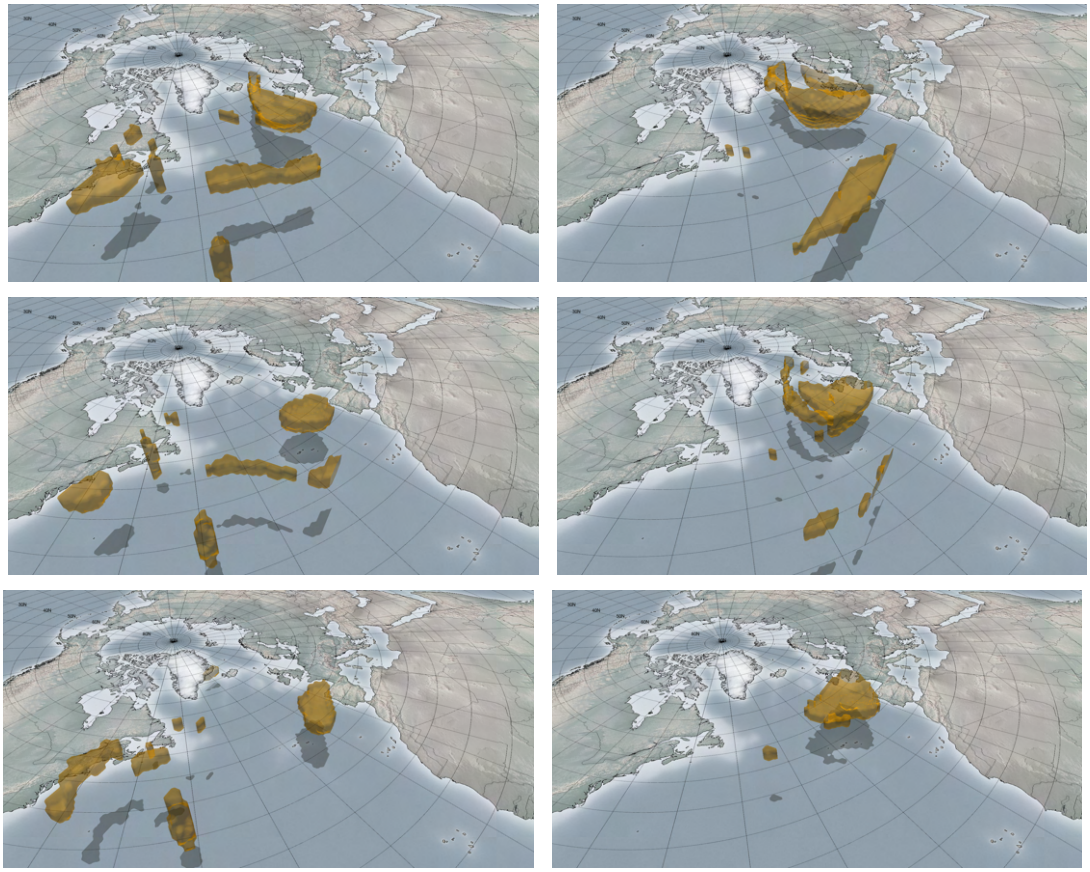

Fig. 52: PV Development over the North Atlantic Ocean associated with Tropical Storm Paulette based on ECMWF Ensemble

The PV streamer associated with storm system Paulette is shown for ensemble member 18 (left) and 34 (right) at 1800 UTC 18 September (top), 0600 UTC 19 September (middle) and 1800 UTC 19 September (bottom) 2020.

Member 18 is characterized by a PV tower structure remaining at its initial position while member 34 denotes a streamer trajectory heading too far East to serve as seed for TT.

Figure 52 visualizes the importance of the PV tower location with respect to the trough as also already identified in the ensemble analysis of storm Leslie.
Besides the vast majority of differences in the PV streamer development when analyzing the no-transition group members there is one feature the evolution of each single member has in common. Either the storms precede the trough, tending far towards the north, or more frequently, the trough itself does not form at all in a sufficiently similar form compared to the reanalysis. Therefore, the location of the storm with respect to the trough as well as the structure of the trough itself seem to be the most relevant features restricting the formation of a tropical storm in the ensemble of storm Paulette.

7 Summary and Conclusion

The aim of the current study is the precise analysis of the PV streamer development associated with already known TT events while pursuing the work of Maier-Gerber et al. (2019) [1]. By considering two case study examples the importance of understanding the given PV dynamics is worked out and highlighted. The two storm systems *Leslie* (2018) and *Paulette* (2020) are chosen because of the rather different PV development. While anticyclonic Rossby-wave breaking leads to the formation of an elongated upper-level trough structure in both cases, the pathway of Leslie follows a cyclonic roll-up of the PV streamer itself. On the other hand, the TT scenario in the Paulette case marks a restrengthening phase of an already diminished hurricane stage while at the same time being embedded in the upper-level trough feature itself.
The analysis of CPS diagrams, as well as further investigation of other environmental properties such as the Coupling Index, demonstrate the purpose of further separations when it comes to the analysis of several ensemble weather forecast members. A distinction of each perturbed forecast into warmer-core transition group and colder-core no-transition group is worked out with respect to the maximum value of the upper-level thermal wind measure $-V_T^U$ in the CPS metrics. Further investigation of the Coupling Index development associated with all four ensemble weather forecast initialization times strengthens the assumption of dividing the respective members into groups, while revealing a significantly smaller average CI value of the transition group in comparison to the no-transition group developments. Additionally, for every group and initialization time the average CI value falls below the 22.5° C temperature threshold investigated by McTaggart-Cowan et al. (2015) [9]. A more quantitative analysis of the CI development highlights that favorable conditions in terms of convective stability might not be the critical point when it comes to the understanding of the main reason for the TT development in the analysed cases, as it was also the case for Hurricane Chris (2012) [1].
In comparison to the 2-D examination demonstrated in [1], the presented twofold case study analysis culminates in the investigation of the 3-D potential vorticity development, which is associated with the ensemble weather forecast for one particular initialization time, one week prior to the TT process itself. In the case of storm system Leslie it is shown, that the separation into transition and no-transition group is reasonable. The evolution of transition group members is characterized by the formation of a hook-shaped upper-level PV streamer, demonstrating a pronounced warm seclusion, which leads to an enhanced value of relative humidity at lower levels. Furthermore, the 3-D visualization shows, that the location of the storm center relative to the trough structure, as well as the penetration depth of the PV tower and the associated intensity of the PV feature itself, turn out to be the main reason for a successful TT event in the Leslie case. Concerning storm system Paulette however, the analysis of the PV structure does not provide reasonable conclusions about the realization of TT. The selection of the 12th September, 2020 as initial date for analyzing the ensemble weather forecast might have been too early in this case to understand the TT scenario of storm system Paulette. This visualizes the complexity of the TT process associated with the restrengthening phase of storm Paulette, as is also mentioned in the reports of the National Hurricane Center of the USA. Nevertheless, similarities in the no-transition group development give rise to the interpretation, that the location of the storm with respect to the trough, as well as the structure of the trough itself, seem to be the most relevant features restricting the formation of a tropical storm in the ensemble of storm Paulette.
The presented case study analyses show that the main reasons for a successful realization of a TT scenario rely on a sufficiently favorable structure of the associated PV streamer and its development. The pronounced chaotic PV evolution in the Paulette ensemble forecast and the comparably more structured streamer development in the Leslie case shed light on to the complexity of highly baroclinically influenced Tropical Transition pathways. Hence, more in-depth future analyses, including the investigation of significantly more case study examples, as well as a broader range of initialization times, are needed to confirm the presented findings in a quantitative manner. While still remaining not fully understood, TT scenarios strongly highlight the need for more advanced future studies in a time, where the evolution of our natural environment is marked by pronounced uncertainty due to climate change.

Acknowledgements

I am thankful for the competent and friendly supervision of Prof. Andreas Fink. I felt very welcome in the group of atmospheric dynamics and enjoyed it a lot to be a part of the C3 project of Waves to Weather as well. I appreciated the meetings and discussion rounds we had and especially had fun to be part of fruitful conversations.
I also want to thank my supervisor Prof. André Butz, who always found time to discuss problems and the management of the thesis itself.
Furthermore I am really happy to get the chance to work together with Christoph Fischer and Brett Chung, who always helped me with upcoming issues besides the relaxed and wonderful atmosphere between us.
I want to thank my former fellow students Lukas, Muriel, Laura, Leonardo and Irene who stuck by my side through hard and funny times during our studies.
I also thank Karina, Mayuko, Mathis and all the other friends that offered me professional advice and emotional support.
I thank my sister, her husband and my new born niece, who ever had an open ear and always put me in a good mood.
I also thank my grandmother, whose always open ear and care made my studies much easier.
Finally I want to thank my parents really much for always supporting me and making the whole path possible in the first place.

8 References

[1] Michael Maier-Gerber, Michael Riemer, Andreas H. Fink, Peter Knippertz, Enrico Di Muzio, and Ron McTaggart-Cowan. Tropical Transition of Hurricane Chris (2012) over the North Atlantic Ocean: A Multiscale Investigation of Predictability. *Monthly Weather Review*, 147(3):951–970, mar 2019.

[2] Andrew L. Hulme and Jonathan E. Martin. Synoptic- and Frontal-Scale Influences on Tropical Transition Events in the Atlantic Basin. Part I: A Six-Case Survey. *Monthly Weather Review*, 137(11):3605 – 3625, 2009.

[3] Ron McTaggart-Cowan, Thomas Galarneau, Lance F. Bosart, Richard W. Moore, and Olivia Martius. A Global Climatology of Baroclinically Influenced Tropical Cyclogenesis. *Monthly Weather Review*, 141:1963–1989, 2013.

[4] Thomas J. Galarneau, Ron McTaggart-Cowan, Lance F. Bosart, and Christopher A. Davis. Development of North Atlantic Tropical Disturbances near Upper-Level Potential Vorticity Streamers. *Journal of the Atmospheric Sciences*, 72(2):572 – 597, 2015.

[5] Christopher A. Davis and Lance F. Bosart. The TT Problem: Forecasting the Tropical Transition of Cyclones. *Bulletin of the American Meteorological Society*, 85:1657–1662, 2004.

[6] Jenni L. Evans and Mark P. Guishard. Atlantic Subtropical Storms. Part I: Diagnostic Criteria and Composite Analysis. *Monthly Weather Review*, 137(7):2065 – 2080, 2009.

[7] Alicia M. Bentley, Lance F. Bosart, and Daniel Keyser. Upper-Tropospheric Precursors to the Formation of Subtropical Cyclones that Undergo Tropical Transition in the North Atlantic Basin. *Monthly Weather Review*, 145(2):503 – 520, 2017.

[8] Christopher A. Davis and Lance F. Bosart. Baroclinically Induced Tropical Cyclogenesis. *Monthly Weather Review*, 131:2730–2747, 2003.

[9] Ron McTaggart-Cowan, Emma L Davies, Jonathan G. Fairman, Thomas Galarneau, and David M. Schultz. Revisiting the 26.5°C Sea Surface Temperature Threshold for Tropical Cyclone Development. *Bulletin of the American Meteorological Society*, 96:1929–1943, 2015.

[10] Ron McTaggart-Cowan, Glenn D. Deane, Lance F. Bosart, Christopher A. Davis, and Thomas Galarneau. Climatology of Tropical Cyclogenesis in the North Atlantic (1948–2004). *Monthly Weather Review*, 136:1284–1304, 2008.

[11] Zhuo Wang, Weiwei Li, Melinda S. Peng, Xianan Jiang, Ron McTaggart-Cowan, and Christopher A. Davis. Predictive Skill and Predictability of North Atlantic Tropical Cyclogenesis in Different Synoptic Flow Regimes. *Journal of the Atmospheric Sciences*, 75:361–378, 2017.

[12] C. Fischer, A. H. Fink, E. Schömer, R. van der Linden, M. Maier-Gerber, M. Rautenhaus, and M. Riemer. A novel method for objective identification of 3-D potential vorticity anomalies. *Geoscientific Model Development*, 15(11):4447–4468, 2022.

[13] James R. Holton. *An introduction to dynamic meteorology.* International Geophysics Series. Elsevier Academic Press,, Burlington, MA, 4 edition, 2004.

[14] G. Lackmann. *Midlatitude Synoptic Meteorology: Dynamics, Analysis, and Forecasting.* American Meteorological Society, 2011.

[15] Nicholas L. Betts. Mid-latitude weather systems, T. N. Carlson, Harper Collins Academic (London), 1991. No. of pages: xx + 507. Price: £57.50 (hardback), £19.75 (paperback). *International Journal of Climatology*, 12:644–645, 1992.

[16] Alan J. Thorpe. Synoptic Scale Disturbances with Circular Symmetry. *Monthly Weather Review*, 114:1384–1389, 1986.

[17] Jennifer L. Catto. Extratropical cyclone classification and its use in climate studies. *Reviews of Geophysics*, 54:486 – 520, 2016.

[18] Michael J. Brennan, Gary M. Lackmann, and Kelly M. Mahoney. Potential Vorticity (PV) Thinking in Operations: The Utility of Nonconservation. *Weather and Forecasting*, 23:168–182, 2008.

[19] Christopher A. Davis and Kerry A. Emanuel. Potential Vorticity Diagnostics of Cyclogenesis. *Monthly Weather Review*, 119:1929–1953, 1991.

[20] Brian J. Hoskins. Theory of Extratropical Cyclones. 1990.

[21] Meteorological Service of New Zealand. Global Tropical Cyclone Tracks, year = Jul, 2007, volume = https://serc.carleton.edu/details/images/10170.html, Accessed 5 October 2022.

[22] William Mulroy Gray. The formation of tropical cyclones. *Meteorology and Atmospheric Physics*, 67:37–69, 1998.

[23] Dandan Tao and Fuqing Zhang. Effect of environmental shear, sea-surface temperature, and ambient moisture on the formation and predictability of tropical cyclones: An ensemble-mean perspective. *Journal of Advances in Modeling Earth Systems*, 6(2):384–404, June 2014.

[24] Wenyu Zhou. The impact of vertical shear on the sensitivity of tropical cyclogenesis to environmental rotation and thermodynamic state. *Journal of Advances in Modeling Earth Systems*, 7:1872 – 1884, 2015.

[25] Jule G. Charney and Arnt Eliassen. On the Growth of the Hurricane Depression. *Journal of Atmospheric Sciences*, 21(1):68 – 75, 1964.

[26] J. Dines. Life cycle of cyclones and the polar front theory of atmospheric circulation. By J. Bjerknes and H. Solberg. Kristiania, Geophysisks Publikationer, 3, 1922, No. 1. Pp. 18. 4°. Price 2 kr. *Quarterly Journal of The Royal Meteorological Society - QUART J ROY METEOROL SOC*, 49:140–141, 04 2007.

[27] J. G. Charney. THE DYNAMICS OF LONG WAVES IN A BAROCLINIC WESTERLY CURRENT. *Journal of Meteorology*, 4:136–162, 1946.

[28] E. T. Eady. Long Waves and Cyclone Waves. *Tellus A*, 1:33–52, 1949.

[29] Chris D. Thorncroft, Brian J. Hoskins, and Michael E. McIntyre. Two paradigms of baroclinic-wave life-cycle behaviour. *Quarterly Journal of the Royal Meteorological Society*, 119:17–55, 1993.

[30] Gregory A. Postel and Matthew H. Hitchman. A Climatology of Rossby Wave Breaking along the Subtropical Tropopause. *Journal of the Atmospheric Sciences*, 56:359–373, 1999.

[31] Kerry A Emanuel. Sensitivity of tropical cyclones to surface exchange coefficients and a revised steady-state model incorporating eye dynamics. *Journal of Atmospheric Sciences*, 52(22):3969–3976, 1995.

[32] Robert E. Hart. A Cyclone Phase Space Derived from Thermal Wind and Thermal Asymmetry. *Monthly Weather Review*, 131:585–616, 2003.

[33] M.Angels Picornell, Joan Campins, and Agusti Jansa. Detection and thermal description of medicanes from numerical simulation. *Natural hazards and earth system sciences*, 1, 11 2013.

[34] Robert Hart. The extratropical transition of Atlantic tropical cyclones: Climatology, life-cycle definition, and a case study. 01 2001.

[35] Rachel G. Mauk and Jay S. Hobgood. Tropical Cyclone Formation in Environments with Cool SST and High Wind Shear over the Northeastern Atlantic Ocean. *Weather and Forecasting*, 27:1433–1448, 2012.

[36] Walker E. Kelly and Donald R. Mock. A Diagnostic Study of Upper Tropospheric Cold Lows Over the Western North Pacific. *Monthly Weather Review*, 110:471–480, 1982.

[37] Kevin I. Hodges. A General Method for Tracking Analysis and Its Application to Meteorological Data. *Monthly Weather Review*, 122:2573–2586, 1994.

[38] Yolande Serra, George N. Kiladis, and Kevin I. Hodges. Tracking and Mean Structure of Easterly Waves over the Intra-Americas Sea. *Journal of Climate*, 23:4823–4840, 2010.

[39] Enrico Di Muzio, Michael Riemer, Andreas H. Fink, and Michael Maier-Gerber. Assessing the predictability of Medicanes in ECMWF ensemble forecasts using an object-based approach. *Quarterly Journal of the Royal Meteorological Society*, 145:1202 – 1217, 2019.

[40] Melvyn Shapiro and Daniel Keyser. Fronts, Jet Streams and the Tropopause. 1990.

[41] David Bolton. The Computation of Equivalent Potential Temperature. *Monthly Weather Review*, 108(7):1046 – 1053, 1980.

[42] Deborah E. Hanley, John E Molinari, and Daniel Keyser. A Composite Study of the Interactions between Tropical Cyclones and Upper-Tropospheric Troughs. *Monthly Weather Review*, 129:2570–2584, 2001.

[43] Mark DeMaria, John A. Knaff, and Bernadette H. Connell. A Tropical Cyclone Genesis Parameter for the Tropical Atlantic. *Weather and Forecasting*, 16:219–233, 2001.

[44] Maxi Boettcher and Heini Wernli. Diabatic Rossby waves in the Southern Hemisphere. *Quarterly Journal of the Royal Meteorological Society*, 141, 2015.

[45] Herbert Riehl. ON THE FORMATION OF TYPHOONS. *Journal of Meteorology*, 5:247–265, 1948.

[46] John Molinari, Steven Skubis, David Vollaro, Frank Alsheimer, and Hugh E. Willoughby. Potential Vorticity Analysis of Tropical Cyclone Intensification. *Journal of the Atmospheric Sciences*, 55(16):2632 – 2644, 1998.

[47] Michael Riemer and Sarah C. Jones. Interaction of a tropical cyclone with a high-amplitude, midlatitude wave pattern: Waviness analysis, trough deformation and track bifurcation. *Quarterly Journal of the Royal Meteorological Society*, 140, 2014.

[48] Sarah C. Jones, Patrick A. Harr, Jim Abraham, Lance F. Bosart, Peter J. Bowyer, Jenni L. Evans, Deborah E. Hanley, Barry N. Hanstrum, Robert E. Hart, François Lalaurette, Mark R. Sinclair, Roger K. Smith, and Chris Thorncroft. The Extratropical Transition of Tropical Cyclones: Forecast Challenges, Current Understanding, and Future Directions. *Weather and Forecasting*, 18(6):1052 – 1092, 2003.

[49] Jonathan E. Martin. The Structure and Evolution of a Continental Winter Cyclone. Part I: Frontal Structure and the Occlusion Process. *Monthly Weather Review*, 126(2):303 – 328, 1998.

[50] Paul David Reasor, Michael T. Montgomery, and Lewis D. Grasso. A New Look at the Problem of Tropical Cyclones in Vertical Shear Flow: Vortex Resiliency. *Journal of the Atmospheric Sciences*, 61:3–22, 2004.

[51] Roger K. Smith. LECTURES ON TROPICAL CYCLONES. 2006.

[52] Kerry A. Emanuel. An Air-Sea Interaction Model of Intraseasonal Oscillations in the Tropics. *Journal of the Atmospheric Sciences*, 44:2324–2340, 1987.

[53] Lance F. Bosart and Joseph A. Bartlo. Tropical Storm Formation in a Baroclinic Environment. *Monthly Weather Review*, 119(8):1979 – 2013, 1991.

[54] H. C. Davies and C. H. Bishop. Eady Edge Waves and Rapid Development. *Journal of Atmospheric Sciences*, 51(13):1930 – 1946, 1994.

[55] Marie-Dominique Leroux, Matthieu Plu, David Barbary, Frank Roux, and Philippe Arbogast. Dynamical and Physical Processes Leading to Tropical Cyclone Intensification under Upper-Level Trough Forcing. *Journal of the Atmospheric Sciences*, 70(8):2547 – 2565, 2013.

[56] Douglas J. Parker and Alan J. Thorpe. Conditional convective heating in a baroclinic atmosphere : a model of convective frontogenesis. *Journal of the Atmospheric Sciences*, 52:1699–1711, 1995.

[57] Kerry Emanuel. The Theory Of Hurricanes. *Annual Review of Fluid Mechanics*, 23:179–196, 11 2003.

[58] Russell L. Elsberry. A global view of tropical cyclones. 1987.

[59] PMF IAS. Tropical Cyclones: Favorable Conditions for Formation, Stages of Formation & Structure, Accessed 5 October 2022. https://www.pmfias.com/tropical-cyclones-favorable-conditions-tropical-cyclone-formation/, Jul 31, 2018.

[60] D. P. Roberts R. J. Pasch. Hurricane Leslie. https://www.nhc.noaa.gov/data/tcr/AL132018_Leslie.pdf, Accessed 5 October 2022, Mar 29, 2019.

[61] A. S. Latto. Hurricane Paulette. https://www.nhc.noaa.gov/data/tcr/AL172020_Paulette.pdf, Accessed 5 October 2022, Apr 1, 2021.

[62] Howard Bluestein. Observations and theory of weather systems. 1993.

[63] J. A. Zehnder. Tropical Cyclone. https://www.britannica.com/science/tropical-cyclone, Accessed 5 October 2022, Sep 28, 2022.

A Appendix

Table 1: Qualitative Differences in the PV Streamer Structure Accompanying Different Ensemble Members in the Leslie Case
Investigation of 32 *Transition and No-Transition Group members*
Initialization Time: 0000 UTC 20 September 2018

Structural Feature	Transition Group Members (11 in total)	No-Transition Group Members (21 in total)
Formation of a PV tower reaching the 800 hPa isobar	$9 \approx 81.82\%$	$2 \approx 9.52\%$
Realization of a pronounced Hook shape	$8 \approx 72.73\%$	$12 \approx 57.14\%$
Clearly visible negative PV advection	$8 \approx 72.73\%$	$1 \approx 4.76\%$

Table 2: Qualitative Differences in the PV Streamer Structure Accompanying Different Ensemble Members in the Paulette Case
Investigation of 23 *Transition and No-Transition Group members*
Initialization Time: 0000 UTC 12 September 2020

Structural Feature	Transition Group Members (9 in total)	No-Transition Group Members (14 in total)
Formation of a PV tower reaching the 800 hPa isobar	$4 \approx 44.44\%$	$2 \approx 14.29\%$
Realization of a PV tongue	$5 \approx 55.56\%$	$4 \approx 28.57\%$
Clearly visible negative PV advection	$2 \approx 22.22\%$	$0 = 0\%$

Selbstständigkeitserklärung

Ich versichere, dass ich diese Arbeit selbstständig verfasst habe und keine anderen als die angegebenen Quellen und Hilfsmittel benutzt habe.

Datum: 08.10.2022

Name: Marvin Kriening

Unterschrift: